FINAL REPORT

Physico-Mechanical Assessment of Using Scrap Tires as an Aggregate in Concrete Masonry Buildings

Prepared for

Missouri Department of Natural Resources

By

Ahmed Gheni, Ph.D.
Tousif Mahmood
Mohamed ElGawady, Ph.D.

Missouri University of Science and Technology, Rolla, Missouri

Jan 2020

The opinions, findings, and conclusions expressed in this publication are those of the principal investigators. They are not necessarily those of the Missouri Department of Natural Resources. This report does not constitute a standard or regulation.

TECHNICAL REPORT DOCUMENTATION PAGE.

1. Report No.:	2. Government Accession No.:	3. Recipient's Catalog No.:
4. Title and Subtitle: Physico-Mechanical Assessment of Using Scrap Tires as an Aggregate in Concrete Masonry Buildings		5. Report Date: 6. Performing Organization Code:
7. Author(s): Ahmed Gheni, Tousif Mahmood, Mohamed ElGawady		8. Performing Organization Report No.:
9. Performing Organization Name and Address: Missouri University of Science and Technology		10. Work Unit No.: 11. Contract or Grant No.:
12. Sponsoring Agency Name and Address: Missouri Department of Natural Resources		13. Type of Report and Period Covered: Final Report. 14. Sponsoring Agency Code:
15. Supplementary Notes:		

16. Abstract:

This study aimed at using crumb rubber in concrete masonry units (CMUs), producing rubberized concrete masonry units (RCMUs). The RCMUs were successfully produced in the laboratory and a masonry production plant in Jefferson City. Furthermore, mortar plaster incorporating rubber fiber powder was used as a corrosion, thermal, and acoustic repair for existing masonry structures. CMUs having 15% sand replacement with crumb rubber produce RCMUs that meet the ASTM requirements for loadbearing units. RCMUs were used for the construction of masonry prisms and full-scale shear walls. Fully-grouted RCMUs prisms did not display significant reduction in compressive strength. They also displayed high ultimate axial strains. The masonry walls made from RCMUs displayed high ultimate axial strain, energy dissipation, and viscous damping. The specific heat of RCMUs increased linearly with an increase in the rubber content. The thermal conductivity of RCMUS also displayed a nonlinear decrease with an increase in the rubber content. Such improvements can significantly decrease the energy consumption in buildings. In addition, rubberized mortar plaster mixtures with up to 20% RFP showed an improved bulk and surface electrical resistivity values which are a significant indication for better reinforcement corrosion resistance. Therefore, rubberized mortar plaster can be used for protection against corrosion. Rubberized mortar also displayed high resistance to carbonation. Using rubberized mortar plaster improved sound absorption and noise cancellation.

17. Key Words: Rubber – Scrap tires – Recycling - Masonry		18. Distribution Statement:	
19. Security Classification (of this report): Unclassified.	20. Security Classification (of this page): Unclassified.	21.	22. Price:

EXECUTIVE SUMMARY

With more than 1.1 billion vehicles on the road today and the expectation to double this number by 2040, the world is facing a serious threat dealing with an billion scrap tires annually. There is also a tremendous increase in the depletion of natural materials used in infrastructure construction, which puts a huge burden on the environment. Therefore, there is an opportunity for reducing the impact of the construction industry on the environment by replacing a portion of the mineral aggregate with recycled tire aggregates.

This report investigates utilizing recycled crumb rubber as a partial replacement of natural mineral aggregate in the production of concrete masonry units (CMUs), producing rubberized concrete masonry units (RCMUs). The project started with optimizing the size of the rubber particles and the rubber replacement ratios. Based on these parameters, RCMUs were produced both in the laboratory and in a plant setting. The mechanical, thermal, and acoustic properties of the RCMUs were examined. It was found that crumb rubber with particle sizes between 2.83 and 0.841 mm can replace up to 15% of fine aggregate to produce RCMUs that meet the ASTM requirements for loadbearing units. Using crumb rubber also improved the durability and thermal and acoustic properties of CMUs.

Rubber fiber powder (RFP) was also used as a sand replacement in mortar for plastering of masonry. Applying rubberized plastering mortar improved the sound absorption, noise reduction, corrosion resistance, and carbon penetration. Furthermore, using rubberized plaster reduced the thermal conductivity of CMUs based on the size and amount of RFP as well as the thickness of the plastering layer by up to 53% compared to conventional plastering.

ACKNOWLEDGMENTS

The authors would like to acknowledge the many individuals and organizations that made this research project possible. The authors wish to extend a very sincere thank you to the Missouri Department of Natural Resources (MoDNR). In addition to their financial support, the authors appreciate MoDNR's vision and commitment to innovative concepts and pushing the boundaries of current practice. In particular, the success of this project would not have been possible without the support, encouragement, and patience of Messrs. Chris Nagel, Dan Fester, Rick Kempker, and Kirk Mitchell.

Appreciation is extended to Midwest Block and Brick for providing conventional CMUs and also allowing the researchers to use their facility in Jefferson City to produce the RCMUs. A sincere thank you is extended to Messrs. Mark Wilhelms, Brian Wieberg, Darryl Winegar, Jason Gerling, and Dan Brenneke; without their help the production of the RCMUs would not be possible.

The authors would like to thank the graduate students that contributed to this project including Y. Darwish, E. Gomaa, and B. Shrestha. Many undergraduate students also helped in many tasks in the laboratory. The authors also appreciate the tireless staff of the Department of Civil, Architectural, and Environmental Engineering. Their assistance both inside and out of the various laboratories was invaluable to the successful completion of this project.

Contents

1. Introduction and Literature Review 16
1.1. Utilizing scrap tire rubber in concrete 19
1.1.1. Effect of scrap tire rubber on fresh properties of concrete 19
1.1.2. Effect of scrap tire rubber on hardened properties of concrete 20
1.1.3. Effect of scrap tire rubber on ductility and seismic behavior of concrete 20
1.1.4. Effect of scrap tire rubber on durability of concrete 21
1.1.5. Thermal and acoustic behavior of rubberized concrete 22
1.1.6. Utilizing scrap tire rubber in concrete masonry 23
1.1.7. Utilizing scrap tire rubber in pavement 24
1.2. Report organization 25
2. Optimization of Mixtures and Production of RCMUs. 27
2.1. Optimizing the compaction pressure and vibration. 27
2.2. Optimizing crumb rubber size and ratio. 37
2.3. Production of trial RCMUs in the lab. 40
2.3.1. Compressive strength of the trial RCMUs. 46
2.4. Production of RCMUs in plant settings. 48
2.4.1. Mechanical characterization of RCMUs. 50
3. Durability of Rubberized Concrete Masonry Units 56
3.1. Characterize the resistance of RCMUs to severe weather and cycles of freeze and thaw. 56
3.2. Durability properties of cement mortar with recycled rubber 56
3.2.1. Material Properties 57
3.2.2. Experimental work 59
3.2.2.1. Density, absorption, and air voids in hardened mortar 61
3.2.2.2. Heat of hydration 62
3.2.2.3. Accelerated carbonation 63
3.2.2.4. Electrical resistivity 63
3.2.2.5. Rapid chloride ion penetration (RCIP) 64
3.2.3. Results and discussion 66
3.2.3.1. Fresh properties 66
3.2.3.2. Density, absorption, and air voids in hardened mortar 68

3.2.3.3. Heat of hydration 72
3.2.3.4. Electrical resistivity 74
3.2.3.5. Rapid chloride ion penetration (RCPT) 77
3.2.3.6. Accelerated carbonation 78
4. Mechanical Characterization of RCMU Prisms and Walls. 81
4.1. Mechanical Characterization of RCMU Prisms 81
4.1.1. RCMU Prisms Preparation 81
4.1.2. Test Set-up, Loading, and Instrumentations 82
4.1.3. Materials Properties 83
4.1.4. Results and discussion 83
4.2. Cyclic Behavior of Post-tensioned Rubberized Masonry Shear Wall 88
4.2.1. Experimental Program 88
4.2.1.1. Material Properties 91
4.2.1.2. Wall construction 91
4.2.1.3. Test Setup 92
4.2.1.4. Loading protocol 95
4.2.1.5. Instrumentation 95
4.2.2. Experimental Results 96
4.2.2.1. Failure mode and extent of damage 96
4.2.2.1.1. The performance of the reference wall 96
4.2.2.1.2. The performance of a rubberized wall 99
4.2.2.2. Deformation profile along the wall height 101
4.2.2.3. Strain profile along the wall length 103
4.2.2.4. Load displacement response 104
4.2.2.5. Displacement ductility 104
4.2.2.6. Energy dissipation 105
4.2.2.7. Equivalent viscous damping 106
4.2.3. Conclusions 107
5. Masonry Thermal Characterization 109
5.1. Thermal characterization of rubberized concrete masonry units 110
5.1.1. Experimental Program 110

5.1.1.1. Thermal characterization of rubber particles 110
5.1.1.2. Thermal characterization of rubberized cement paste 112
5.1.1.3. Thermal conductivity of RCMUs 117
5.1.1.3.1. Thermal needle probe method 117
5.1.1.3.2. Guarded hot plate assembly method 118
5.1.1.3.3. Two controlled sides guarded hot box apparatus 121
5.1.1.3.4. The hot box apparatus 123
5.1.2. Results and discussion 127
5.1.2.1. Thermal needle probe method 128
5.1.2.2. Guarded hot plate assembly method 129
5.1.2.3. Two Controlled sides guarded hot box method 129
5.1.2.4. The hot box apparatus method 131
5.2. Thermal and acoustic retrofitting of CMU using eco-friendly rubberized plastering 134
5.2.1. Material properties 134
5.2.2. Experimental program 137
5.2.2.1. Mechanical properties of rubberized mortar 137
5.2.2.1.1. Density, water absorption, and air voids 137
5.2.2.1.2. Compressive strength 138
5.2.2.1.3. Flexural strength and toughness 138
5.2.2.1.4. Tensile strength and strain energy 140
5.2.2.2. Thermal characterization of rubberized cement mortar at different temperatures 142
5.2.2.2.1. Thermal needle probe method for plastering materials 143
5.2.2.2.2. The guarded hot box method 144
5.2.2.3. Acoustic characterization of rubberized cement mortar 146
5.2.2.3.1. Sound absorption 146
5.2.2.3.2. Sound transmission 149
5.2.3. Results and discussion 151
5.2.3.1. Mechanical properties 151
5.2.3.1.1. Density, water absorption, and air voids 151
5.2.3.1.2. Compressive strength 152
5.2.3.1.3. Flexural and tensile strength 153

5.2.3.2. Thermal conductivity 157
5.2.3.2.1. The thermal needle probe method for plastering materials 157
5.2.3.2.2. Thermal conductivity of plaster masonry units using the guarded hot box method 158
5.2.3.3. Sound absorption 160
5.2.4. Conclusions 162
6. Conclusions and Future work 166
6.1. Findings and conclusions 167
6.2. Future work 173
7. References 174

List of Figures

Figure 1.1: U.S. Nonfuel Material Consumption, 1900-2014 (Matos 2012). 16
Figure 1.2: Scrap Tire Trends 2007 – 2017 (RMA 2018) in the U.S. 19
Figure 2.1: Gyratory compactor employed for determining the packing density of aggregate combinations. 27
Figure 2.2: The relationship between sand-to-solid materials ratio and the density of the solid components of CMU mixtures after 220 gyratory cycles under compaction pressure of: (a) 15 psi, (b) 22 psi, (c) 30 psi, (d) 36 psi), and (e) 44 psi. 29
Figure 2.3: The relationship between sand-to-solid materials ratio and the density of the solid components of CMU mixtures after 350 gyratory cycles under compaction pressure of: (a) 15 psi, (b) 22 psi, (c) 30 psi, (d) 36 psi), and (e) 44 psi. 31
Figure 2.4: The relationship between sand-to-solid materials ratio and the density of the solid components of CMU mixtures after 400 gyratory cycles under compaction pressure of: (a) 15 psi, (b) 22 psi, (c) 30 psi, (d) 36 psi), and (e) 44 psi. 33
Figure 2.5: The relationship between sand-to-solid materials ratio and the density of the solid components of CMU mixtures after 500 gyratory cycles under compaction pressure of: (a) 15 psi, (b) 22 psi, (c) 30 psi, (d) 36 psi), and (e) 44 psi. 35
Figure 2.6: The relation between number of gyratory cycles and density of the solid components of concrete masonry mixture under compaction pressure of 2 bar (30 psi). 36
Figure 2.7: The relationship between sand-to-solid materials ratio and density of the solid components of CMU mixture after 500 gyratory cycles under compaction pressure of 30 psi. 36
Figure 2.8: Different rubber sizes: (a) 4.0 to 2.83 mm, (b) 2.83-0.841 mm., (c) 0.30-0.15 mm., and (d) Smaller than 0. 075 mm. 38
Figure 2.9: The relationship between crumb rubber ratio and density of the solid components of RCMU mixture after 500 gyratory cycles under compaction pressure of 30 psi with rubber having particle sizes of: (a) 2.83 - 0.841 mm, (b) 0.30 - 0.15 mm, and (c) Smaller than 0. 075 mm. 39
Figure 2.10: Mixing the solid and liquid components of RCMU mixtures. 41
Figure 2.11: Masonry units manufacturing lab machine: (a) Machine parts, (b) Base plate, and (c) Targeted CMU shape. 42
Figure 2.12: RCMU laboratory manufacturing process: (a and b) Placing the mixture, (c and d) Compaction and vibration, and (e and f) The final shape of the CMU. 44
Figure 2.13: RCMU laboratory curing: (a) stocking and labeling the units, and (b) placing the units inside the curing room. 45
Figure 2.14: Compressive strength test setup. 46
Figure 2.15: Compressive strength of RCMUs produced in the laboratory. 47
Figure 2.16: RCMU production process in a masonry plant in Jefferson City: (a and b) RCMUs after compaction and vibration, (c) Stocking and labeling the units, and (d) Curing the units in the curing room. 49

Figure 2.17: Water absorption and density tests: (a) Drying the RCMUs in the oven, (b) Soaking the RCMUs in water, and (c and d) Measuring the immersed weight or RCMU. 51
Figure 2.18: Effect of rubber replacement ratios on the oven dry density of RCMU. 53
Figure 2.19: Effect of rubber replacement ratios on the water absorption of RCMU. 54
Figure 2.20: Effect of rubber replacement ratios on the compressive strength of RCMU. 55
Figure 3.1: Schematic overview of the work done in this study. 57
Figure 3.2: Particles size distribution analysis: (a) Sieve analysis of sand, and (b) Laser diffraction analysis of RFP and Cement. 58
Figure 3.3: Microscopic images of rubber powder: (a, b) The angular irregular shape of the rubber particles, and (c): Nylon fiber pieces within the powder. 59
Figure 3.5: (a) RICP test device with 4 cells, and (b) Vacuum desiccator. 65
Figure 3.6: Workability of different mortar mixtures. 66
Figure 3.7: Workability of 1:2 and 1:3 mortar mixtures. 67
Figure 3.8: Different densities of mortar with: (a) W/C= 0.51, (b) W/C= 0.56, and (c) RFP was used as a sand replacement. 69
Figure 3.9: Absorption and air voids of cement mortar with: (a) W/C= 0.51, (b) W/C= 0.56, and (c) RFP was used as a sand replacement. 71
Figure 3.10: Heat of hydration (Calorimeter) curves of mortar mixtures with different: (a) Sand addition, and (b) RFP addition ratios. 72
Figure 3.11: Magnitude of the peak heat flow and induction time of the different mortar mixtures. 73
Figure 3.12: Heat of hydration released of the different mortar mixtures. 74
Figure 3.13: Surface electrical resistivity of mortar mixtures with: (a) W/C= 0.51, and (b) W/C= 0.56. 75
Figure 3.14: Bulk electrical resistivity of mortar mixtures and its correlation with steel corrosion risk with: (a) W/C= 0.51, (b) W/C= 0.56, and (c) RFP was used as a sand replacement. 75
Figure 3.15: Charge passed through mixture with w/c ratio of 0.51 with adding RFP or sand and its correlation with the RCPT. 78
Figure 3.16: Surface resistivity versus rapid chloride permeability. 78
Figure 3.17: Different carbonation depths with different RFP or sand content. 79
Figure 3.18: Accelerated carbonation depth of mortar mixtures with: (a) W/C= 0.51, and (b) W/C= 0.56. 80
Figure 4.1: Vertical stress-strain test setup of four-block high prisms with the instrumentations. 82
Figure 4.2: Stress vs. strain of grouted four blocks height masonry prisms. 85
Figure 4.3: Failure mechanism for four blocks height prisms with: (a) No rubber added, and (b) 5% rubber ratio. 86
Figure 4.4: Rubberized masonry shear wall. 89
Figure 4.5: Conventional masonry shear wall. 90
Figure 4.6: Wall construction. 92
Figure 4.7: Detailing of post-tension inside the wall footings. 92

Figure 4.8: Loading top RC beam. 93
Figure 4.9: Details of the test setup. 94
Figure 4.10: Overall test setup. 94
Figure 4.11: Loading history as per FEMA 461. 95
Figure 4.12: External instrumentation arrangement. 96
Figure 4.13: Hysteresis loops of the reference wall. 97
Figure 4.14: (a) Crushing of the toe at maximum load, (b) At drift of 1.18%, (c) Shear cracks and compression zone, (d) Deformed PVC with steel rebar embedded at the end of test, and (e) Extent of damage at the end of the test. 98
Figure 4.15: Hysteresis loops of the rubberized wall. 99
Figure 4.16: (a) Wall with rubberized blocks in the plastic hinge region, (b) Compression cracks, (c) Splitting cracks at the toe, (d) Damage extent of the different blocks at the end of the test, and (e) Damage at wall ends at the end cycles. 100
Figure 4.17: Curvature: (a) At a cross section, and (b) Curvature profile along wall height. 101
Figure 4.18: Curvature profile along with wall height of the walls at different % drift levels, (a) reference wall and (b) rubberized wall. 102
Figure 4.19: Strain profile along wall length at different % drift levels, (a) reference wall and (b) rubberized wall. 103
Figure 4.20: Load-displacement envelope for the investigated walls. 104
Figure 4.21: Energy dissipation. 106
Figure 4.22: Equivalent viscous Damping, ζ (%). 107
Figure 5.1: Gyratory compactor employed for determining the packing density of aggregate combinations. 109
Figure 5.2: Differential scanning calorimetry (DSC) of crumb rubber. 111
Figure 5.3: NETZSCH simultaneous TGA/DTA. 112
Figure 5.4: Thermogravimetric analysis (TGA) for cement mixes with varying rubber content. 113
Figure 5.5: Differential thermal analysis (DTA) for cement mixes with varying rubber content. 114
Figure 5.6: Specific heat test of rubberized cement paste (a) Heat flow vs. temprature, and (b) Specific heat vs. rubber content. 116
Figure 5.7: Thermal needle probe test using KD2 PRO portable thermal properties analyzer (a) testing the RMCU (b) CMU component test locations. 118
Figure 5.8: Thermal conductivity apparatus general layout. 119
Figure 5.9: Thermal conductivity measuring system (a) testing box, and (b) the entire system. 120
Figure 5.10: Two controlled sides apparatus (a) The controlled heat source in the apparatus, (b) Testing specimen and data acquisition system, (c) Calibration block, and (d) Measuring the transferred heat with thermocouples. 122
Figure 5.11: The hot box apparatus (a) hot box, and (b) Power monitoring meter. 124

Figure 5.12: Thermal images of the guarded hot box (a) Side view image before testing, (b) Front view image before, (c) Side view image during testing, and (d) Front view image during testing. 125
Figure 5.13: The materials used for calibration. 127
Figure 5.14: Thermal conductivity factor for RCMUs (solid lines) and LWCMUs (dotted lines) using different approaches. 128
Figure 5.15: ΔT between the inner and outer faces of blocks at the steady-state case. 130
Figure 5.16: Time to reach steady state. 131
Figure 5.17: Reduction in energy consumption for rubberized and lightweight masonry units. 133
Figure 5.18: Sieve analysis of the two grades of rubber and cement. 134
Figure 5.19: SEM analysis of the two grades of rubber (a) Rubber < sieve No. 200, and (b) Rubber between sieves No. 50 and 100. 136
Figure 5.20: Flexural strength and toughness: (a) flexural strength test setup, and (b) Modulus of toughness calculation. 139
Figure 5.21: Tensile strength and resilience (a) Test specimen, (b) Test setup, (c) Digital extensometer for strain measurement, and (d) Modulus of resilience calculation. 141
Figure 5.22: Different thicknesses of rubberized mortar plaster with five different ratios of RFP. 142
Figure 5.23: Thermal needle probe test (a) Testing mortar specimen with KD2 PRO portable thermal properties analyzer, and (b) Thermal needle probe with and without thermal grease. 144
Figure 5.24: Acoustic absorption test (a) Testing apparatus, (b) Sound source (compression driver), (c) Microphones with holders, and (d) ACUPRO Software with data acquisition module. 148
Figure 5.25: Sound transmission testing apparatus. 149
Figure 5.26: Preparing specimens for acoustic tests (a) Using a water jet cutter to cut masonry specimens, and (b) Masonry specimen to be used in ACUPRO testing system. 150
Figure 5.27: Apparent and bulk densities of rubberized plastering mortar with varied sizes and ratios of rubber-fiber powder. 152
Figure 5.28: Compressive strength of rubberized plastering mortar with varied sizes and ratios of rubber-fiber powder. 153
Figure 5.29: Flexural strength of rubberized plastering mortar with varied sizes and ratios of rubber-fiber powder. 154
Figure 5.30: Tensile strength test: (a) stress-strain behavior of cement mortar with different rubber powder sizes and content, and (b) the ultimate strain of cement mortar with different rubber powder sizes and content. 155
Figure 5.31: Compressive strength of rubberized plastering mortar with varied sizes and ratios of rubber-fiber powder. 156
Figure 5.32: Thermal conductivity factor for rubberized mortar with different sizes and ratios of RFP. 158
Figure 5.33: Thermal conductivity coefficients of masonry units with three plastering thicknesses and varied RFP sizes and content. 159

Figure 5.34: Effect of using RFP as a sand replacement on the reduction in energy consumption of masonry units with three plastering thicknesses. _____ 160
Figure 5.35: Sound absorption coefficient of plastered masonry units with varied RFP ratios. 161
Figure 5.36: Noise reduction coefficient of plastered masonry units with varied RFP ratios. _ 162

List of Tables

Table 2.1: RCMUs lab trial mix design (lb) 40
Table 2.2: Production Report of RCMUs in Plant Settings (lb) 48
Table 2.3. Material properties 55
Table 3.1. Density results of the materials (ASTM B923−16). 58
Table 3.2: Test matrix. 60
Table 3.3: RCIP in concrete based on charge passed (ASTM C1202-17). 65
Table 4.1: Material Properties 83
Table 4.2: Average Tests Results of Four Block Height Masonry Prisms 84
Table 4.3: Material Properties 91
Table 4.4: Displacement Ductility 105
Table 5.1: Mix Proportions for Cement Mortar Mixes with Cement or Fine Aggregate Replacement by Recycled Rubber Powder 137

1. Introduction and Literature Review

Construction activities were the largest consumer of natural materials in the U.S. during the last century. As shown in Figure 1.1, U.S. consumption of construction materials is incomparable to any other material. In 1998, mineral fine and coarse aggregate production reached 1.12 gigatons representing 73% of all natural materials used (Horvath 2004). This raises serious concerns about the continuous depletion of these natural resources and exhaustion of the environment.

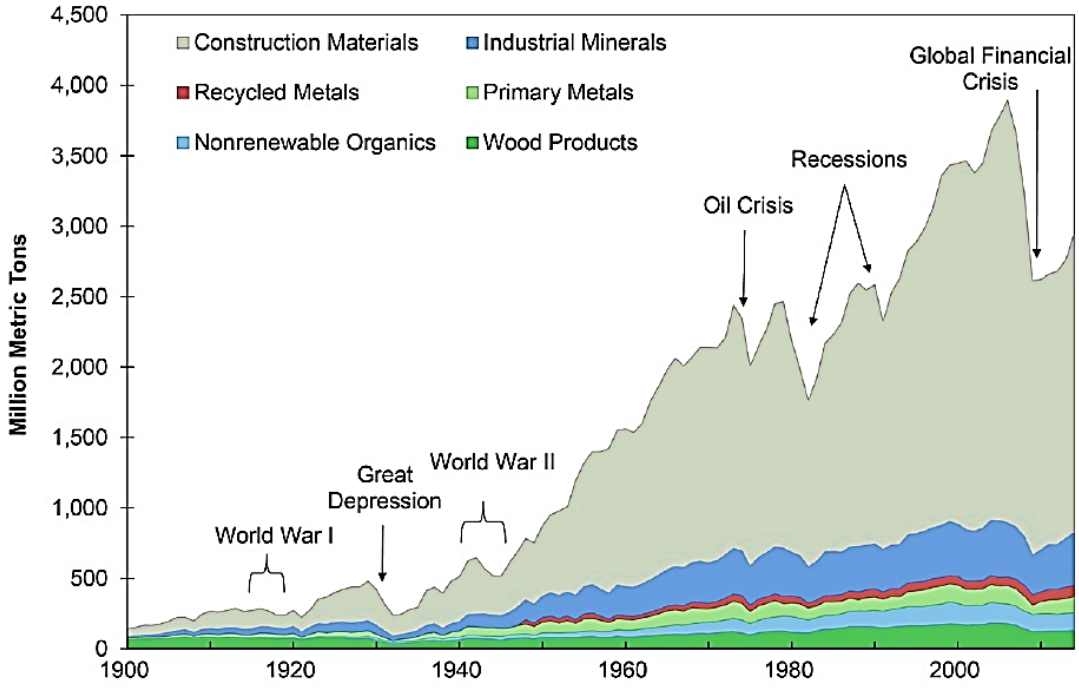

Figure 1.1: U.S. Nonfuel Material Consumption, 1900-2014 (Matos 2012).

The concrete masonry unit (CMU) is one widely used construction material, with 4.5 billion structural masonry units produced in the U.S in 2014 (Pacheco-Torgal et al. 2015). Natural aggregate is still the major component of the CMU matrix, which puts more pressure on already depleted natural resources. Furthermore, the cradle-to-gate energy processing of natural aggregate, including the extraction, manufacturing, and transporting, makes the CMU embodied energy one

of the highest compared to other construction materials such as timber and stone, increasing environmental devastation (Milne and Reardon 2005, Hammond and Jones 2008). For example, the embodied energy of concrete is 1.6 to 14.4 times that of steel, aluminum, copper, timber, plastic, brick, glass, plaster, stone, and ceramic, putting an additional burden on the environment by increasing carbon dioxide emissions (Sajwani and Nielsen 2017).

There is an opportunity for reducing the impact of the construction industry on the environment by replacing a portion of the mineral aggregate with a recycled one. For example, replacing only 10% of the mineral aggregate used in the construction industry with recycled materials would result in cutting the total annual consumption of natural aggregate by 112 million tons.

Meanwhile, the world is facing a serious threat dealing with scrap tires, given the continuous increase in the number of vehicles, which is directly connected to the increase in the global population. According to the most recent statistics, there are more than 1.1 billion vehicles on the road, and this number is expected to double by 2040 (Sperling and Gordon 2008, Sperling and Gordon 2009). This enormous number of vehicles across the world led to a global yearly production of 1.7 billion of tires and caused an annual generation of 1.0 billion scrap tires (Forrest 2014). The U.S. alone produces about 250 million scrap tires each year (RMA 2018), which results in increased environmental concerns regarding how to properly dispose of them.

Since scrap tires are not a biodegradable material, two of the largest issues regarding their disposal are fire and health hazards. It is very difficult to prevent or quench the oxygen supply of the donut-shaped tire since it contains 75% void space, which increases the fire exposure risk of scrap tires in landfills. Chemically, rubber tires burn very quickly and are very difficult to extinguish, which can lead to months of fire with a high rate of toxic gas emissions as well as surface and groundwater pollution due to the melted oil from the burned tires. These fires will emit

significant amounts of CO2 and dioxins into surrounding air and water. As a result, many landfill operators are hesitant to accept whole scrap tires. Most states in the U.S. have enacted legislation that either restricts or even bans the disposal of tires in landfills.

With regards to public health, scrap tires serve as a fertile breeding ground for mosquitoes and other insects due to their ability to collect and retain water and heat. With the serious threat of the mosquito-borne Zika virus, the current focus is not only on dealing with newly generated scrap tires but also on cleaning up old stockpiles of scrap tires.

On the bright side, the use of recycled scrap tires has accelerated over the last 20 years, significantly alleviating historic tire dump issues, and dropping the number of stockpiled tires from one billion in 1992 to 75 million in 2013. Reusing scrap tires is the best practical approach to deal with them due to the lack of both technical and economical disposal mechanisms. Current popular use of scrap tires includes using recycled crumb rubber as mulch on farms or playgrounds and as a binder modifier in asphalt; however, as shown in Figure 1.2, the civil engineering market consumes a very small portion from the total generated scrap tires because of the lack of practical applications. Another widely used application for the scrap tires was as a fuel in cement production kilns; however, their use resulted in higher CO2 and sulphur dioxide emissions during the burning process which affects the chemical composition of cement, resulting in delayed ettringite formation and potential cracking in concrete members (Olorunniwo 1994). Therefore, there is an urgent need to find new applications that can consume large quantities of scrap tires.

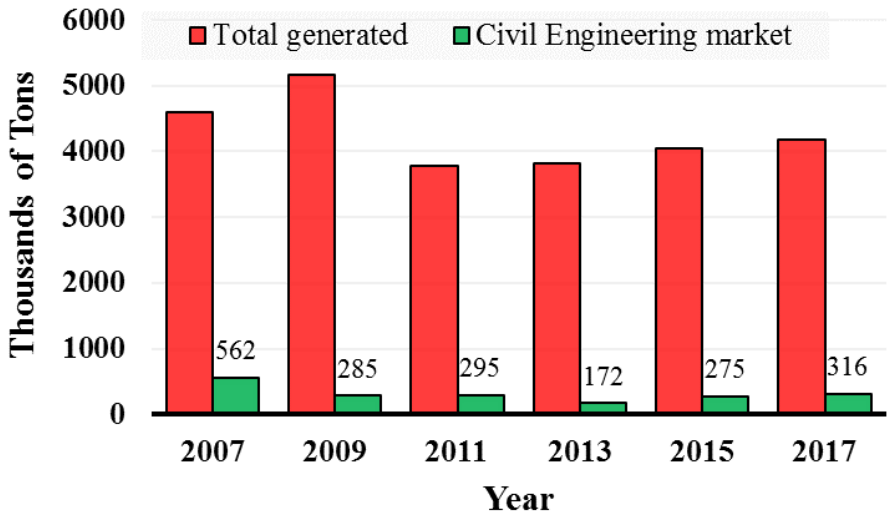

Figure 1.2: Scrap Tire Trends 2007 – 2017 (RMA 2018) in the U.S.

1.1. Utilizing scrap tire rubber in concrete

Utilization of scrap tire rubber in the construction industry has great potential and has been the focus of many researchers for different applications. One of the main applications was the use of crumb rubber in concrete as a partial replacement for fine and/or coarse aggregate. Several studies have been conducted in an attempt to investigate the impact of adding crumb rubber to both conventional and self-compacting concrete.

1.1.1. Effect of scrap tire rubber on fresh properties of concrete

Researchers who focused on the mechanical properties of fresh concrete reported that using crumb rubber has a direct impact on lowering the fresh density and workability and increasing the air-entrainment (Najim and Hall 2010, Najim and Hall 2012, Gou and Liu 2014). These results were due to the rubber particles' low specific gravity and increasing air contents. Researchers found that slump was reduced when crumb rubber was used in concrete (Khatib and Bayomy 1999, Siddique and Naik 2004, Sukontasukkul and Chaikaew 2006, Gou and Liu 2014, Moustafa and ElGawady 2015). In addition, it was reported also that there is a rubber content threshold. Before that threshold, adding rubber will increase slump values due to the hydrophobic nature of rubber

which causes a water film coating on the rubber particles, reducing the friction with other particles. Beyond the threshold, the low unit weight of the rubber causes a reduction in slump (Siddique and Naik 2004, Sukontasukkul and Chaikaew 2006, Gou and Liu 2014). It is worth noting that the air content was higher in rubberized concrete than in reference mixtures without rubber (Fedroff et al. 1996).

1.1.2. Effect of scrap tire rubber on hardened properties of concrete

Both the compressive and flexural strengths were negatively affected when crumb rubber was used as one of the constituents of the concrete mixture due to rubber's relatively low stiffness and the poor bond between the rubber particles and cement paste (Siddique and Naik 2004, Batayneh et al. 2008, Najim and Hall 2010, Thomas and Gupta 2013, Gou and Liu 2014, Moustafa and ElGawady 2016, Youssf et al. 2017). On the other hand, the water absorption and the porosity were increased with the increase of rubber content due to the increased air voids which led to a lower unit weight (Siddique and Naik 2004, Onuaguluchi and Panesar 2014).

The effect of the size and shape of rubber particles has been investigated and the results showed that large rubber particles have more influence on reducing the compressive strength than the small particles (Eldin and Senouci 1993, Fattuhi and Clark 1996, Batayneh et al. 2008). Due to the significant reduction in the stress and strain concentration on the rubber particles, it was reported that the elastic modulus of rubberized concrete decreased, and the ultimate strain increased by reducing the rubber particle size.

1.1.3. Effect of scrap tire rubber on ductility and seismic behavior of concrete

Although the compressive strength, flexural strength, and the modulus of elasticity of hardened concrete were decreased with the increase of rubber content, the ductility and toughness of rubberized concrete were higher than that of conventional concrete (Ganjian et al. 2009, Ho et al. 2012).

From the seismic and dynamic load perspective, significant improvements were recorded in the energy dissipation, viscous damping, enhanced strain rate effect, and hysteretic damping properties when rubber replaced mineral aggregate in concrete. Rubberized concrete displayed higher energy dissipation, viscous damping and hysteretic damping compared with the corresponding conventional concrete (Hernandez-Olivares et al. 2002, Zheng et al. 2008, Xue and Shinozuka 2013, Moustafa and ElGawady 2015, Youssf et al. 2015, Youssf et al. 2016, Moustafa and ElGawady 2017, Moustafa et al. 2017). Rubberized concrete was proposed as a structural material in high seismic regions to enhance energy dissipation capabilities, a crucial feature (Xue and Shinozuka 2013). Atahan and Yücel (2012) performed dynamic drop-weight tests to assess the effect of rubber on energy dissipation. They determined that replacing 20-40% of aggregates with crumb rubber creates concrete mixtures that are useful for concrete barriers. Moustafa and ElGawady (2017) used free vibration tests with an impact hammer on simply supported beams to investigate the concrete's dynamic properties. They reported that both the viscous damping and the average hysteresis damping increased as the rubber content increased. Moustafa et al. (2018), using shaking table testing, found that the energy dissipation and viscous damping of bridge columns constructed using rubberized concrete were higher than those of columns constructed using conventional concrete.

1.1.4. Effect of scrap tire rubber on durability of concrete

Rubberized concrete exhibited better freeze and thaw durability compared to conventional concrete mixtures (Savas et al. 1997, Benazzouk and Queneudec 2002, Richardson et al. 2016). In addition, anti-sulfate corrosion was enhanced with the use of rubber in concrete (Yung et al. 2013, Thomas and Gupta 2015, Liu et al. 2016, Thomas et al. 2016). The same trend was noticed when recycled rubber was used in concrete masonry (Gheni et al. 2017).

Using crumb rubber helped to produce more durable concrete by enhancing the abrasion resistance, frost resistance, acid attack and chloride ion penetration (Richardson et al. 2012, Zhu et al. 2012, Gesoğlu et al. 2014, Richardson et al. 2016, Thomas and Gupta 2016); however, the effect of rubber on carbonation resistance varied based on the rubber content (Gesoğlu and Güneyisi 2011, Gupta et al. 2014).

1.1.5. Thermal and acoustic behavior of rubberized concrete

The influence of using rubber on the thermal characterization of concrete was a function of the rubber content and particle size (Abu-Lebdeh et al. 2014, Fadiel et al. 2014, Kashani et al. 2017). As the rubber content increases, the thermal conductivity of concrete decreases due to the relatively low thermal conductivity of rubber compared to concrete and the accompanying entrapped air that has been created with the presence of rubber particles (Turgut and Yesilata 2008, Sukontasukkul 2009, Hall et al. 2012). Using a larger size of rubber particle in the production of rubberized gypsum board resulted in a better reduction in the thermal conductivity; the same trend was reported with cement mortar as well (Fadiel et al. 2014). It was reported that composite concrete and scrap tire rubber walls increased the thermal insulation of a model room by 11% (Yesilata et al. 2011). Using granulated rubber in the concrete of flooring and foundations was enough to help low-rise dwellings meet the UK Building Regulations in term of thermal insulation without the need for any additional insulating layers (Paine and Dhir 2010).

In terms of cutting the heating energy consumption, a reduction of 45% was achieved when 37% of the natural aggregate in masonry units was replaced with crumb rubber (Gheni et al. 2017). Varied thicknesses of thermally insulating materials were used as an energy retrofitting material to improve the fire resistance of masonry walls, and it was shown that increasing the thickness resulted in more effective thermal retrofitting (Triantafillou et al. 2017). The effectiveness of any thermal retrofitting material can be influenced by several factors such as the material orientation,

climate, and type and thickness of materials (Huang et al. 2013). Applying the thermal retrofitting system on both external and internal faces of masonry walls has a positive impact on cutting the energy consumption. Furthermore, applying the thermal insulation system externally caused an extra 8% cut in the energy consumption compared to the internally applied thermal insulation (Kolaitis et al. 2013).

Rubberized concrete has the ability to perform better than a conventional concrete in terms of sound insulation. A higher noise reduction coefficient and sound insulation were achieved by using rubberized concrete (Turgut and Yesilata 2008, Hall et al. 2012, Mohammed et al. 2012, Abu-Lebdeh et al. 2014, Gheni et al. 2017, Gheni et al. 2017, Kashani et al. 2017, Zhang and Poon 2018).

1.1.6. Utilizing scrap tire rubber in concrete masonry

Researchers have shown that crumb rubber can be used to replace mineral aggregate leading to more environmentally friendly construction practices (Papagiannakis and Lougheed 1995, Hanson et al. 1996, Amirkhanian 2001, Shuler 2011, Rangaraju and Gadkar 2012, Moustafa and ElGawady 2015, Youssf et al. 2016). In the last 10 years, more than 1,000 paper have been published in Scopus-indexed journals related to masonry units. The term “eco-efficient” was mentioned in only 0.3% of those papers, meaning that the eco-efficient concept has not yet successfully entered in the masonry research field (Pacheco-Torgal et al. 2014). More than 4.6 billion CMUs were produced in the United States in 2014, a nearly 12% increase over the past year. However, CMUs are currently manufactured using conventional materials that have a negative impact on the environment. In addition, CMUs are a quite brittle material. Hence, there is a pressing need to produce more ductile and sustainable CMUs. Replacing the natural fine aggregates with crumb rubber produced from scrap tires has the potential to address both issues.

Very few studies investigated the effect of adding crumb rubber to masonry units as a replacement of natural aggregates producing what is known as rubberized concrete masonry units (RCMUs). Both load-bearing and non-load-bearing rubberized masonry hollow blocks and bricks, where mineral aggregates were partially replaced with crumb rubber, were produced (Isler 2012, Mohammed et al. 2012, Sadek and El-Attar 2015). Previous researchers focused on finding a new home for recycled rubber while attempting to match the mechanical characterizations of conventional masonry. However, the research described in this report utilized a different approach, attempting to employ the unique features of rubber to improve the physical and mechanical properties of masonry units to result in a high-performance material.

1.1.7. Utilizing scrap tire rubber in pavement

Transportation infrastructure is a major contributor to global greenhouse gas emissions, responsible with 23% of global carbon dioxide (CO2) emissions, which makes it the second largest contributor, only behind electricity generation (Ang and Marchal 2013). As a result, using recycled material in construction of the transportation infrastructure will help to cut the (CO2) emissions significantly. Previous studies used crumb rubber as an asphalt binder modifier, which improves the general performance of the binders in terms of temperature susceptibility, viscosity, and stiffness(Lee et al. 2008, Presti 2013).

The processes of applying crumb-rubber modifier (CRM) in asphalt mixtures includes blending asphalt cement with crumb rubber at a high temperature, ranging from 177 to 210° C. The Federal Highway Administration (FHWA) and many state agencies have conducted numerous field studies for the feasibility of using recycled rubber tire products in asphalt pavements. The National Cooperative Highway Research Programs (NCHRP) provides a comprehensive review of using recycled rubber tires in highways based on a review of nearly 500 references and information recorded from state highway agencies' responses to a 1991 survey of practices (Epps

and Mason 1994). Florida DOT began constructing demonstration projects of asphalt pavement using crumb rubber modified asphalt (CRMA) in 1989 and has reported satisfactory pavement performance (Page 1992). It concluded that the addition of CRM would increase the asphalt film thickness, binder resiliency, viscosity, and shear strength. Virginia DOT constructed CRMA produced by two wet processes and compared the pavement performance to that of conventional asphalt mixtures. Maupin (Maupin Jr 1996) reported that the mixes containing asphalt rubber performed at least as well as conventional mixes. In Virginia mixes, the inclusion of asphalt rubber in hot-mix asphalt (HMA) pavements increased construction cost by 50–100 percent as compared to the cost of conventional mixes. Troy et al. (Troy et al. 1996) conducted a research on CRM pavements in the state of Nevada. In their study, they evaluated a CRM binder using the Superpave binder testing protocols and conducted the mix design using the Hveem procedure. They concluded that the conventional sample geometry in Superpave binder test protocols cannot be used to test the CRM binders and that the Hveem compaction is inadequate for mixtures containing CRM binders.

Gheni et al. (2018) proposed a new approach to recycle crumb rubber. Crumb rubber was used as an aggregate replacement (not binder modifier) in chip seal. Chip seal is a layer of surfacing treatment that is constructed by spreading binder followed by a uniform layer of aggregate. Rollers are used after that to embed the aggregate into the binder. Chip seal plays an excellent role in resisting tire damage and creates a macrotexture that provides a good skid-resistant surface to ensure a safe driving atmosphere (Gransberg and James 2005). In addition, chip seal has been widely used for preventive road maintenance to prevent further surface deterioration. One important feature that makes chip seal competitive with other maintenance techniques is its affordability (Gransberg and James 2005, Karasahin et al. 2014).

1.2. Report organization

This report is built upon the recently concluded project at Missouri S&T (Gheni et al. 2017), where preliminary study was conducted on rubberized masonry units. This project focused on an experimental work that utilized and optimized scrap tire rubber as a replacement for the natural aggregate in concrete masonry units and structures.

This report includes six chapters summarizing the literature review and experimental work on rubberized masonry units. Appendices are provided where detailed information about testing and raw data is summarized. In particular, Chapter 1 includes a brief introduction to the subject area, the objectives and scope of the project, and a literature review establishing the state-of-the-art of the research area. Chapter 2 focuses on optimizing the production presses, the size of rubber particles, and the rubber replacement ratios. Based on these parameters, rubberized concrete masonry units (RCMU) were produced both in the lab and in a plant setting. The mechanical properties of the new RCMUs were examined as well. Chapter 3 describes the impact of incorporating crumb rubber within the RCMU matrix on the durability of the new units and structure. Different durability aspects of both masonry units and plastering mortar were examined in this chapter. Chapter 4 presents the thermal and acoustic behavior of the new proposed RCMUs using different measurements for thermal and sound conductivity and details the impact of using RCMUs on energy consumption for heating and cooling. Chapter 5 presents the seismic and cyclic behavior of rubberized masonry prisms and full-scale structural elements and the benefits of incorporating crumb rubber within the masonry structure in terms of responding to seismic and cyclic loads. Finally, Chapter 6 presents the key findings of all experiments that were executed during this research study as well as a proposal for future research.

2. Optimization of Mixtures and Production of RCMUs.

This chapter presents the optimum material and production process parameters required for manufacturing RCMU with high density leading to high compressive strength. The material parameters included sand-to-solid materials ratio, rubber-to-sand ratio, and rubber particle size. The production process parameters included the required pressure and vibration.

2.1. Optimizing the compaction pressure and vibration.

A gyratory compactor (Figure 2.1) was employed to determine the highest packing density of different mixtures with varied aggregate combinations leading to the highest compressive strength of a CMU. Several trial runs, with pressures from 15 psi to 44 psi, were investigated under gyratory cycles ranging from 0 to 500, to optimize the proper pressure for each mixture to obtain the optimum density.

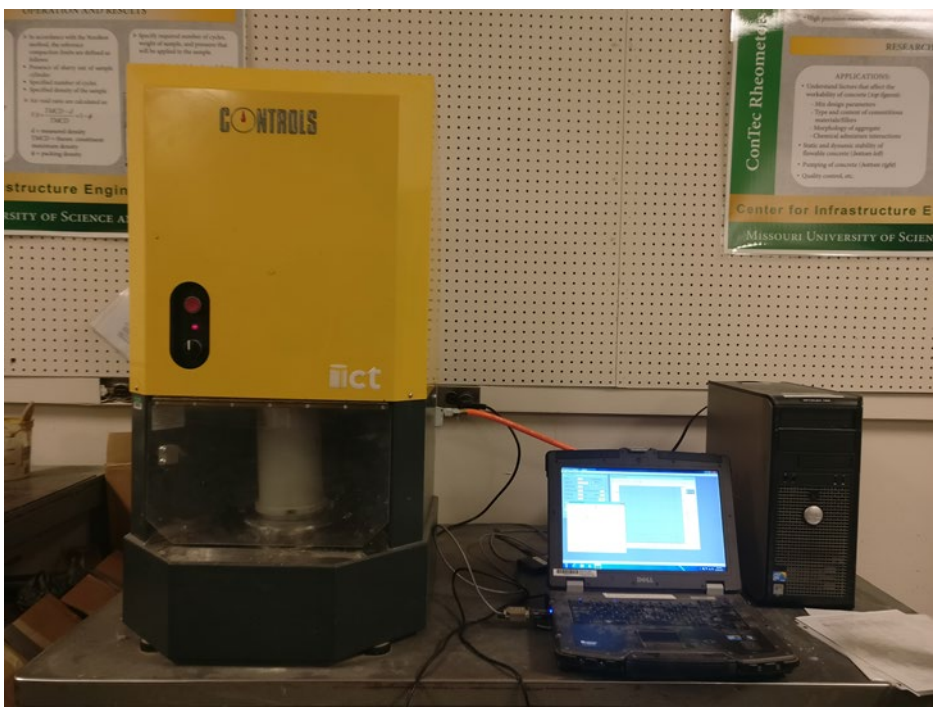

Figure 2.1: Gyratory compactor employed for determining the packing density of aggregate combinations.

Figure 2.2 to 2.5 display the densities of dry mixtures of RCMU having sand-to-solid material ratios ranging from 40% to 70% subjected to different pressures and gyratory cycles. It was concluded from these figures that a pressure of 30 psi resulted in the highest density compared to other options.

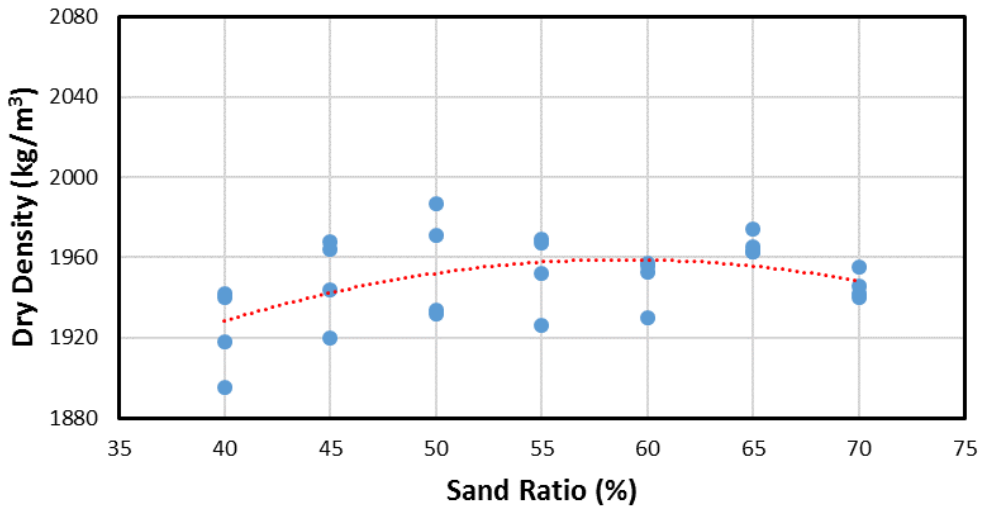

(a)

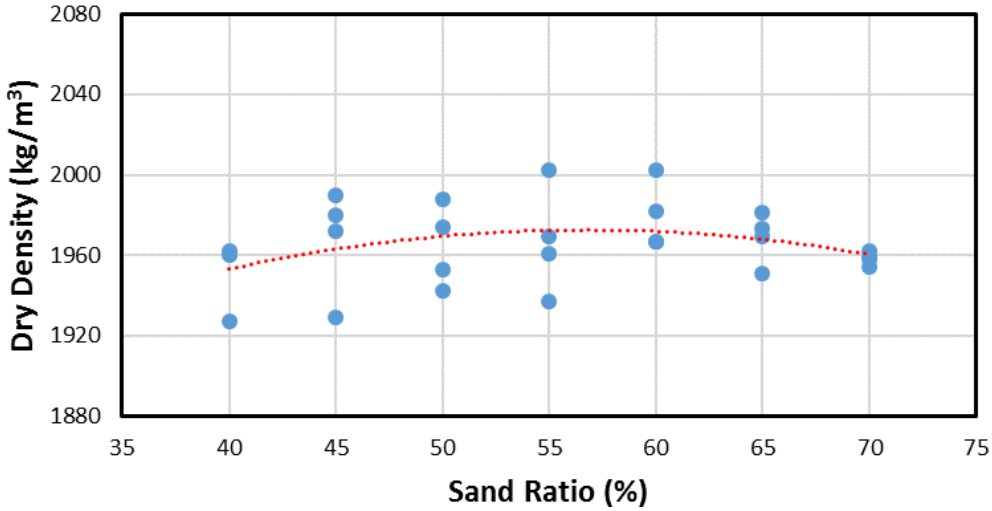

(b)

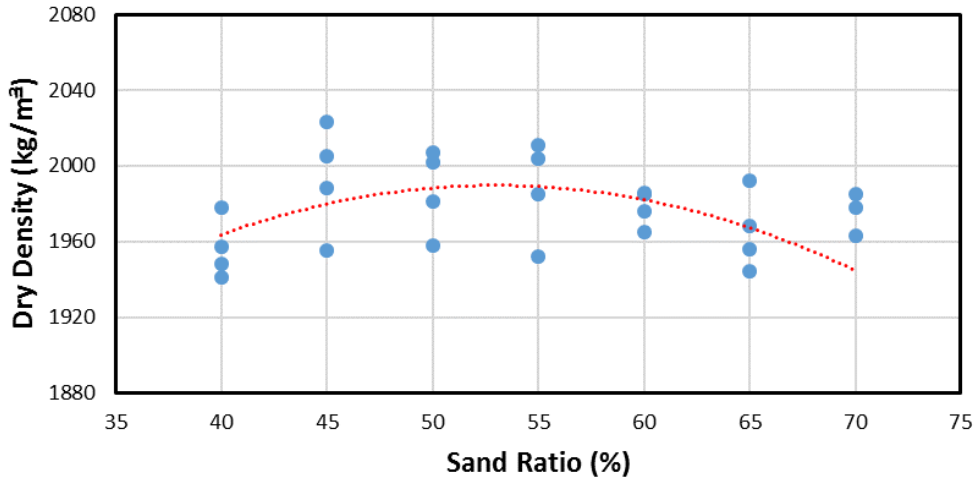

(c)

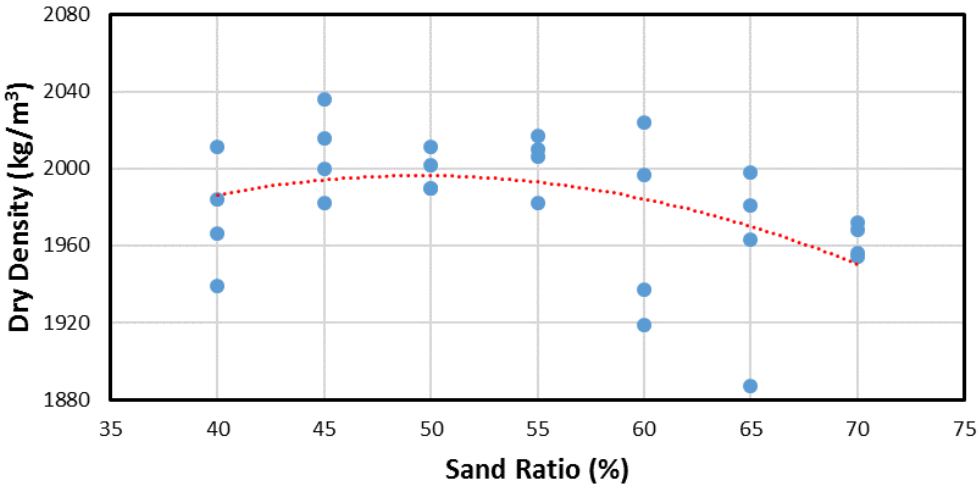

(d)

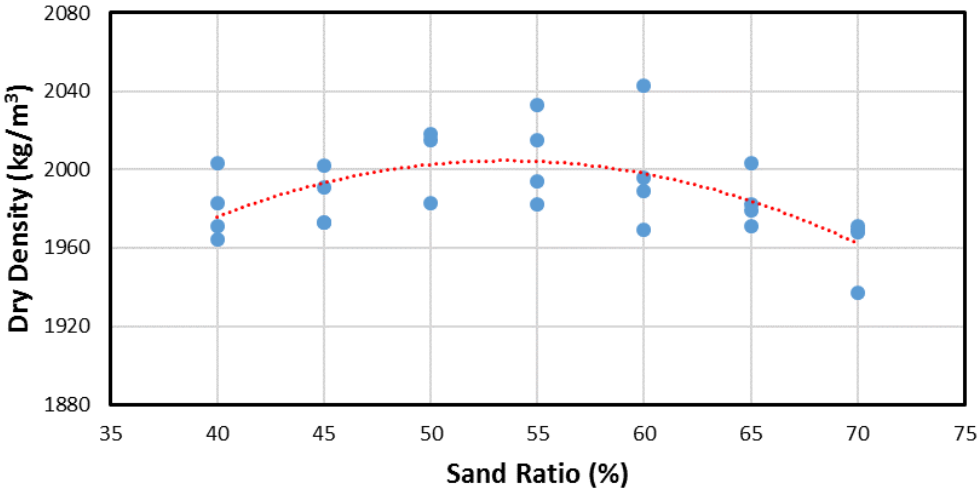

(e)

Figure 2.2: The relationship between sand-to-solid materials ratio and the density of the solid components of CMU mixtures after 220 gyratory cycles under compaction pressure of: (a) 15 psi, (b) 22 psi, (c) 30 psi, (d) 36 psi), and (e) 44 psi.

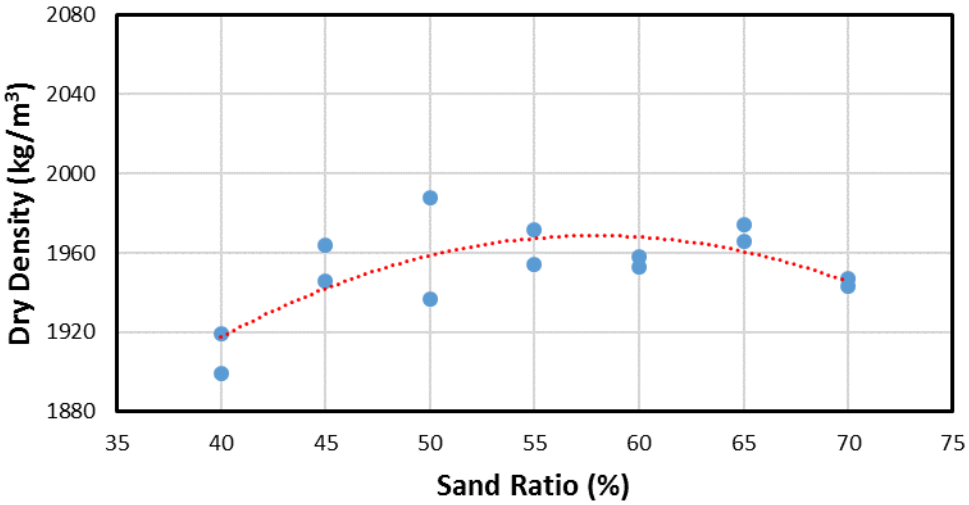
2080
2040
2000
1960
1920
1880
Dry Density (kg/m³)
35
40
45
50
55
60
65
70
75
Sand Ratio (%)

(a)

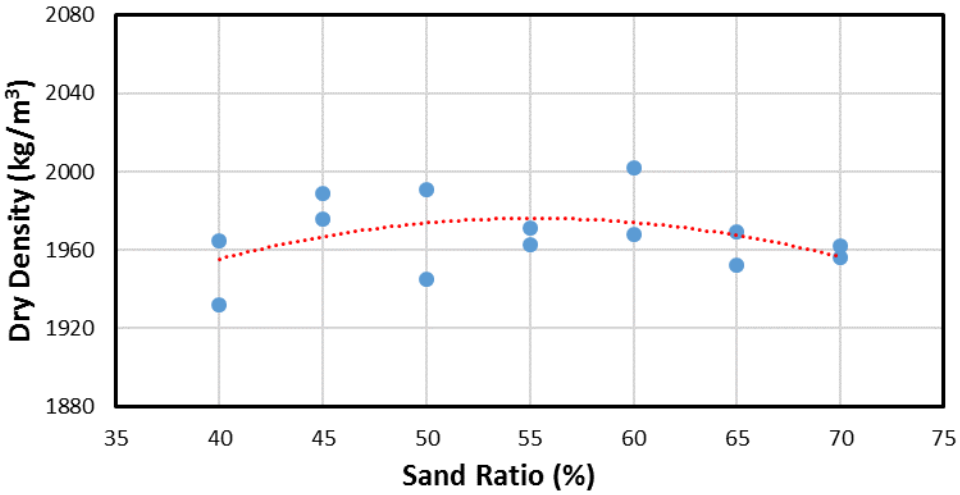
2080
2040
2000
1960
1920
1880
Dry Density (kg/m³)
35
40
45
50
55
60
65
70
75
Sand Ratio (%)

(b)

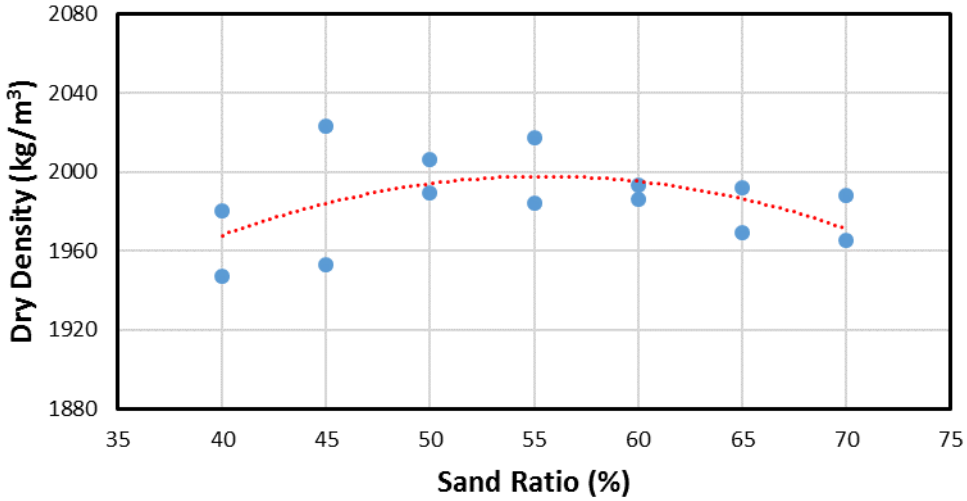
2080
2040
2000
1960
1920
1880
Dry Density (kg/m³)
35
40
45
50
55
60
65
70
75
Sand Ratio (%)

(c)

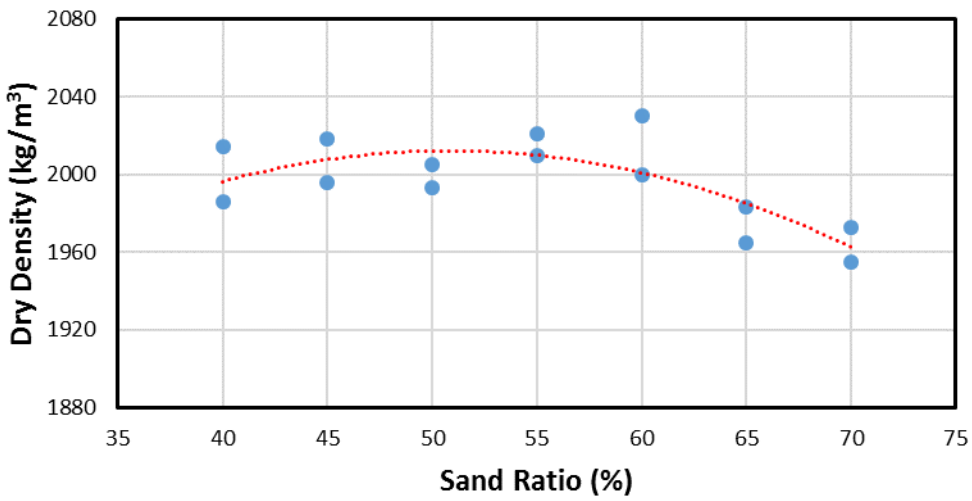

(d)

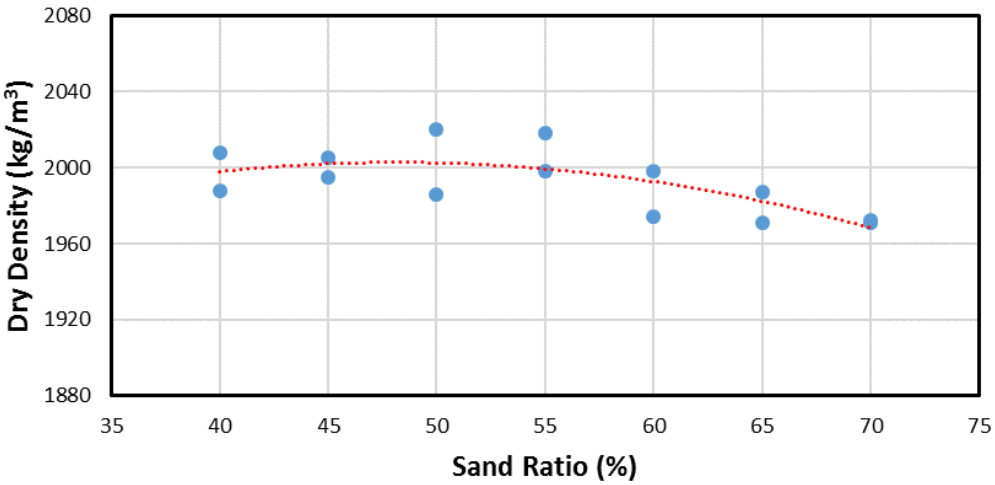

(e)

Figure 2.3: The relationship between sand-to-solid materials ratio and the density of the solid components of CMU mixtures after 350 gyratory cycles under compaction pressure of: (a) 15 psi, (b) 22 psi, (c) 30 psi, (d) 36 psi), and (e) 44 psi.

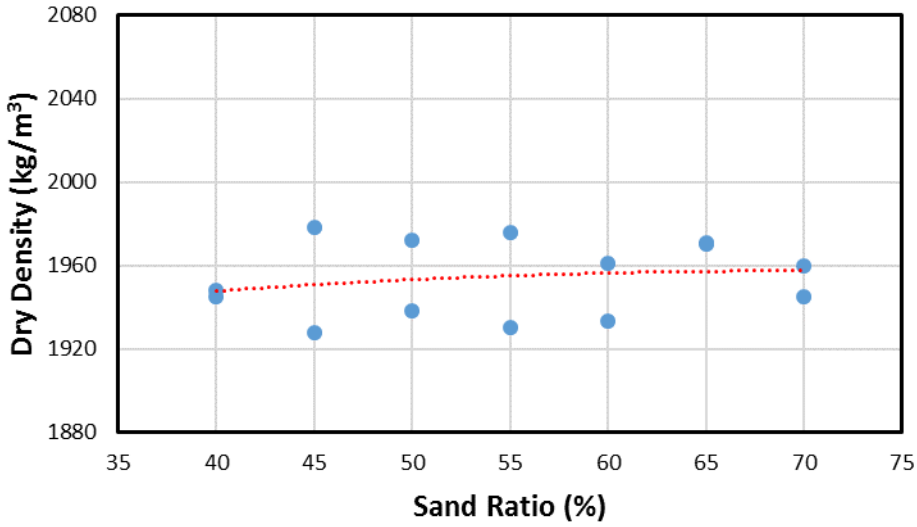
2080
2040
2000
1960
1920
1880
Dry Density (kg/m³)
35
40
45
50
55
60
65
70
75
Sand Ratio (%)

(a)

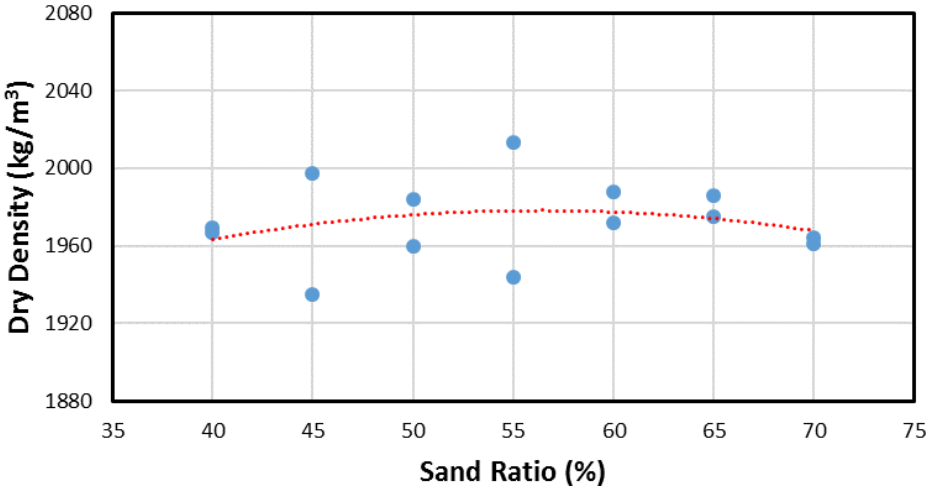
2080
2040
2000
1960
1920
1880
Dry Density (kg/m³)
35
40
45
50
55
60
65
70
75
Sand Ratio (%)

(b)

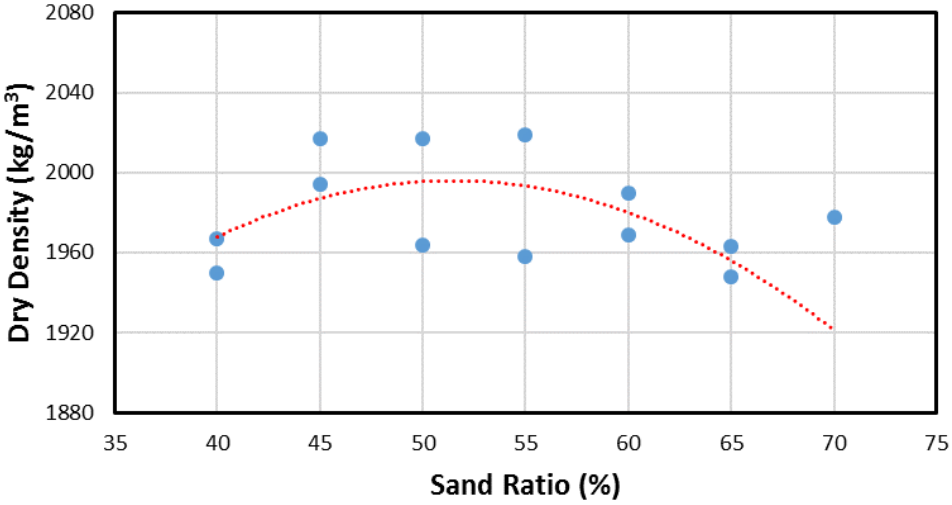
2080
2040
2000
1960
1920
1880
Dry Density (kg/m³)
35
40
45
50
55
60
65
70
75
Sand Ratio (%)

(c)

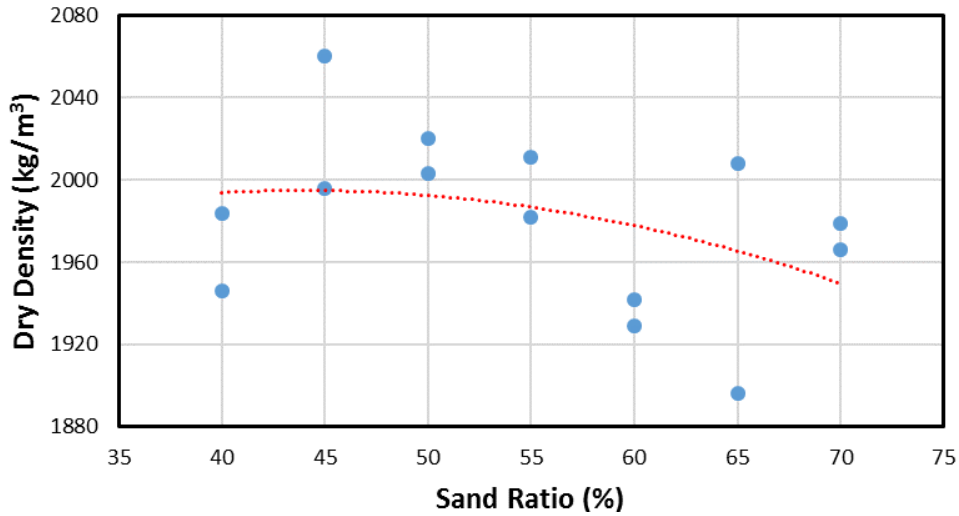

(d)

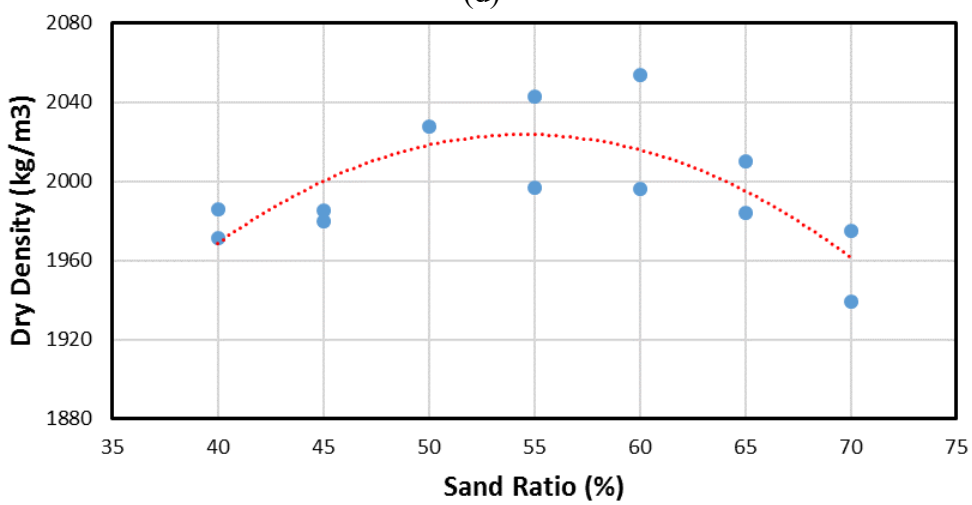

(e)

Figure 2.4: The relationship between sand-to-solid materials ratio and the density of the solid components of CMU mixtures after 400 gyratory cycles under compaction pressure of: (a) 15 psi, (b) 22 psi, (c) 30 psi, (d) 36 psi), and (e) 44 psi.

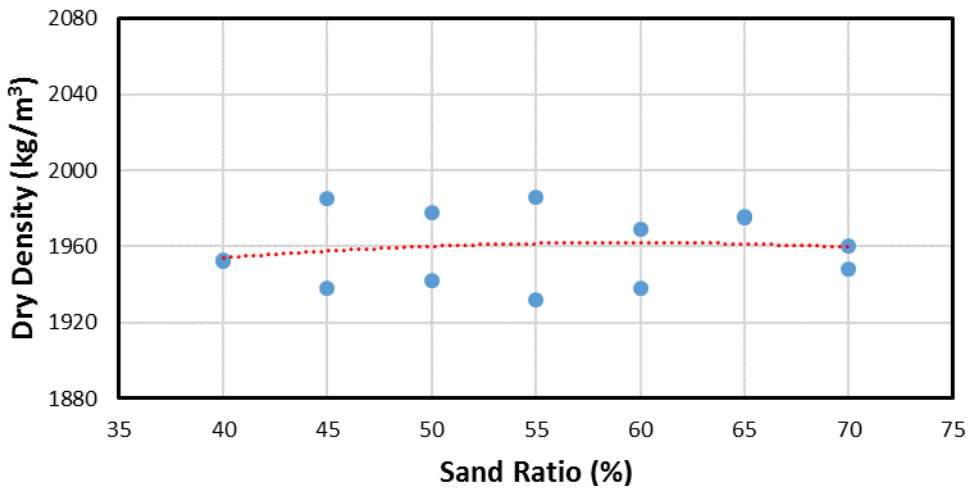
2080
2040
2000
1960
1920
1880
Dry Density (kg/m³)
35
40
45
50
55
60
65
70
75
Sand Ratio (%)

(a)

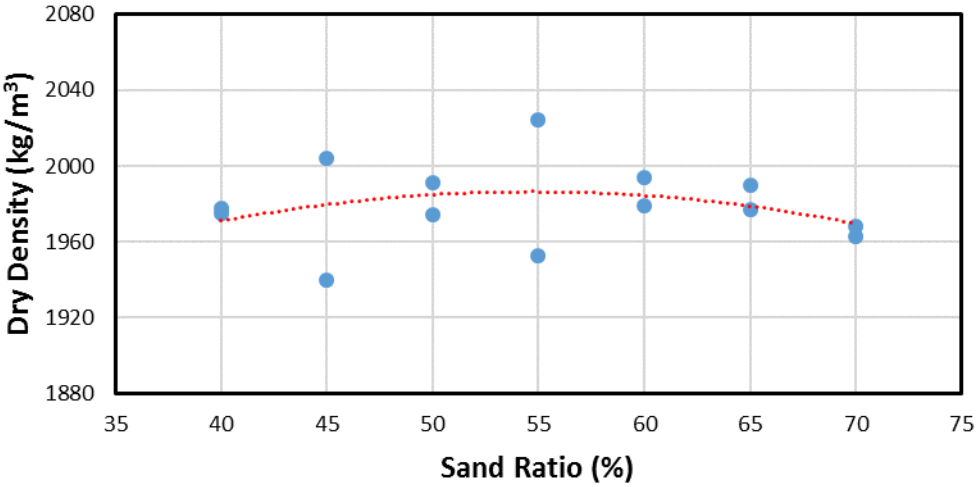
2080
2040
2000
1960
1920
1880
Dry Density (kg/m³)
35
40
45
50
55
60
65
70
75
Sand Ratio (%)

(b)

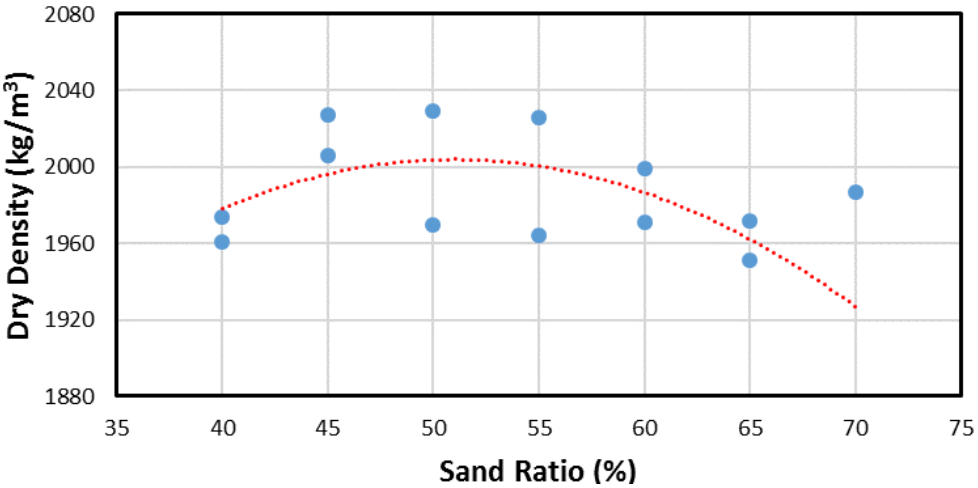
2080
2040
2000
1960
1920
1880
Dry Density (kg/m³)
35
40
45
50
55
60
65
70
75
Sand Ratio (%)

(c)

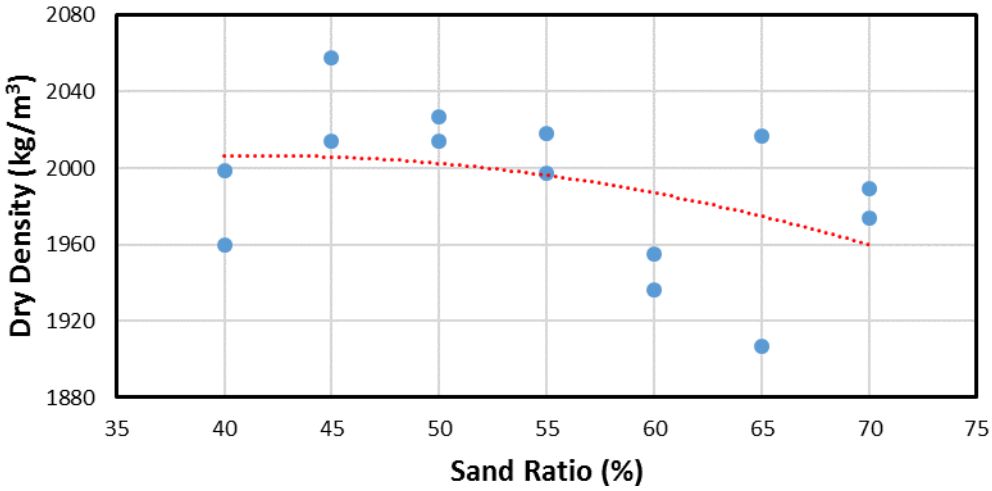

(d)

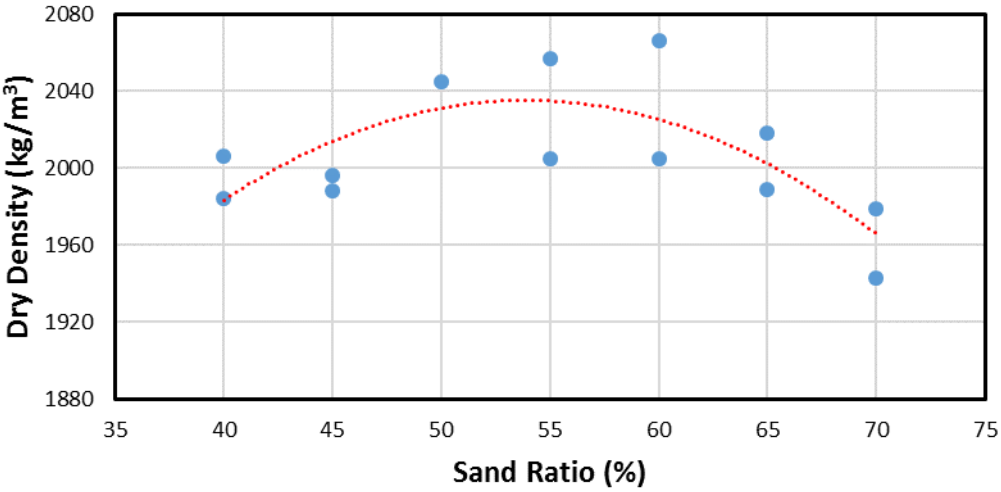

(e)

Figure 2.5: The relationship between sand-to-solid materials ratio and the density of the solid components of CMU mixtures after 500 gyratory cycles under compaction pressure of: (a) 15 psi, (b) 22 psi, (c) 30 psi, (d) 36 psi), and (e) 44 psi.

In terms of the number of the gyratory cycles (Figure 2.6), the density significantly increased up to 50 gyratory cycles; beyond that the density increased with an increase in the number of gyratory cycles but at much smaller rate. The density reached its peak and remained approximately constant after 500 gyratory cycles. Therefore, a pressure of 30 psi and gyratory cycles of 500 were adopted in the rest of this investigation.

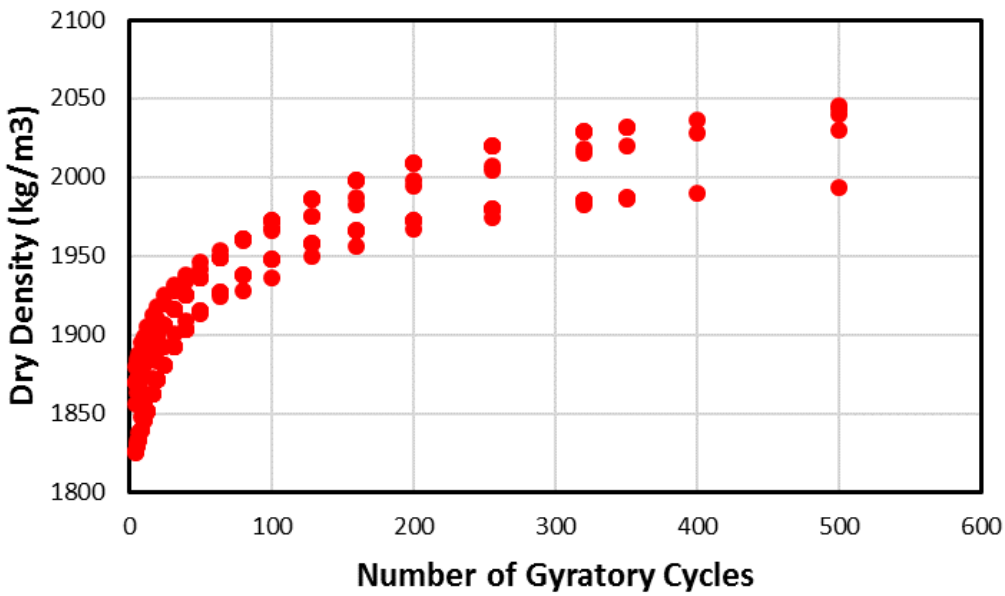

Figure 2.6: The relation between number of gyratory cycles and density of the solid components of concrete masonry mixture under compaction pressure of 2 bar (30 psi).

In terms of the best sand-to-solid materials ratio, in addition to the results presented in Figures 2.2 through 2.5, Figure 2.7 shows that sand-to-solid materials ratio of 50% produced the highest dry density compared to the other sand ratios under pressure of 30 psi and 500 gyratory cycles.

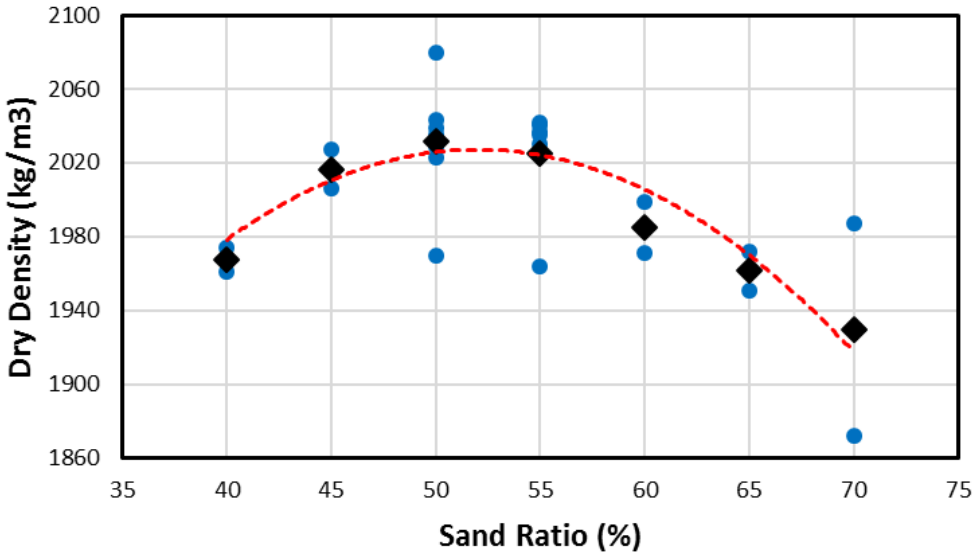

Figure 2.7: The relationship between sand-to-solid materials ratio and density of the solid components of CMU mixture after 500 gyratory cycles under compaction pressure of 30 psi.

2.2. Optimizing crumb rubber size and ratio.

Crumb rubber is currently produced in sizes that can be classified into fine materials, fine aggregate, and coarse aggregate, which allow users to replace any of the material components of concrete with crumb rubber without changing the overall gradation of the dry components. Previous studies concluded that rubberized concrete having a relatively small size crumb rubber resulted in a higher compressive strength compared to those with relatively large crumb rubber particles. In a previous study, the authors of this report used crumb rubber having a size of 2.83 mm to 4.00 mm (Figure 2.8a) to develop RCMUs (Gheni et al. 2017). Building upon that with an intension to use a smaller size of rubber to reach better performance, during the course of this project, the authors investigated new mixtures with crumb rubber particles smaller than 2.83 mm. Thus, three sizes of crumb rubber particles were examined with each replacement ratio. Based on the smallest and the largest size in each grade, the examined sizes are 2.83-0.841 mm. (Figure 2.8b), 0.30-0.15 mm. (Figure 2.8c), and smaller than 0. 075 mm. (Figure 2.8d).

This task of the project investigates the optimum crumb rubber ratio that can be used as a partial replacement for the sand. Based on a previous investigation (Gheni et al. 2017), RCMU that meets the ASTM's C90-12 compressive strength requirements can be produced with a crumb rubber ratio up to 20%. As a result, crumb rubber ratios of 0%, 5%, 10%, 15%, and 20% were examined for their impact on the dry density of the RCMU mixtures during this study. For each ratio, three different sizes were investigated. Figure 2.9 shows the relation between the ratio of crumb rubber as a sand replacement and the dry density of the RCMU mixtures. As shown in the figure, replacing 5% of the sand with crumb rubber having a size of 2.83-0.841 mm resulted in the highest dry density compared to the other two crumb rubber sizes. Therefore, this size was adopted in the production of RCMUs for the rest of this project.

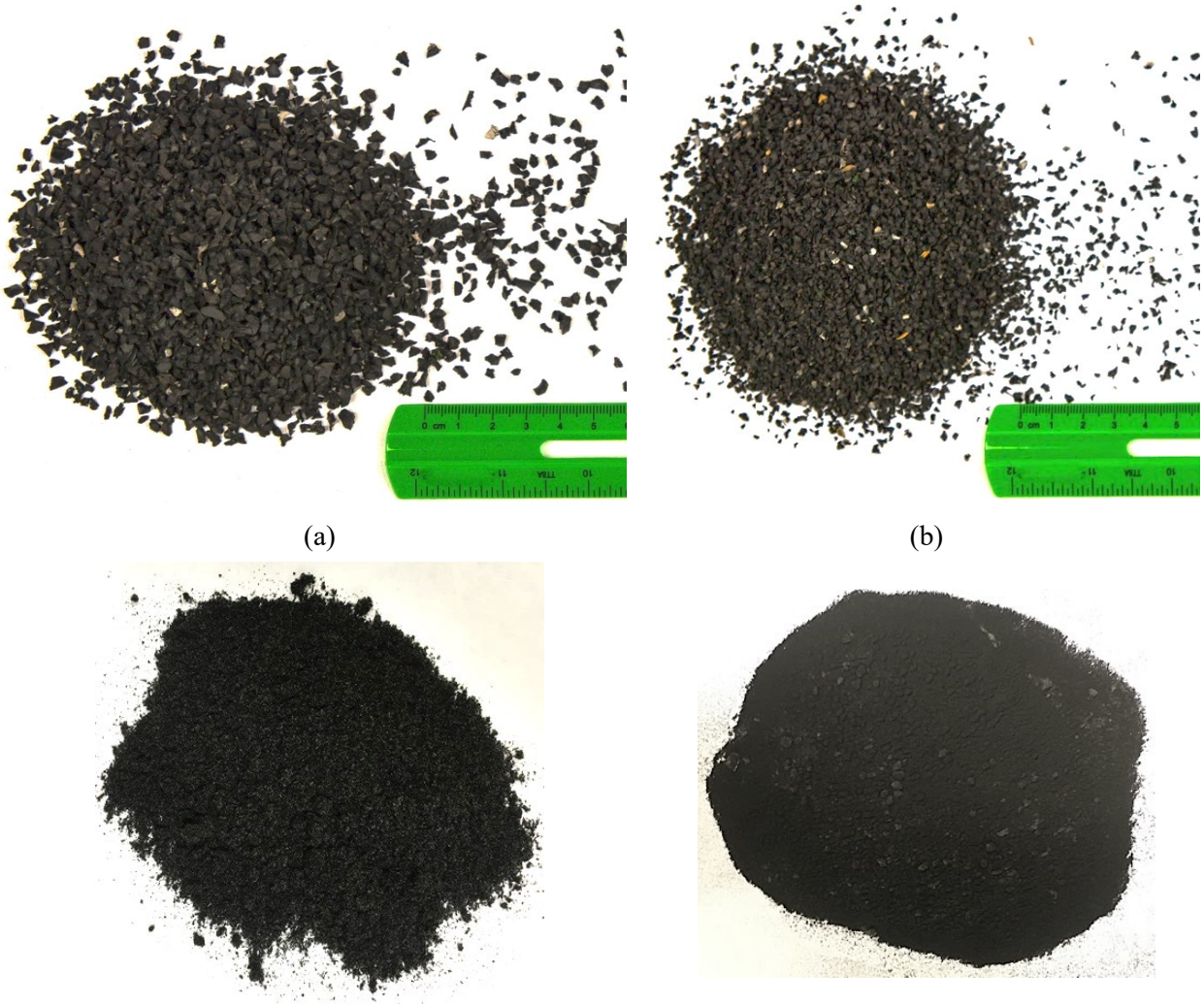

(a) (b)

(c) (d)

Figure 2.8: Different rubber sizes: (a) 4.0 to 2.83 mm, (b) 2.83-0.841 mm., (c) 0.30-0.15 mm., and (d) Smaller than 0. 075 mm.

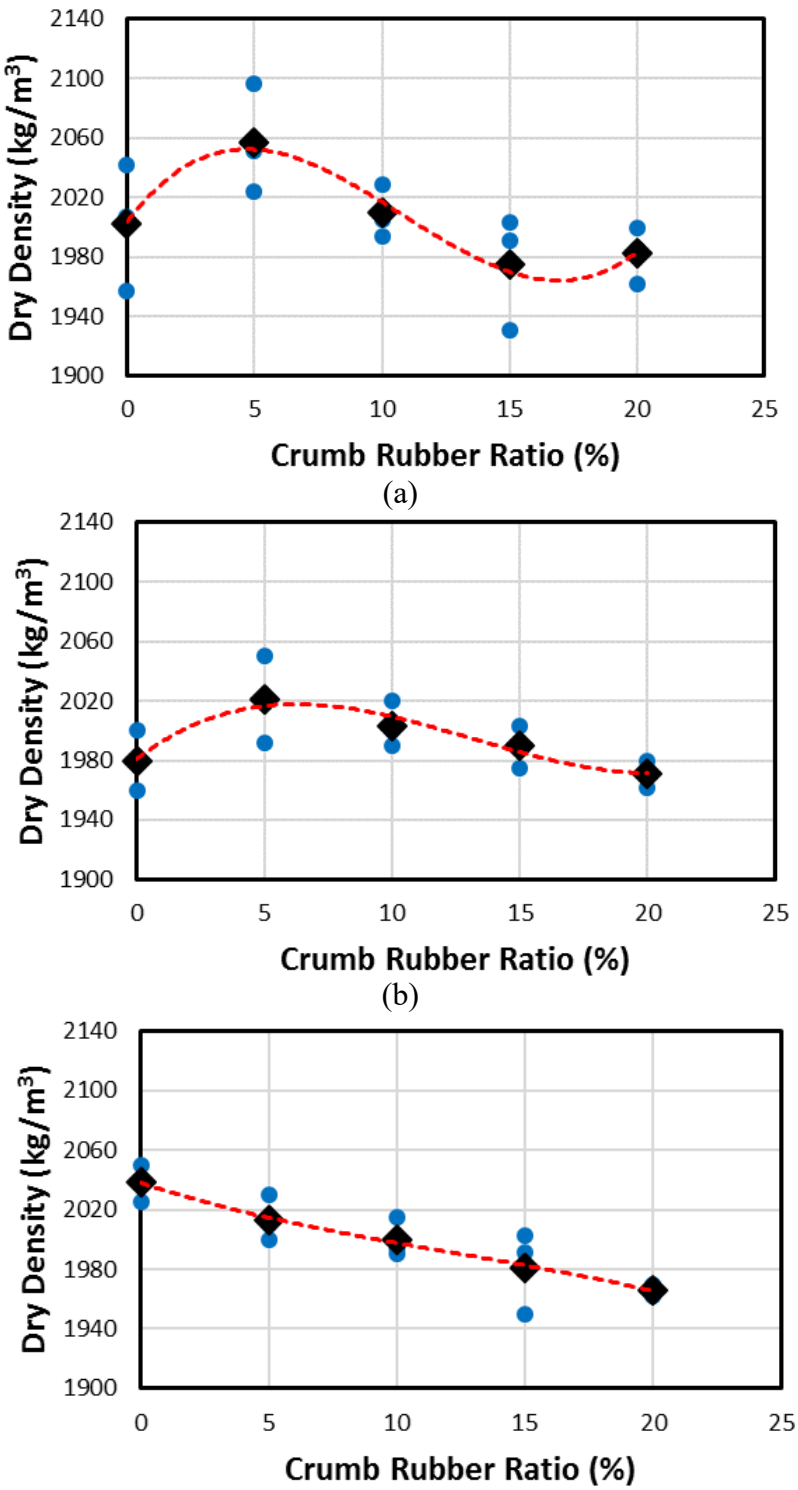

Figure 2.9: The relationship between crumb rubber ratio and density of the solid components of RCMU mixture after 500 gyratory cycles under compaction pressure of 30 psi with rubber having particle sizes of: (a) 2.83 - 0.841 mm, (b) 0.30 - 0.15 mm, and (c) Smaller than 0. 075 mm.

2.3. Production of trial RCMUs in the lab.

Based on the conclusion of the first part of this study relating to the optimum compacting pressure and gyration, sand ratio, and crumb rubber size, four mixtures were designed that contain 0%, 5%, 10%, and 15% rubber. In addition to the obtained optimized parameters, and to facilitate the mass production at Midwest Brick and Block masonry production plant, their exact same materials and admixtures were used during the mix design (Table 2.1).

Table 2.1: RCMUs lab trial mix design (lb)

	0% Rubber	5% Rubber	10% Rubber	15% Rubber
Type I-II Portland Cement	15.25	15.25	15.25	15.25
Fly Ash	2.028	2.028	2.028	2.028
Masonry Sand	87.71	83.32	78.94	74.55
Washed Chat	54.65	54.65	54.65	54.65
Crumb Rubber	0.000	1.750	3.510	5.260
MasterCast 900 Additive	0.520	0.520	0.520	0.520
MasterPel 240 Additive	0.184	0.184	0.184	0.184

A shear mixer was used to mix both solid and liquid components with a goal to get a zero-slump mix in all four mixtures (Figure 2.10). The mixing procedure started by mixing all the solid components, followed by the gradual addition of a solution of both water and admixtures (Figure 2.10b).

(a) (b)

Figure 2.10: Mixing the solid and liquid components of RCMU mixtures.

A machine (Figure 2.11) was developed at Missouri S&T to produce CMUs having the same shape and dimensions of the CMUs currently produced by the Midwest Brick and Block masonry plant. The machine also matched the required pressure and vibration according to both the optimized production parameters as well as the CMU manufacturing machine at the Midwest Brick and Block masonry plant. As shown in Figure 2.11a, the machine has an electrical motor that runs the vibrator to the required time and speed. A moment arm that can handle a variable weight at its end was used to apply the required pressure on the CMU mold to shape it with the lowest void content. The mold of the lab machine was modified to match the currently produced CMUs in terms of both shape and dimensions. In addition, since we cannot control the compaction pressure at the mass production facility in Jefferson City, their normal compaction pressure of 16 psi was used in our laboratory machine instead of the optimum pressure that was determined form the first part of this study. The reason behind adapting the pressure from the mass production

facility in Jefferson City was to prepare laboratory mixtures that matched these at the mass production facility in terms of proportions and production conditions.

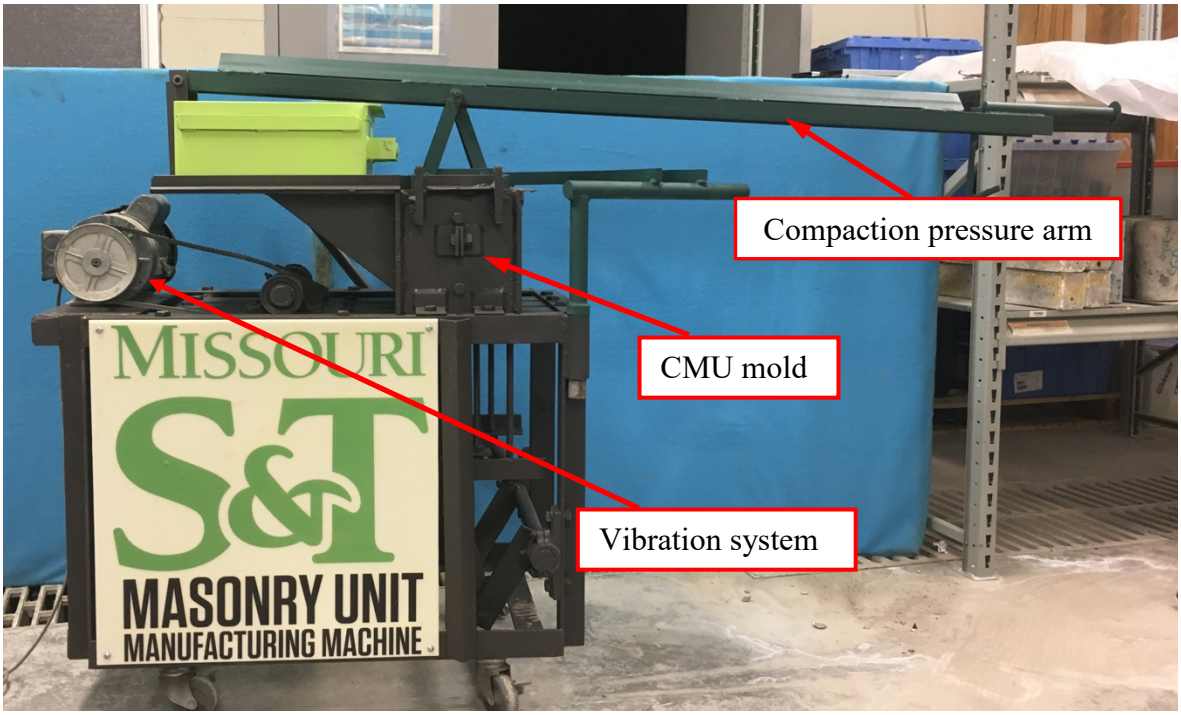

(a)

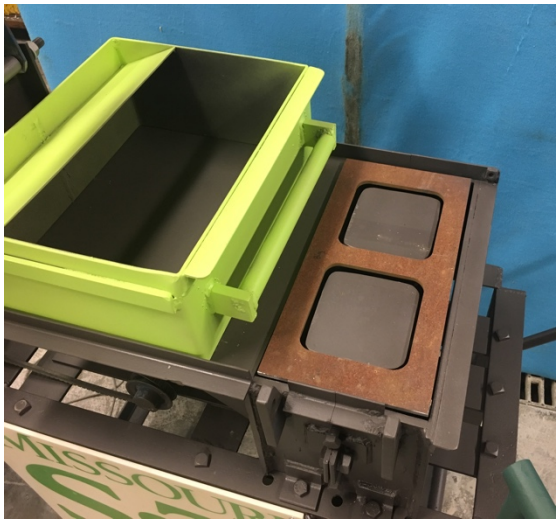

(b)

(c)

Figure 2.11: Masonry units manufacturing lab machine (a) Machine parts, (b) Base plate, and (c) Targeted CMU shape.

The workability of each mixture was measured to ensure zero slump while having enough moisture content to hold and glue the particles together after the compaction and vibration. The required weight of the mix was then moved to the laboratory machine to fill the CMU mold (Figure 2.12a and b) and then vibrated and pressed (Figure 2.12c and d) to achieve the highest possible packing density.

(a) (b) (c) (d) (e) (f)

Figure 2.12: RCMU laboratory manufacturing process: (a and b) Placing the mixture, (c and d) Compaction and vibration, and (e and f) The final shape of the CMU.

The cast CMUs were stacked and labeled on a galvanized metal movable shelf (Figure 2.13a), and after 24 hours they were moved to the curing room (Figure 2.13b) for 28 days before testing their compressive strength.

(a) (b)

Figure 2.13: RCMU laboratory curing: (a) Stocking and labeling the units, and (b) Placing the units inside the curing room.

2.3.1. Compressive strength of the trial RCMUs.

After 28 days of moist curing, the compressive strengths of the RCMUs were tested according to ASTM C140/C140M−14b. For each rubber content ratio, three individual blocks were tested for compressive strength. A fibrous composite laminated cap was placed on the top and bottom of each RCMU to uniformly distribute the load on the block surface and prevent any stress concentration. A rigid 24x12x2 inch loading plate was used to apply the loads (Figure 2.14). The average applied load for each of the three blocks having a given rubber ratio was calculated and used to calculate the compressive strength.

Figure 2.14: Compressive strength test setup.

Figure 2.15 shows the compressive strengths for the RCMUs. For all RCMUs, the compressive strengths were within the limits of ASTM C90-12 for loadbearing concrete masonry units. Therefore, the developed units can be used as load bearing masonry units. Furthermore, the trend of the compressive strength matches the trend of the packing density results in Figure 2.9, where the highest dry density was achieved with a 5% rubber ratio. The RCMU with 5% rubber content yielded the highest compressive strength compared with all investigated blocks including the reference CMU. The compressive strength decreased in the case of 10% and 15% rubber ratios.

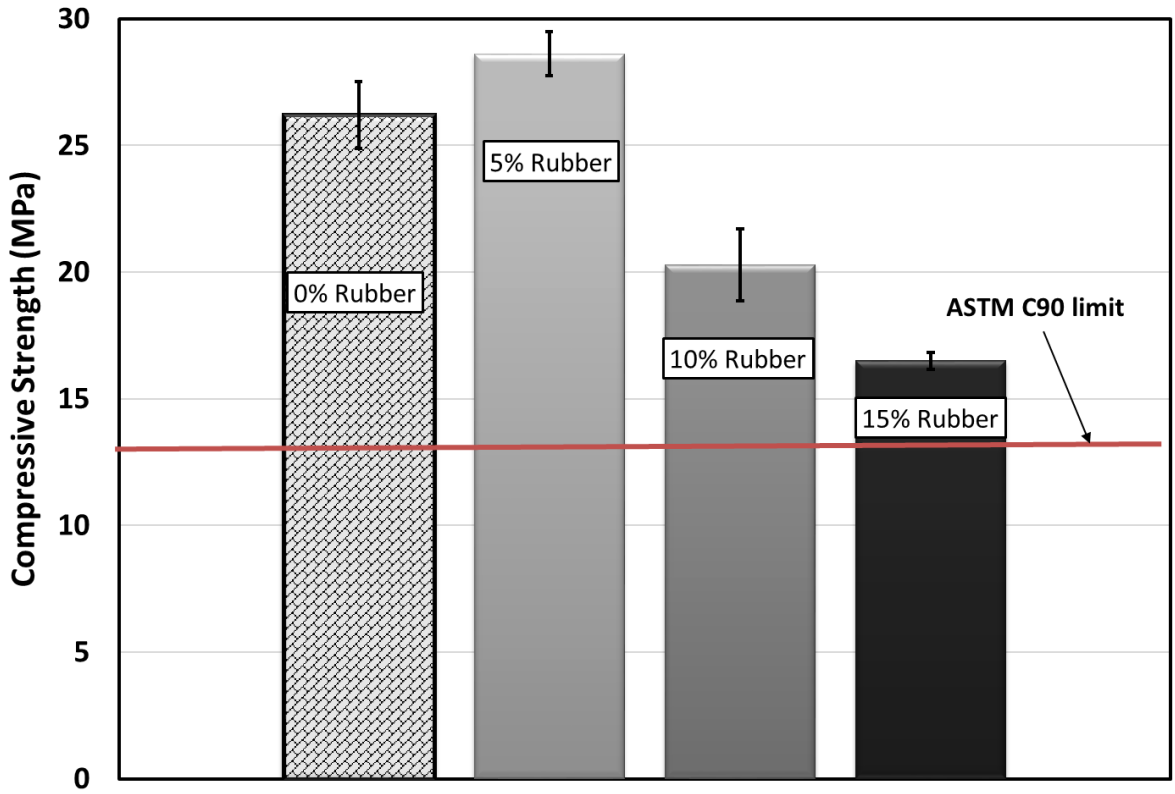

Figure 2.15: Compressive strength of RCMUs produced in the laboratory.

2.4. Production of RCMUs in plant settings.

Based on the successful production of RCMUs in the laboratory, mass production of RCMUs with four rubber ratios, namely 0%, 5%, 10%, and 15%, was performed at the Midwest Brick and Block masonry production plant in Jefferson City, Missouri. The target and actual material proportions used in each mix are presented in Table 2.2.

The conventional daily production process was used to produce RCMUs in the production plant in Jefferson City without any modification, as shown in Figure 2.16. The RCMUs were compacted and vibrated using an automatic hydraulic machine (Figure 2.16a).

An average of 130 RCMUs were cast to satisfy the required number of specimens for all the tests in this report including unit weight, water absorption, compressive strength, durability, freeze and thaw resistance, and thermal conductivity of the units. Tests on RCMU prisms were carried out also to determine the mechanical properties of the RCMU prisms.

Table 2.2: Production Report of RCMUs in Plant Settings (lb)

	0% Rubber		**5% Rubber**		**10% Rubber**		**15% Rubber**	
	Target	Actual	Target	Actual	Target	Actual	Target	Actual
Type I-II Portland Cement	550.0	551.0	550.0	551.0	550.0	553.0	550.0	553.0
Masonry Sand	2700	2778	2498	2560	2367	2415	2235	2285
Washed Chat	1781	1785	1781	1785	1781	1785	1781	1790
Crumb Rubber	0.00	0.00						
MasterCast 900 Additive	15.00	17.00	15.00	16.00	15.00	17.00	15.00	16.00
MasterPel 240 Additive	5.000	5.000	5.000	5.000	5.000	5.000	5.000	5.000

(a) (b)

(c) (d)

Figure 2.16: RCMU production process in a masonry plant in Jefferson City: (a and b) RCMUs after compaction and vibration, (c) Stocking and labeling the units, and (d) Curing the units in the curing room.

2.4.1. Mechanical characterization of RCMUs.

After the curing period, all RCMUs were delivered to Missouri S&T for testing. The mechanical characteristics of RCMUs were examined through testing the unit weight, water absorption, and compressive strength, according to ASTM C140/C140M−14b.

To calculate the absorption, three RCMUs from each different rubber ratio were placed in an oven at 113° C for 25 hours (Figure 2.17). Whenever two successive RCMUs were weighed at intervals of 2 hours and showed an increment of loss not greater than 0.2% of the previous weight, the weight of the specimen was determined. The samples were then left outside the oven until they reached room temperature so that the oven-dry weight (W_d) could be measured. Next, the samples were soaked in a large water container for 24 to 28 hours. The specimens then were removed from the water and weighed while suspended by a metal wire and completely submerged in water to obtain the immersed weight. (W_i). The block was then removed from the water, and all visible water was wiped before obtaining the saturated weight (W_s). The absorption and oven dry density were calculated using equations 2.1 and 2.2, respectively.

$$Absorption, kg/m^3 = \frac{w_s - w_d}{w_s - w_i} * 1000 \quad (2.1)$$

$$Oven\ Dry\ Density, kg/m^3 = \frac{w_d}{w_s - w_i} * 1000 \quad (2.2)$$

Where W_s = saturated weight of specimen, kg,

W_i = immersed weight of specimen, kg, and W_d = oven-dry weight of specimen, kg.

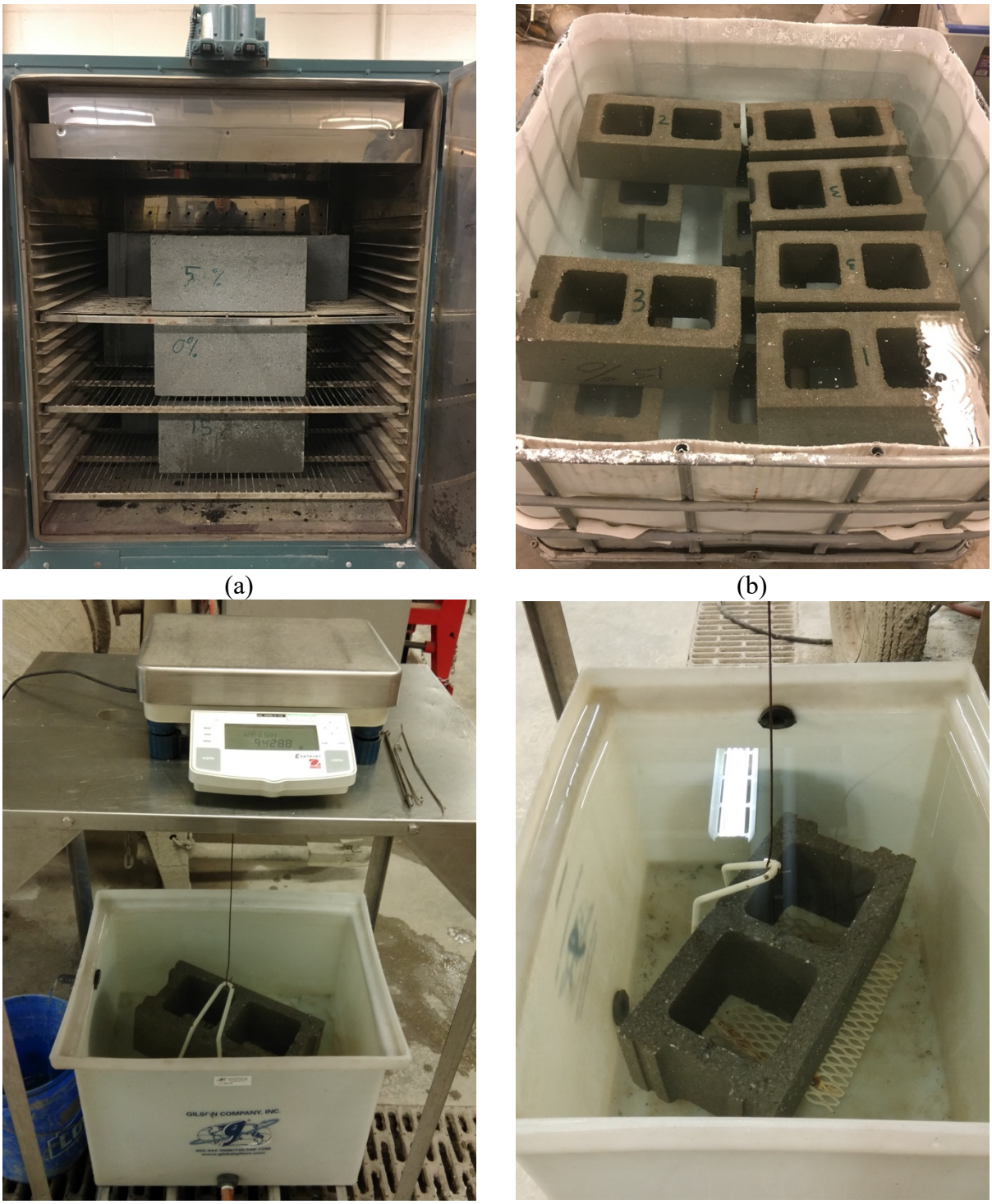

(a) (b) (c) (d)

Figure 2.17: Water absorption and density tests: (a) Drying the RCMUs in the oven, (b) Soaking the RCMUs in water, and (c and d) Measuring the immersed weight or RCMU.

The effect of the rubber replacement on the oven dry density of RCMUs is illustrated in Figure 2.18. As shown in the figure, the CMU's oven dry density decreased nonlinearly as the rubber content increased. Increasing the rubber content from 0 to 5% increased the oven dry density slightly from 2167 kg/m^3 to 2172 kg/m^3. The reason behind this increase was presented in the packing density results, where RCMU with 5% rubber gave the highest packing density of the dry raw materials compared to RCMUs with other rubber ratios as well as the reference conventional CMU. However, increasing the rubber ratio from 5% to 15% decreased the oven dry density from 2172 kg/m^3 to 2077 kg/m^3, representing a reduction of 4.4% in the RCMU's density. This reduction occurred because of the low packing density of the dry raw materials and the fact that the rubber particle's specific gravity was only 32% of that of the fine aggregate. Furthermore, the air content increased with an increase in the rubber content in the mixture as indicated by the higher absorption rate (Table 2.3).

As illustrated in Table 2.3 and Figure 2.17, RCMUs having up to 15% replacement of fine aggregate with crumb rubber have unit weights exceeding 2000 kg/m^3 and hence are classified as normal weight blocks.

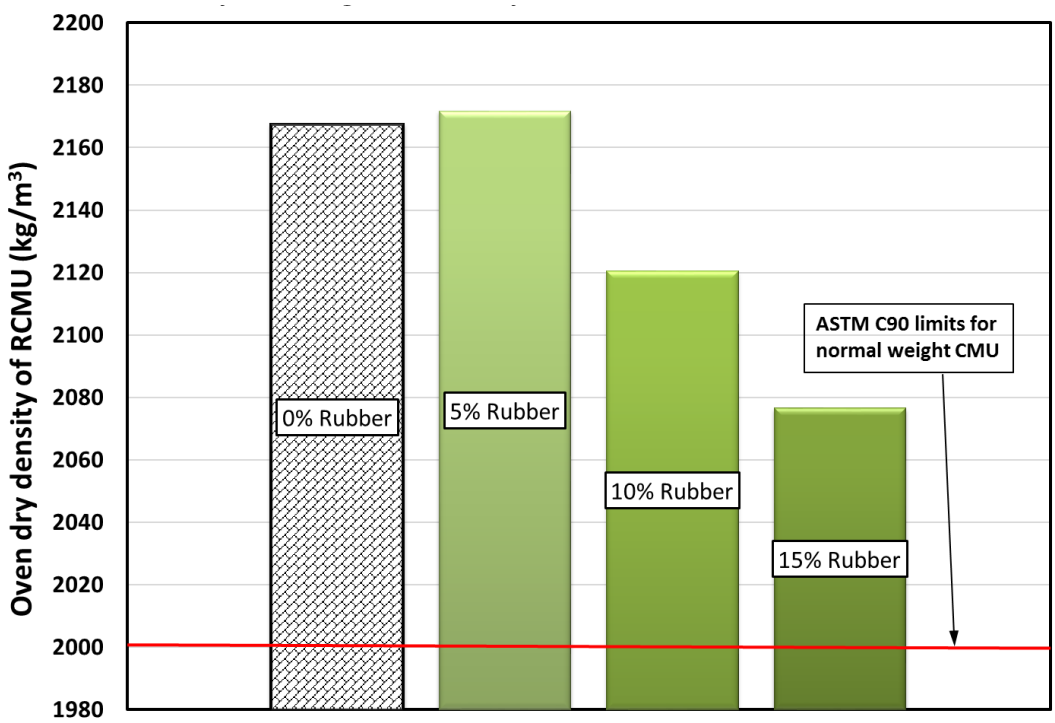

Figure 2.18: Effect of rubber replacement ratios on the oven dry density of RCMU.

The effect of rubber content on the water absorption is illustrated in Figure 2.19. The absorption rate of all RCMUs did not exceed the absorption limit of 208 kg/m^3 allowed by ASTM C90-12 (Table 2.3). Therefore, all RCMUs passed the water absorption limitations of ASTM C90-12. As shown in Figure 2.19, the water absorption decreased when the rubber ratio increased from 0% to 5% due to the increase in the packing density that was reported before in Figure 2.9a. However, the water absorption increased as the rubber content increased above 5%. Increasing the rubber content from 5% to 15% increased the water absorption from 107 kg/m^3 to 125 kg/m^3, representing an increase of 16.8%. The increase in the absorption rate occurred because the rubber had a relatively larger particle size than the fine aggregate. This difference in the particle size, shape and arrangement created extra voids due to the shortage of fine material in the rubber particles. Moreover, it is related to the increase in the air voids associated with low packing density, as explained earlier in this report.

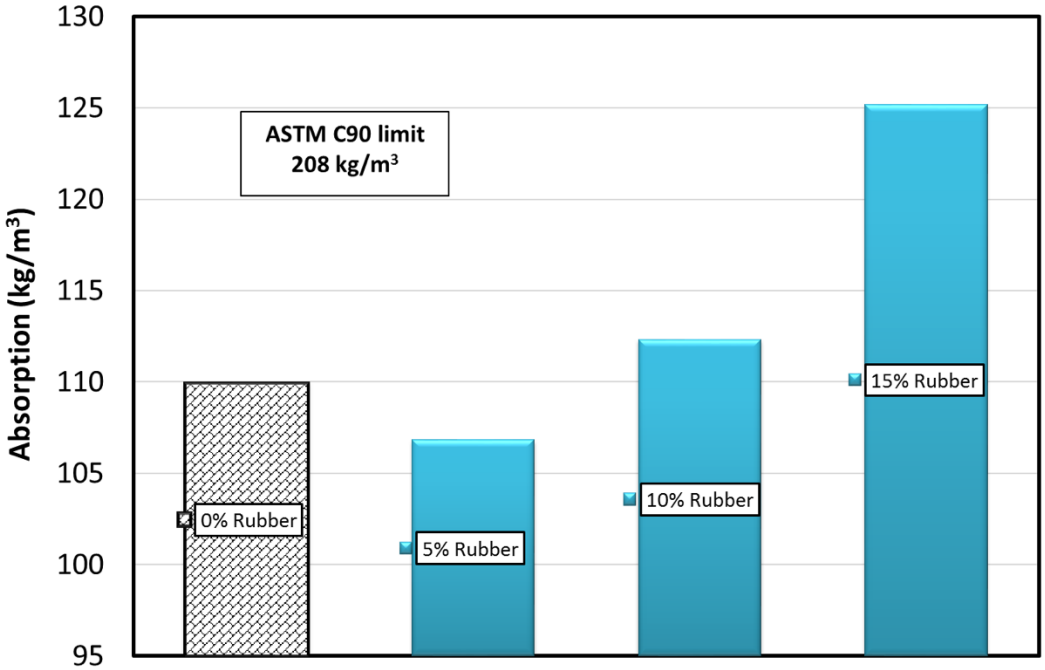

Figure 2.19: Effect of rubber replacement ratios on the water absorption of RCMU.

Three individual RCMUs from each rubber ratio were tested for their compressive strength. A fibrous composite laminated cap was used to distribute the load and prevent the stress concentrations (Figure 2.14). A rigid 610 x 305 x 51 mm steel loading plate was used to apply the loads (Figure 2.14). The maximum stress was averaged for each rubber ratio.

The effect of the rubber ratio on the compressive strength of RCMU is shown in Figure 2.20. As shown in this figure, increasing the rubber content from 0% to 5% increased the compressive strength slightly from 24.2 to 25.0 MPa due to the previously reported increase in the packing density with the addition of 5% crumb rubber. However, increasing the rubber replacement ratio from 5% to 15% decreased the compressive strength nonlinearly by 46%. However, increasing rubber replacement from 10% to 15% decreased the compressive strength by 15% only. Despite this decrease in strength, the compressive strengths of all the investigated RCMUs exceeded the minimum required strength of ASTM C90-12 of 13.1 MPa required for structural applications of load bearing masonry (Table 2.3).

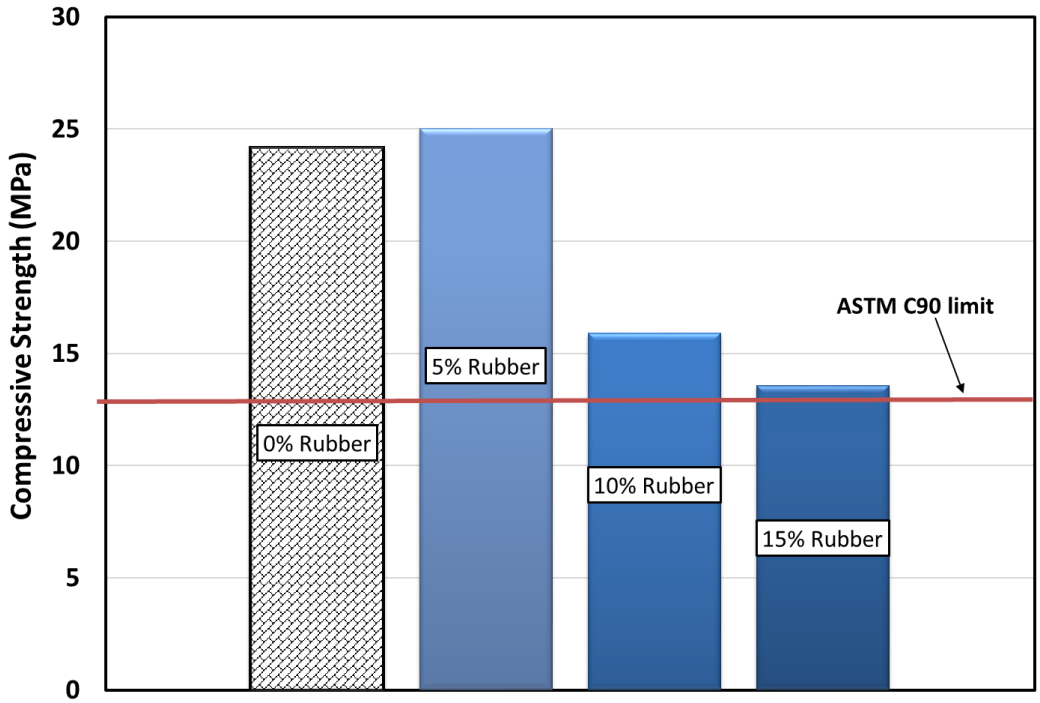

Figure 2.20: Effect of rubber replacement ratios on the compressive strength of RCMU.

Table 2.3. Material properties

Test type	Results	ASTM limits
Compressive strength ASTM C90−12	0% rubber 24.2 MPa 5% rubber 25.0 MPa 10% rubber 15.9 MPa 15% rubber 13.6 MPa	13.1 MPa (Min)
Absorption testing ASTM C90−12	0% rubber 110 kg/m^3 5% rubber 107 kg/m^3 10% rubber 112 kg/m^3 15% rubber 125 kg/m^3	208 kg/m^3 (Max)
Density classification ASTM C90−12	0% rubber 2167 kg/m^3 5% rubber 2172 kg/m^3 10% rubber 2120 kg/m^3 15% rubber 2077 kg/m^3	Lightweight less than 1680 kg/m^3 Medium weight ^{3} 1680–2000 kg/m^3 Normal weight 2000 kg/m^3 or more

3. Durability of Rubberized Concrete Masonry Units

3.1. Characterize the resistance of RCMUs to severe weather and cycles of freeze and thaw.

This chapter investigates the impact of utilizing recycled rubber particles within masonry matrixes on the overall durability. The first section covers the impact of incorporating varied crumb rubber rations on the resistance of RCMUs to rapid freezing and thawing according to ASTM C666/C666M-15. In addition to that, in the first section, the freeze-thaw durability of dry-cast segmental RCMUs was evaluated according to ASTM C1262/C1262M-18.

The second section of this chapter covers the impact of utilizing rubber-fiber powder (RFP), which is by-products of tire recycling, as an additive, on the durability of concrete products, in terms of the ability to protect steel reinforcement from corrosion.

3.2. Durability properties of cement mortar with recycled rubber

This part of the study used by-products of tire recycling as a sustainable alternative to produce rubberized mortar. The fresh properties, including workability and fresh mortar density, of rubberized mortar with different rubber fiber powder RFP ratios were investigated. In addition to the heat of hydration, the mechanical characterization of the rubberized mortar including hardened density, water absorption, compressive strength, flexural strength, and tensile strength were tested. Finally, the bulk and surface electric resistivity, rapid chloride ion penetration (RCIP), and the depth of carbonation were investigated to evaluate the durability of the new rubberized mortar mixtures. Figure 3.1 illustrates a schematic overview of this section.

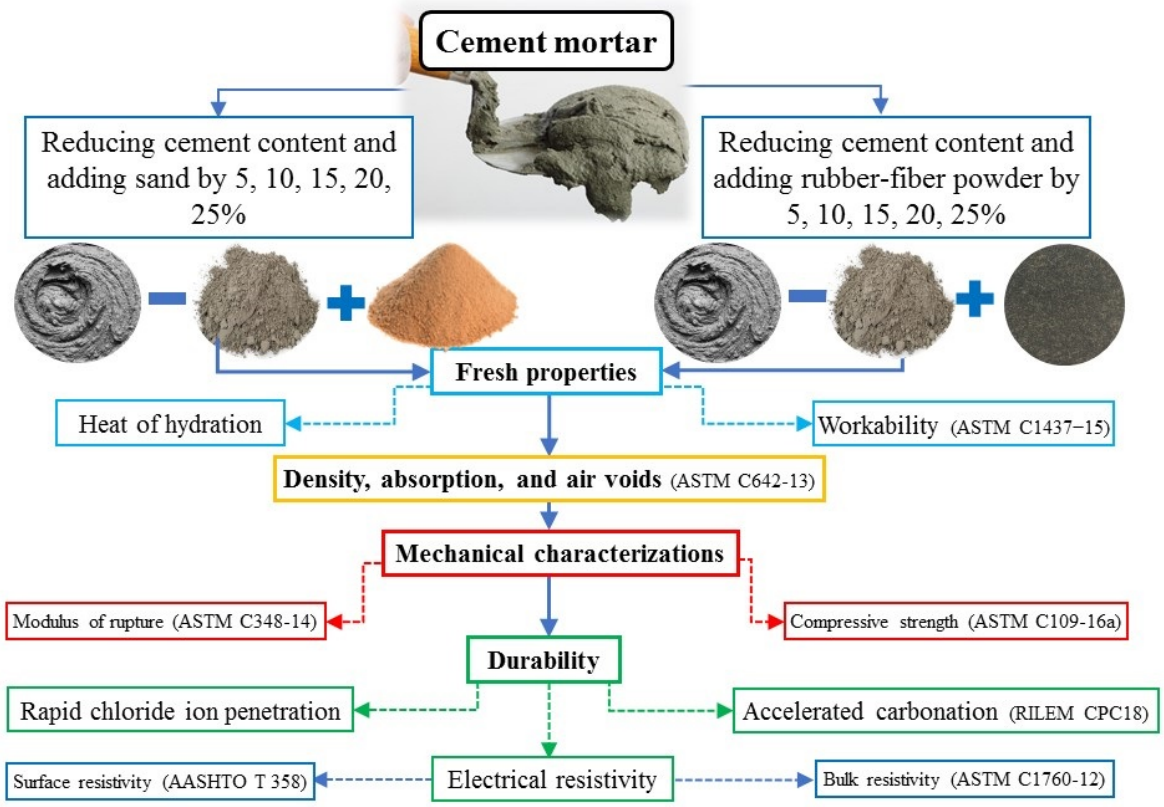

Figure 3.1: Schematic overview of the work done in this study.

3.2.1. Material Properties

Well-graded (Figure 3.2a) locally available river sand that meets the grain size distribution of ASTM C33 was used in this study. The waste RFP was obtained from a scrap tire processing factory in Macon, Missouri, USA. The RFP was sieved through a #200 sieve to remove any oversized particles. The particle size distribution of RFP and cement was determined using a laser diffraction analyzer (Figure 3.2b). Although both the RFP and cement passed #200 sieve (Figure 3.2b), about 25% and 9% of the RFP and cement particles respectively are still shown as having a size larger than #200 sieve since laser diffraction analyzer considers the larger dimension for each particle. For example, fibers or flaky particles with a length larger than 75 µm can pass #200 sieve but it is still considered larger than #200 sieve in laser diffraction analysis. The densities of RFP,

cement, and sand were measured (Table 3.1) per ASTM B923−16 using Ultrapyc 1200e density analysis by the ultimate gas pycnometers.

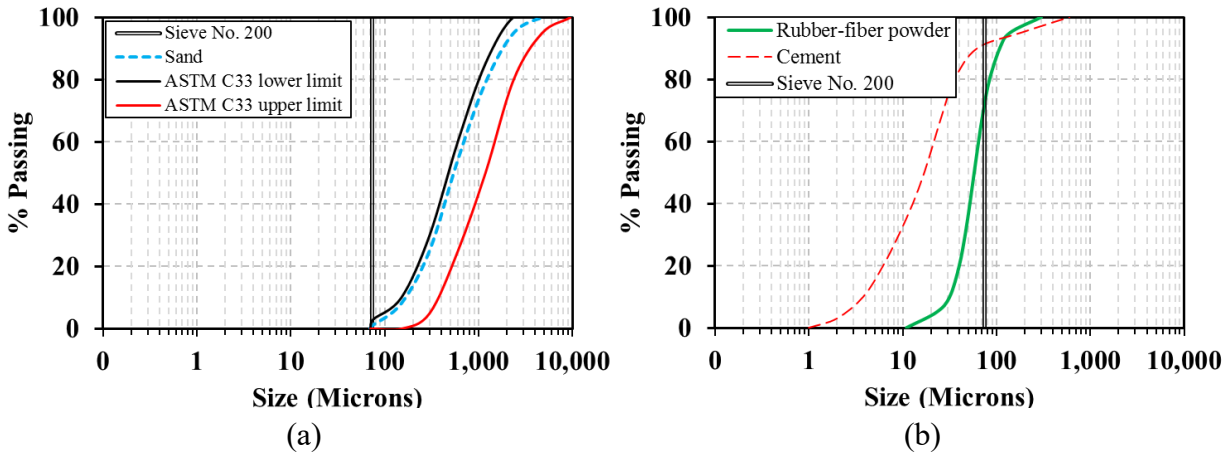

Figure 3.2: Particles size distribution analysis (a) Sieve analysis of sand, and (b) Laser diffraction analysis of RFP and Cement.

Table 3.1. Density results of the materials (ASTM B923−16).

Materials	Density (g/cm^3)
Rubber powder and nylon fiber (RFP)	1.566
Cement	3.132
Fine aggregate	2.648

A 3D digital microscope KH-8700 was used to investigate the RFP particles' shape, and the results showed the existence of nylon fibers as well as the irregular non-spherical shape of rubber particles (Figure 3.3). The x-ray photoelectron spectroscopy (XPS), which is a surface-sensitive quantitative spectroscopic technique that measures the elemental composition, was used to measure the percentage of rubber vs. nylon fiber in RFP and it was found that the RFP consisted of 76% rubber and 24% nylon fiber by volume.

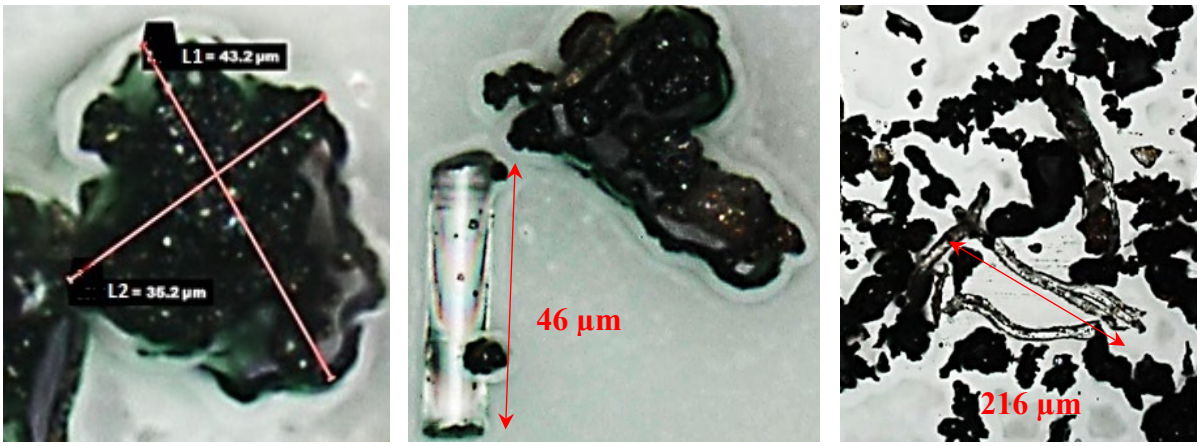

(a) (b) (c)

Figure 3.3: Microscopic images of rubber powder: (a, b) The angular irregular shape of the rubber particles and, and (c): Nylon fiber pieces within the powder.

3.2.2. Experimental work

This study investigated 39 mixtures (Table 3.2) that were grouped into four groups. Three different groups each had 11 mixtures and having water-to-cement ratios (w/c) of either 0.42, 0.51, or 0.56. The minimum used W/C ratio of 0.42 was selected based on optimization process such that the reference mortar mixture would display a minimum increase in the flow of 40±20% using the mini-slump per ASTM C230/ C230M.

In each group, one reference mixture without rubber and with a cement to sand ratio equal to 1:3 by weight was prepared. Each group also included another ten mixtures with either RPF or sand at five different volume ratios of 5, 10, 15, 20 and 25% while reducing the cement content at the same ratio. The fourth group had six mixtures with w/c ratio of 0.51. One reference mixture and five mixtures where RPF was used as a sand replacement at five different volume ratios of 5, 10, 15, 20, and 25%. This was a very comprehensive approach to decouple the effects decreasing the cement content and adding inactive material being sand or RFP; then, assess the effect of replacing sand with RFP.

Table 3.2: Test matrix.

Mix ID	Rubber addition (%)	Sand addition (%)	Rubber (kg)	Sand (kg)	Cement (kg)	Water (kg)	w/c	f'c (MPa)	MOR (MPa)
0-0.42	0	0	0.000	9.00	3.00	1.25	0.42	39.4	5.70
R5-0.42	5	0	0.075	9.00	2.85	1.19	0.42	33.5	5.30
R10-0.42	10	0	0.150	9.00	2.70	1.13	0.42	25.2	4.21
R15-0.42	15	0	0.225	9.00	2.55	1.06	0.42	21.7	3.52
R20-0.42	20	0	0.300	9.00	2.40	1.00	0.42	14.4	2.33
R25-0.42	25	0	0.375	9.00	2.25	0.94	0.42	7.40	0.62
S5-0.42	0	5	0.000	9.13	2.85	1.19	0.42	35.5	5.42
S10-0.42	0	10	0.000	9.25	2.70	1.13	0.42	35.9	5.48
S15-0.42	0	15	0.000	9.38	2.55	1.06	0.42	28.2	4.66
S20-0.42	0	20	0.000	9.51	2.40	1.00	0.42	27.2	4.41
S25-0.42	0	25	0.000	9.63	2.25	0.94	0.42	12.2	1.92
0-0.51	0	0	0.000	9.00	3.00	1.53	0.51	44.5	5.84
R5-0.51	5	0	0.075	9.00	2.85	1.46	0.51	37.5	5.76
R10-0.51	10	0	0.150	9.00	2.70	1.38	0.51	32.4	5.30
R15-0.51	15	0	0.225	9.00	2.55	1.30	0.51	26.1	4.52
R20-0.51	20	0	0.300	9.00	2.40	1.23	0.51	25.2	4.08
R25-0.51	25	0	0.375	9.00	2.25	1.15	0.51	20.7	3.32
S5-0.51	0	5	0.000	9.13	2.85	1.46	0.51	12.8	1.77
S10-0.51	0	10	0.000	9.25	2.70	1.38	0.51	10.8	1.52
S15-0.51	0	15	0.000	9.38	2.55	1.30	0.51	8.00	0.80
S20-0.51	0	20	0.000	9.51	2.40	1.22	0.51	6.20	0.51
S25-0.51	0	25	0.000	9.63	2.25	1.15	0.51	6.90	0.46
0-0.56	0	0	0.000	9.00	3.00	1.67	0.56	32.0	5.25
R5-0.56	5	0	0.075	9.00	2.85	1.58	0.56	22.7	3.58
R10-0.56	10	0	0.150	9.00	2.70	1.50	0.56	20.9	3.49
R15-0.56	15	0	0.225	9.00	2.55	1.42	0.56	20.6	3.34
R20-0.56	20	0	0.300	9.00	2.40	1.33	0.56	21.1	3.23
R25-0.56	25	0	0.375	9.00	2.25	1.25	0.56	19.0	3.10
S5-0.56	0	5	0.000	9.13	2.85	1.58	0.56	10.0	1.12
S10-0.56	0	10	0.000	9.25	2.70	1.50	0.56	5.70	0.18
S15-0.56	0	15	0.000	9.38	2.55	1.42	0.56	6.21	0.28
S20-0.56	0	20	0.000	9.51	2.40	1.33	0.56	6.82	0.44
S25-0.56	0	25	0.000	9.63	2.25	1.25	0.56	7.23	0.34
0-0.51S	0	0	0.000	9.00	3.00	1.53	0.51	24.1	3.92
R5-0.51S	5	0	0.266	8.55	3.00	1.53	0.51	22.2	3.71
R10-0.51S	10	0	0.532	8.10	3.00	1.53	0.51	26.2	4.00
R15-0.51S	15	0	0.799	7.65	3.00	1.53	0.51	21.0	3.61
R20-0.51S	20	0	1.065	7.20	3.00	1.53	0.51	16.9	2.85
R25-0.51S	25	0	1.331	6.75	3.00	1.53	0.51	12.5	1.82

Note: Constant volume of 4357 cm^3 was used for each mixture

A brass conical mold with a height of 50 mm, the diameter of the top opening of 70 mm and diameter of the bottom opening of 100 mm was used to carry out the mini-slump test per ASTM

C1437−15 for each mixture right after mixing and 30 minutes later. The fresh density of each mortar mixture was measured using a standard cylinder having a volume of 400 ± 1 mL, packed with mortar, and consolidated by placing the molds on a micro-vibration table for 40 seconds. Using the measured weight of the infill mortar and knowing the volume of the cylinder, the density was calculated. The density, absorption, and voids in hardened mortar were tested according to ASTM C642−13. The heat of hydration was also monitored and recorded for each mixture according to both ASTM C1679-17 and ASTM C1702-17. All specimens were demolded at the age of one day and were then moist-cured under a relative humidity of 95 ± 5% and a temperature of 23.0 ± 2.0º C until the testing day. Finally, both of the compressive strength and modulus of rupture (MOR) were tested at the age of 28 days according to ASTM C109-16a and ASTM C348–14, respectively, and the results are listed in Table 3.2.

3.2.2.1. Density, absorption, and air voids in hardened mortar

Concrete cylinders, 100×200 mm, out of each mixture were used to measure the density and voids in hardened mortar according to ASTM C642-13 method which can be used to deduce concrete permeability attribute and it yields results similar to that of vacuum saturation method; however, the former approach is more versatile. The test procedure can be summarized as follows: the oven-dried masses of all specimens were determined followed by saturating them in water and determine their surface-dry masses after immersion for not less than 48 hrs. After boiling the specimens in water for 5 hours, the soaked, boiled, and surface-dried masses were determined. Finally, after suspending the specimens in water, the apparent masses in water after immersion and boiling were determined. Based on the results from this procedure, the following characteristics can be calculated:

Absorption after immersion, % = $[(B - A)/A] \times 100$ (3.1)

Absorption after immersion and boiling, % = $[(C - A)/A] \times 100$ (3.2)

Bulk density, dry = $[A/(C - D)].\rho = g_1$ (3.3)

Bulk density after immersion =$[B/(C - D)].\rho$ (3.4)

Bulk density after immersion and boiling = $[C/(C - D)].\rho$ (3.5)

Apparent density = $[A/(A - D)].\rho = g_2$ (3.6)

Volume of permeable pore space (voids), % = $(g_1 - g_2)/g_2 \times 100$ (3.7)

Where: A = mass of oven-dried sample in air, B = mass of surface-dry sample in air after immersion, C = mass of surface-dry sample in air after immersion and boiling, D = apparent mass of sample in water after immersion and boiling, g_1 = dry bulk density, g_2= apparent density, and ρ = density of water.

3.2.2.2. Heat of hydration

An eight-receptacles I-Cal 8000 isothermal portable calorimeter was used in this study to evaluate the heat of hydration behavior of the different mortar mixtures. Each of the eight receptacles has a thermistor at the bottom, and all these receptacles were fixed inside a well-insulated box. The heat of hydration was recorded during the first 65 hours after adding the water to the mixture. Isothermal calorimeters, as opposed to semi-adiabatic calorimeters, allow for testing at a controlled temperature and thus enabling excellent repeatability.

A thermal hydration curve for each mixture was plotted while the ambient temperature around the sample remained constant at 20º C. The temperature was set via software interface with a feedback loop to ensure optimal control, while precision sensors measure the heat of hydration generated by the reaction of cementitious binders in the mixture. Embedded reference cells eliminate the need for duplicate test samples.

3.2.2.3. Accelerated carbonation

Carbonation affects the durability and strength of concrete directly by reducing concrete's pH and increases its porosity. The carbonation action began at the surface and propagate with time until reaching to the steel reinforcement causing corrosion damage. As a result, measuring the depth of carbonation is a direct method to evaluate concrete's ability to protect the steel reinforcement with time.

After being cured in the moisture room for 28 days, three mortar cylinders with a diameter of 100 mm and height of 50 mm were prepared, out of each mortar mixture, for accelerated carbonation test according to RILEM CPC18. The perimeter of each cylinder was painted with protective epoxy resin to secure one-dimension diffusion of the carbon dioxide into the specimens through its two opposite faces. The rubberized cylinders were placed in the carbonation chamber under a condition of 23º C, 70% relative humidity, and a 20% carbon dioxide concentration for the duration of 8 weeks. Then, the test cylinders were removed from the carbonation chamber and subjected to a splitting tension test. The freshly split surface was then cleaned and sprayed with a phenolphthalein pH indicator. After applying the indicator, the noncarbonated part would display a purple-red color due to the reduction in the alkalinity while the carbonated part remained gray. The depth of the carbonated area was measured at three various locations along each specimen and averaged.

3.2.2.4. Electrical resistivity

Solid materials have a relatively higher resistivity than air voids and capillary pores; hence, the electrical resistivity can evaluate the quality of the microstructure and porosity of a solid material such as mortar, which indicates mortar's permeability class and durability. By reducing

the permeability, reinforced concrete's capacity to resist chloride ion attacks will be enhanced which leads to better durability.

After 28 days of moist curing, both bulk and surface electrical resistivity of two 100×200 mm mortar cylinders samples from each mixture were determined using a Proceq Resipod bulk and surface resistivity tester (Fig. 3.4) per ASTM C1760-12 (Fig. 3.4a), and AASHTO T 358 (AASHTO 2015), respectively. The Proceq Resipod resistivity meter uses the principle of the Wenner probe where four equally spaced, 38 mm spaced, co-linear electrodes put in contact with a mortar specimen where the outermost electrodes are subjected to oscillating current while the middle two electrodes read the voltage. The surface resistivity can be calculated using Eq. 3.8.

$$\rho = 2\pi a V / I, \tag{3.8}$$

where ρ = surface resistivity (kΩcm), a = electrode spacing (25 mm), V = potential difference (V), and I = applied electric current.

(a) (b)

Figure 3.4: Electrical resistivity: (a) Bulk, and (b) Surface.

3.2.2.5. Rapid chloride ion penetration (RCIP)

While the chloride ion penetration during the service life of concrete is a very slow process, ASTM International developed a rapid testing method (ASTM C1202-17) that can be used as an indication for chloride penetration based on the electrical charge passed (Table 3.3). However, the

values in Table 3.3 are for concrete not mortar which would have more paste compared to concrete. As a result, higher values are expected for mortar.

The test was conducted for each mixture using a 50 mm thick mortar disk test specimen, which was cut from a fully cured 100 mm diameter cement mortar cylinder. To assure a one-dimension flow of the chloride ions, the surface of the side of each test specimen was coated with a water-proof epoxy. The specimens then put in vacuum desiccator where both end uncoated faces of the mortar pieces were in contact with water. After that, the desiccator closed tightly before starting the vacuum pump to decrease the pressure to less than 50 mm Hg (6650 Pa) within a few minutes and continued for 3 hrs (Fig. 5). The specimens then were placed in the test cells to be tested for chloride ion penetration with 3% NaCl solution on one side and 0.3 N NaOH solution on the other side.

Table 3.3: RCIP in concrete based on charge passed (ASTM C1202-17).

Charge Passed (coulombs)	Chloride Ion Penetrability
>4,000	High
2,000–4,000	Moderate
1,000–2,000	Low
100–1,000	Very Low
<100	Negligible

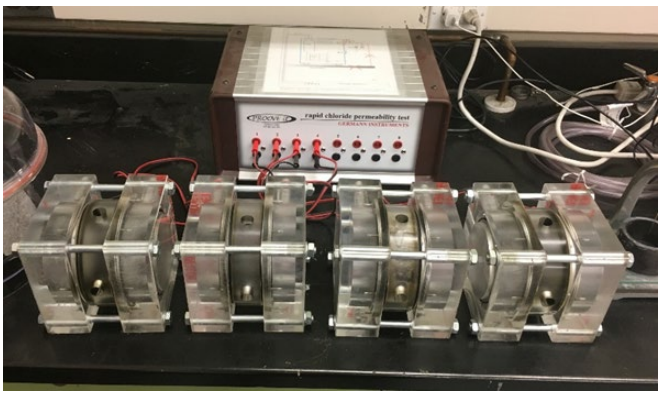

(a)

(b)

Figure 3.5: (a) RICP test device with 4 cells and (b) Vacuum desiccator.

3.2.3. Results and discussion

3.2.3.1. Fresh properties

Reducing the cement content, and adding either the sand or RFP, decreased the mixture workability almost linearly (Figure 3.6) which was associated with the reduction in water content to keep w/c constant. It is worth noting that the decrease in the workability was slightly higher in the case of introducing the RFP compared to introducing more sand. Mixtures having low w/c ratio of 0.42 was very dry reaching zero flow by 15% reduction in cement content and there was a significant fluctuation in the results of the table flow, with some mixtures displaying flow table results higher than that in the reference mixture only because of a collapse in the slump cone due to the lack of fine binding materials. Based on these results, mixtures with 0.42 were not used for further tests or investigations.

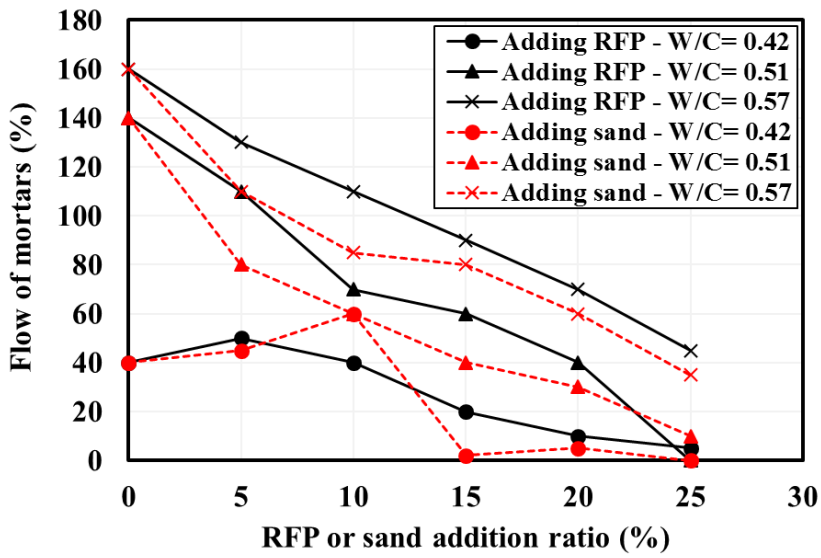

Figure 3.6: Workability of different mortar mixtures.

All the investigated mixtures had a cement to sand (or sand and RFP) ratio of at most 1:3, to ensure that the same behavior would be observed in higher-cement content mixtures, an extra set of mixtures were prepared with a cement to sand ratio of 1:2, W/C ratio of 0.51, and different reductions in cement and additions of RFP as was done in the other sets. The performance of this set was similar to the corresponding set but with cement to sand ratio of 1:3 (Figure 3.7), The only slight difference was that adding sand or RFP had the same effect on flowability. This occurred since, for higher cementitious content, the effect of reducing cement and hence water was more dominant than in the other case. Therefore, it can be concluded that the reduction in the workability is due to the reduction of water within the mortar matrix, not due to the introduction of RFP. The influence of RFP on workability will thus only play a role when the paste volume is sufficiently low.

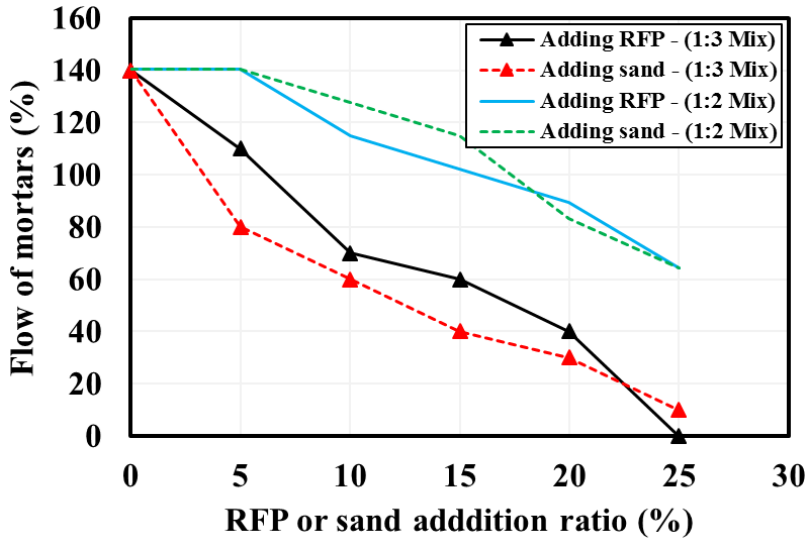

Figure 3.7: Workability of 1:2 and 1:3 mortar mixtures.

3.2.3.2. Density, absorption, and air voids in hardened mortar

Figure 3.8 shows the influence of using varied RFP, and sand ratios on each of the different types of densities. Adding RFP up to 15%, decreased the bulk densities of mixtures with w/c of 0.51 and 0.56. Replacing sand with RFP up to 5% also decreased the apparent density. Beyond these RFP content values, the bulk densities slightly increased then decreased again. Although it was anticipated to have a lower bulk density in the case of increasing the RFP content due to the relatively low density of RFP compared to sand or cement, adding RFP beyond a certain amount changed the mortar packing density as the present of RFP caused a decrease in the volume of permeable voids (Figure 3.9) leading to a more condense mixtures. However, there was no consistent trend since the workability is decreasing with both adding the RFP or sand to the mortar matrix side by side with reducing cement content. The lack of workability caused less compaction and higher air voids.

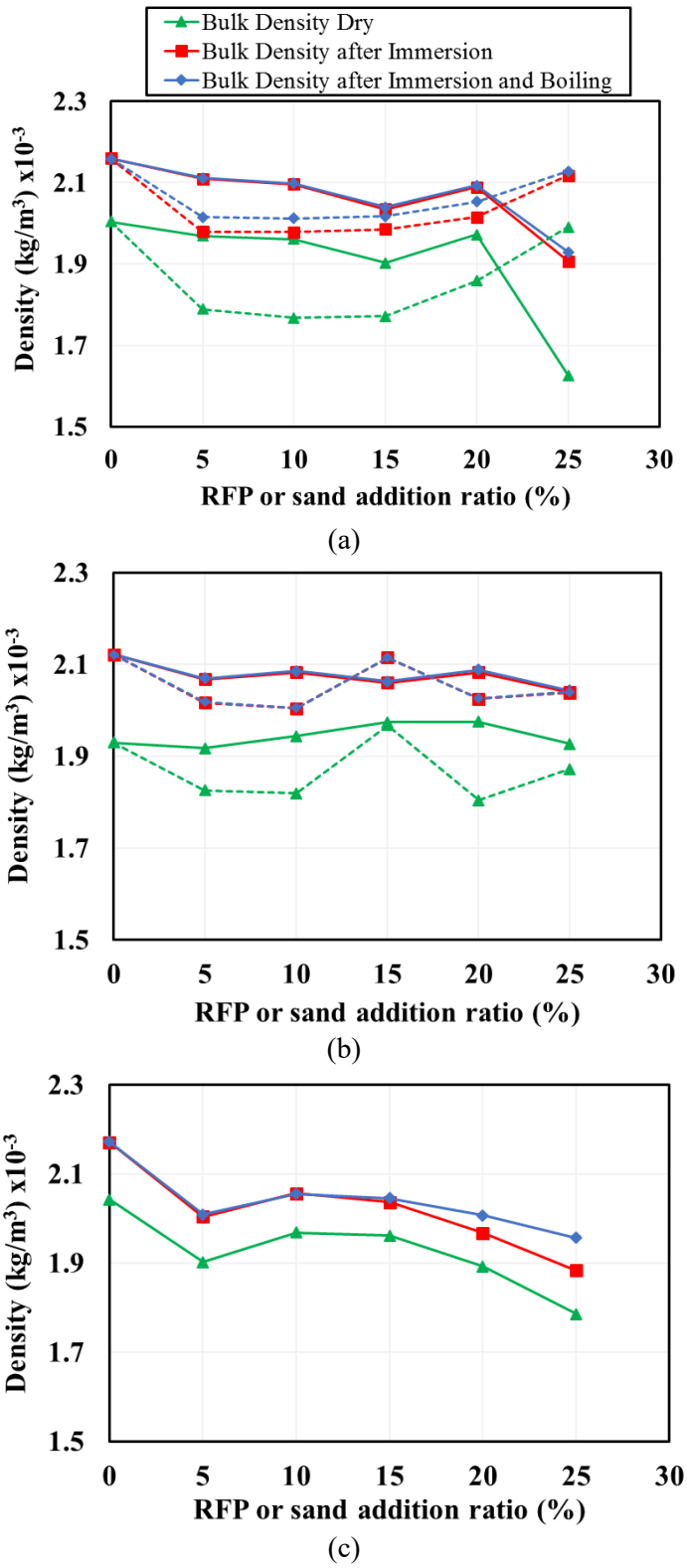

Figure 3.8: Different densities of mortar with: (a) W/C= 0.51, (b) W/C= 0.56, and (c) RFP was used as a sand replacement.

Dotted lines: adding sand; solid lines: adding RFP.

Optimizing the maximum particle packing density is another factor that affects the density. To optimize the particle packing density of mortar, the particles should be selected to fill up the voids between large particles with smaller particles and so on, to obtain a dense and stiff particle structure. A higher degree of particle packing leads to minimum voids, maximum density and requirement of cement and water will be less. However, optimizing the particle packing density require neutralizing the influence of the lack of compaction due to the lack of workability. As a result, mixtures with w/c ratio of 0.56, which resulted in the highest and the consistent workability (Figure 3.6), was used to evaluate the particle packing density. Taking the bulk density after immersion and boiling as an example since the immersion and boiling fill more air voids compared to the other densities. For example, the bulk density after immersion and boiling at RFP dosage of 20% decreased by 1.6% only (Figure 3.8b), while mathematically the density should be decreased by 4.3% due the low density of RFP compared to the other component. The difference between the actual density deduction (1.6%) and the mathematical density reduction (4.3%) refer to a change in the particles arrangement that leads to denser matrix.

This conclusion was consistent with the result of the permeable pore space (voids) in Figure 3.9b where the permeable air voids decreased with the increase of RFP dosage to 20%. Same consistency of results was noticed between the density and air void results. Mixture with w/c ratio of 0.51 has the highest volume of permeable voids at 25% RFP (Figure 3.9a) which caused the lowest density at the same ratio (Figure 3.8a). Same trend was noticed when the sand was added. Adding 15% sand resulted in the highest volume of permeable voids (Figure 3.9a) and lowest density (Figure 3.8a). When the RFP was used with reducing the sand instead of cement (Figure 3.8c and Figure 3.9c), RFP ratio of 15% resulted in the least volume of permeable voids.

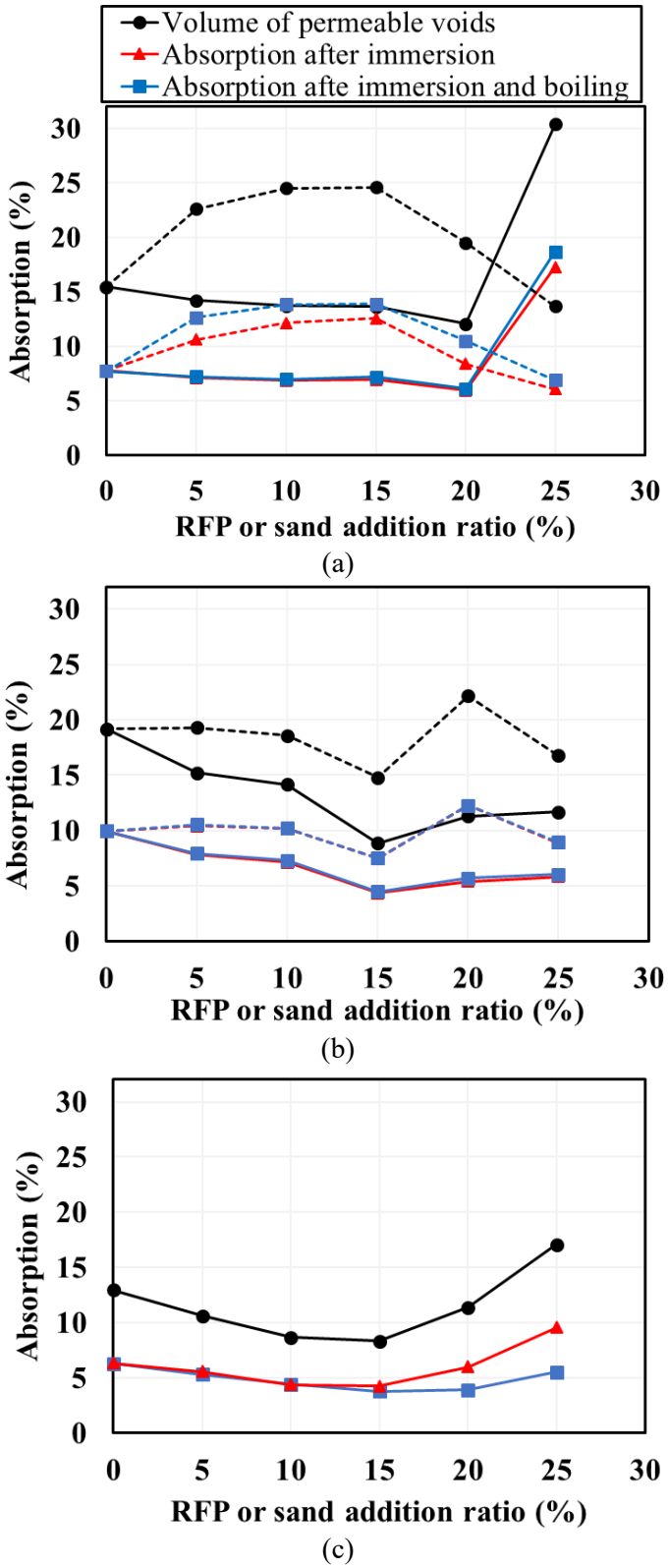

Figure 3.9: Absorption and air voids of cement mortar with: (a) W/C= 0.51, (b) W/C= 0.56, and (c) RFP was used as a sand replacement.

Dotted lines: addition of sand, Solid lines: addition of RFP.

3.2.3.3. Heat of hydration

Figure 3.10 shows the temporal variation of the heat of hydration per gram of cement over approximately three days for the different mortar mixtures. The higher the magnitude of the peak of temperature is the higher the rate of hydration of tricalcium silicate and paste hardening. In both cases, the w/c ratio was kept constant at 0.51 since we care only about the heat of hydration, not the workability.

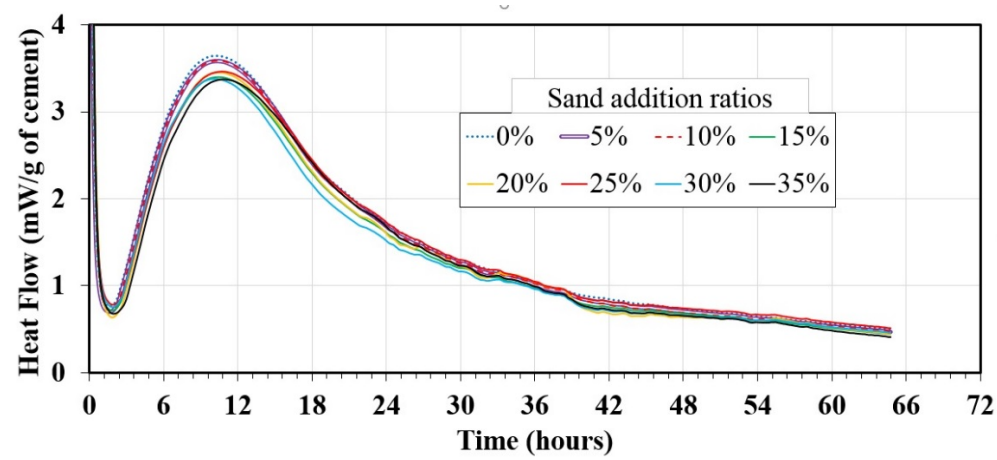

(a)

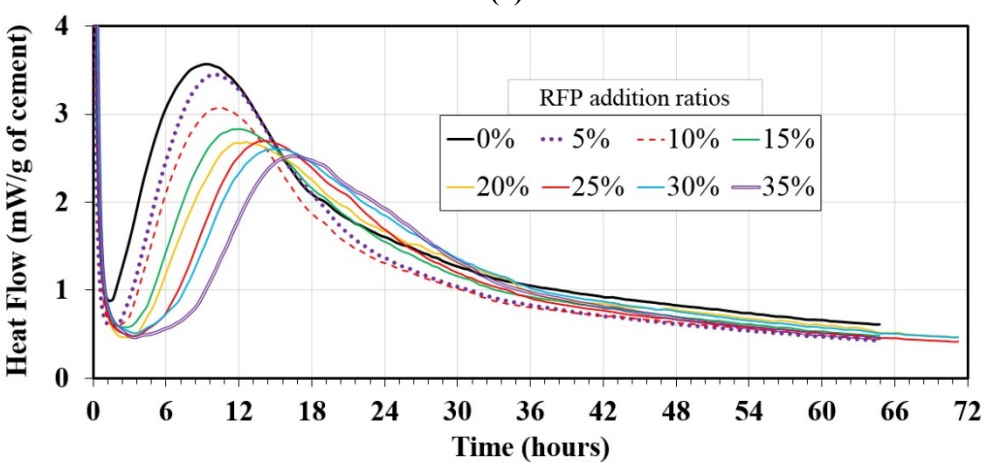

(b)

Figure 3.10: Heat of hydration (Calorimeter) curves of mortar mixtures with different: (a) sand addition, and (b) RFP addition ratios.

As shown in Figure 3.10a, adding extra sand to the mixture did not affect the normalized heat flow per gram of cement. However, adding RFP changed the temporal variation of the heat of hydration. This change due to the incorporation of the RFP which had a relatively high specific

heat of 2010 J/kg.K, the amount of heat per unit mass required to raise the temperature by one degree, compared to 840 J/kg.K for cement. As a result, mixtures with RFP needs more heat and time to reach a certain temperature compared to the reference mixture. This extra heat was obtained from the heat of cement hydration.

Figure 3.11 shows the magnitude of the peak heat flow and induction time for the different mixtures. The induction time, the period of inactivity just before the peak of hydration, is linked to the setting time which would increase with increasing RFP ratio. Adding RFP significantly decreased the heat of hydration and increased the induction time. For example, compared to the reference mixture, the magnitude of the peak heat flow of mixtures with w/c of 0.51 and with 15, 20, and 35% RFP ratios decreased by 20.7, 25.5, and 29.4%, respectively. However, the time of induction increased by 24.3, 31.5, and 78.5% for mixtures with 15, 20, and 35% RFP respectively. Adding extra sand did not have a significant effect on either the peak heat flow nor the time of induction.

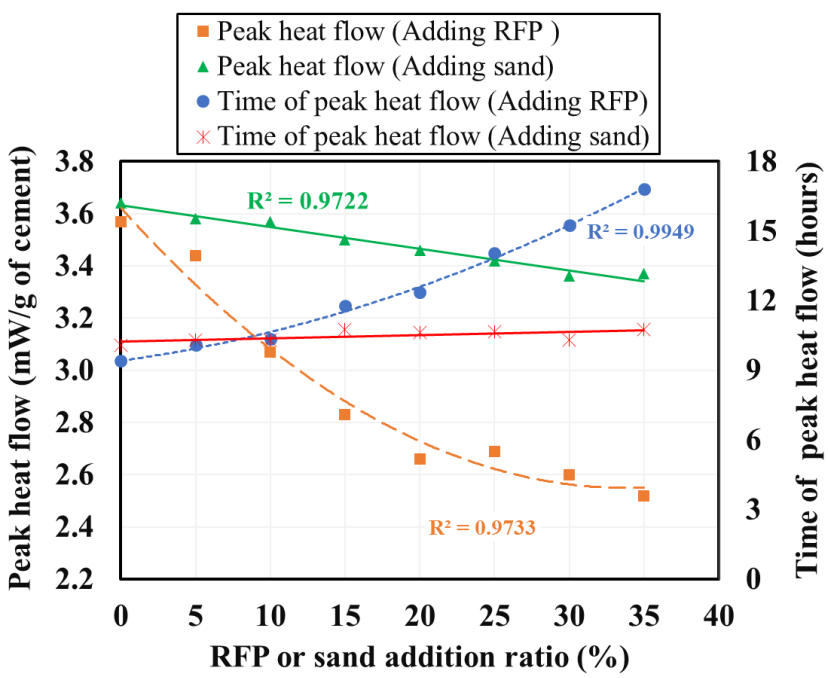

Figure 3.11: Magnitude of the peak heat flow and induction time of the different mortar mixtures.

The areas under the time – heat flow curves representing the heat of hydration divided by the mass of cement were calculated (Figure 3.12). The results indicate that increasing the RFP content lowers the peak heat flow of rubberized mortar.

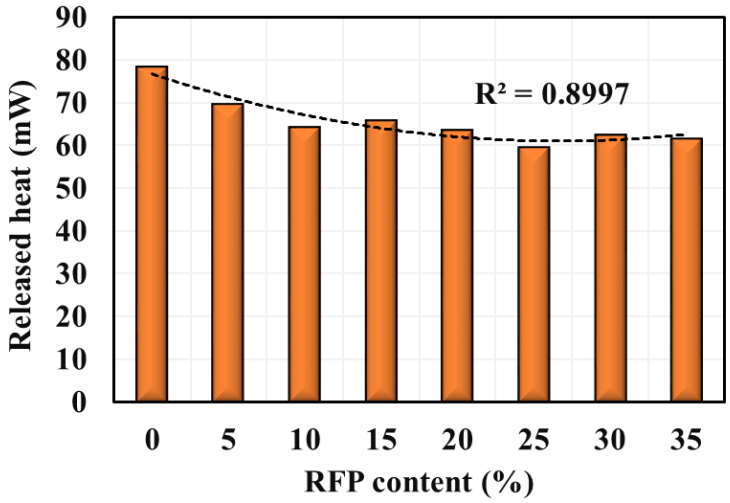

Figure 3.12: Heat of hydration released of the different mortar mixtures.

3.2.3.4. Electrical resistivity

Adding RFP to the mortar matrix influenced both the surface and bulk resistivity significantly compared to adding sand (Figures 3.13 and 3.14). For example, mixtures with w/c of 0.51, the surface and bulk resistivity the increased approximately linearly by 122% and 73% respectively with increasing the RFP content from 0% to 20%. However, increasing the RFP beyond 20% resulted in a decrease in the surface and the bulk resistivity by 51% and 48% for the surface and bulk resistivity, respectively (Figures 3.13a and 3.14a). This decrease can be explained by investigating Fig. 8a where increasing the RFP from 20% to 25% led to increasing the volume of the permeable pore voids from 12.1 to 30.4%. Similar behavior was observed for mixtures having w/c ratio of 0.56 with one-difference; both the surface and bulk resistivities increased significantly with increasing the RFP ratio up to 25% (Figures 3.13b and 3.14b). Investigating Figure 3.6 showed that adding 25% RFP for mixture having w/c of 0.56 did not deteriorate the workability

significantly, where at 25% of RFP or sand, the flow was around 40% compared to almost 0% with w/c ratios of 0.51 and 0.42 at the same addition ratio. Hence proper compaction process and high packing density were possible which led to decreased air void.

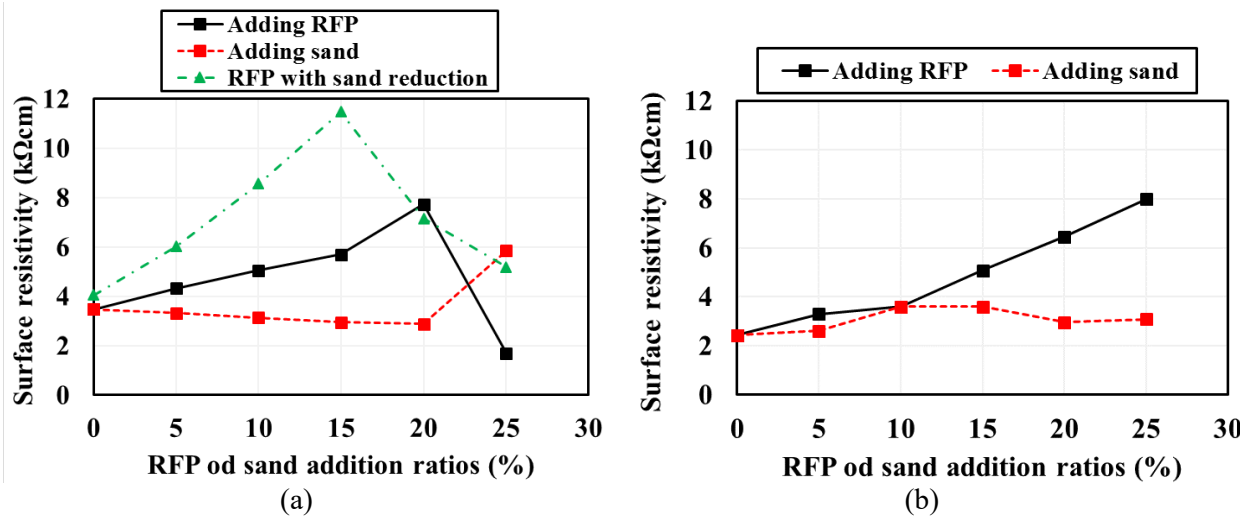

Figure 3.13: Surface electrical resistivity of mortar mixtures with: (a) W/C= 0.51, and (b) W/C= 0.56.

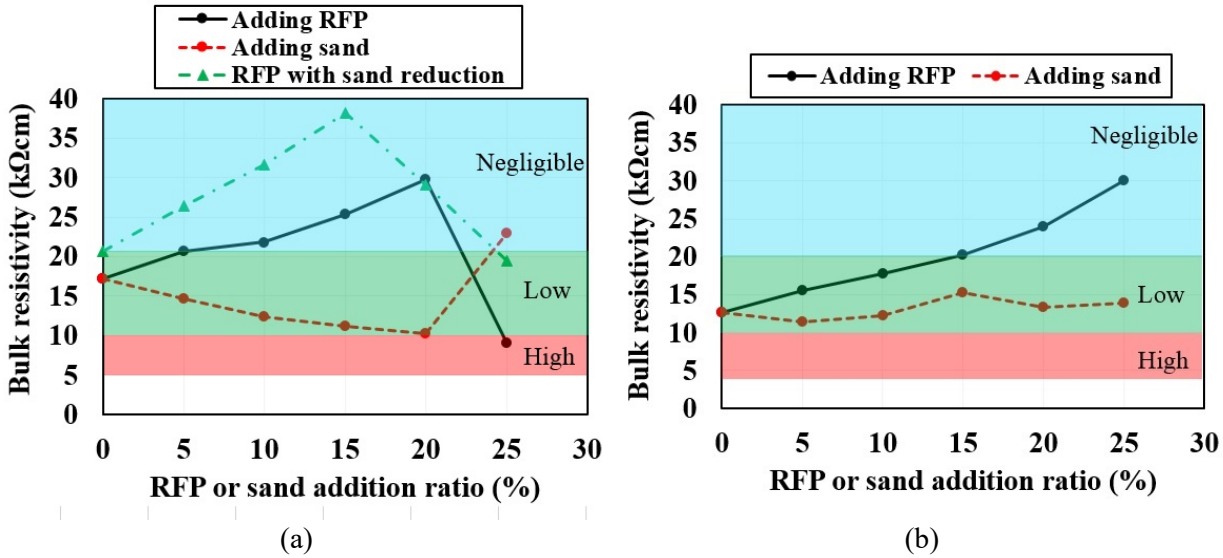

Figure 3.14: Bulk electrical resistivity of mortar mixtures and its correlation with steel corrosion risk with: (a) W/C= 0.51, (b) W/C= 0.56, and (c) RFP was used as a sand replacement.

Two main parameters, air voids between the sand particles and the porosity within the cement paste, affect the electrical resistivity of mortar mixtures. Air voids between the sand particles can be reduced through optimizing the size and gradation of the sand particles and/or incorporating materials with smaller particle size or different particle geometry and hence RFP with a particle size smaller than sand would be a potential candidate. Porosity within the cement paste can be reduced by reducing the cement content and used w/c in a mixture. Incorporating RFP into a mortar matrix added other contradicting parameters to the resistivity issue making it more challenging. The low electrical conductivity of rubber particles reduces the electrical resistivity of rubberized mortar mixtures (Kaewunruen and Meesit 2016, Si et al. 2018). However, adding rubber to concrete mixture increases its air content (Youssf et al. 2017) and decrease the workability (Figure 3.6) leading to reductions in concrete electrical resistivity. These contradicting parameters create a fluctuation and inconsistent behavior with different mixture parameters and RFP content.

To isolate the effect of reducing the cement from that of incorporating the RFP in the mortar mixtures on the resistivity, the resistivity values of mixtures included additional sand instead of RFP can be compared to those having RFP. For mixtures with sand addition having w/c of 0.51, the surface and the bulk resistivity decreased approximately linearly by 17% and 41% respectively with increasing the sand content from 0% to 20%. Beyond that and at 25% addition of sand, both the surface and bulk resistivity increased by 68% and 33% compared to the reference mixture, respectively. This increase occurred due to the decrease in the volume of the permeable voids with increasing the sand content (Figure 3.9a). For mixtures having w/c of 0.56, since the electrical current uses the interconnected void within the cement paste, reducing the cement only and using sand decreased the electrical resistivity slightly compared to the reference mixture. In addition, Figure 3.9b shows that at w/c ratio of 0.56, there is a general decreasing trend with increasing both RFP and sand content.

Replacing sand with the RFP without reducing the cement content yielded the highest electrical resistivity compared to the other mixtures with an optimum replacement ratio of 15% (Figure 3.13a and 3.14a). Beyond that, the electrical resistivity decreased but still higher or similar to the reference mixture in both the surface and the bulk resistivity respectively. With both w/c ratios of 0.51 and 0.56, adding RFP moved the risk of corrosion from low to negligible per (Chini et al. 2003, Song and Saraswathy 2007, Hornbostel et al. 2013, Sengul 2014, Azarsa and Gupta 2017) where specimens having a bulk resistivity of 20 kΩcm or more have a negligible corrosion risk.

3.2.3.5. Rapid chloride ion penetration (RCPT)

Adding RFP decreased the rapid chloride ion penetration (RCPT) up to 20% RFP (Figure 3.15). Beyond that the RCPT value significantly increased due to the increase in the volume of the permeable pore space from 12.06 to 30.40% (Figure 3.9a). A mixture having 20% RFP had an average RCPT of 2667 Coulombs passed through the specimens which represent 76% reduction in the charge passed compared to 10933 Coulombs passed through the reference specimen. Despite the reduction in the RCPT values and except for the mixture with 20% RFP, all mixtures were classified as a high RCPT per (Chini et al. 2003, Hornbostel et al. 2013, Sengul 2014). Adding sand with 5% or higher increased the RCPT values linearly. It is worth noting that the results of the RCPT had a strong correlation to both surface resistivity and bulk electrical resistivity. Eq. 9 was empirically developed to correlate the surface resistivity to the RCPT (Kessler et al. 2005). The experimental results in this study follow closely the relationship described in Eq. 3.9 (Figure 3.16).

$$Surface\ Resistivity = 5801.2(Rapid\ Chloride\ Permeability)^{-0.819} \quad (3.9)$$

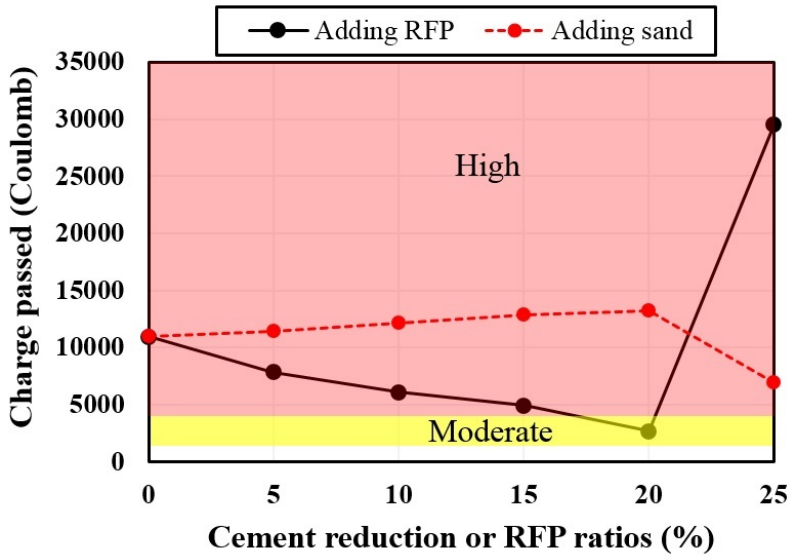

Figure 3.15: Charge passed through mixture with w/c ratio of 0.51 with adding RFP or sand and its correlation with the RCPT.

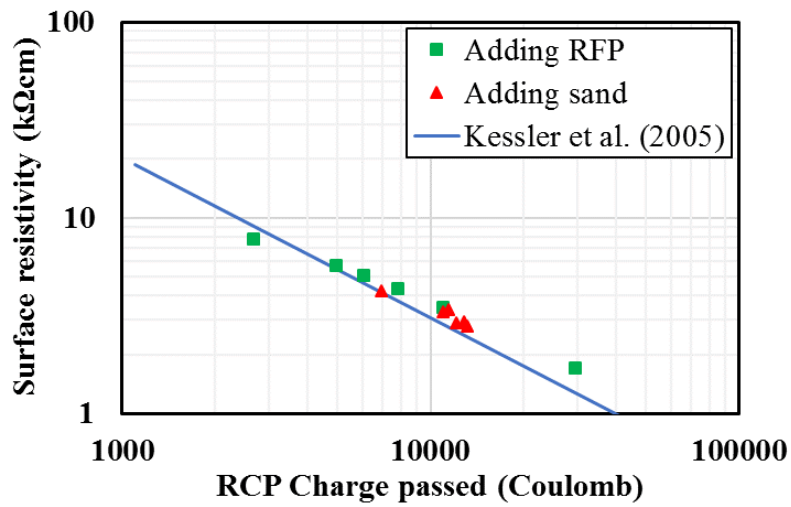

Figure 3.16: Surface resistivity versus rapid chloride permeability.

3.2.3.6. Accelerated carbonation

The effect of adding the RFP while reducing the cement content functions in w/c of the mixture (Figures 3.17 and 3.18). For w/c of 0.56, adding up to 25% RFP to the mixtures reduced the carbonation depth (Figure 3.17b). The carbonation depth started with 13 mm for mixture with 0% rubber content and decreased to approximately 8 mm for mixture with 10% rubber content and

then increased to 11 mm for mixture with 25% rubber content. Adding sand, however, significantly increased the carbonation depth. At 5% sand addition, the CO2 had a full penetration into the specimen. The carbonation rate is highly affected by the permeability of concrete that mainly caused by alternating the pore size and distribution (Kulakowski et al. (2009). Therefore, the air void content, particles arrangement, and accompanying air voids in a mixture directly affected the carbonation depth. For relatively low w/c of 0.51, adding RFP or sand increased the carbonation depth. However, this increase was very pronounced in the case of sand compared to RFP.

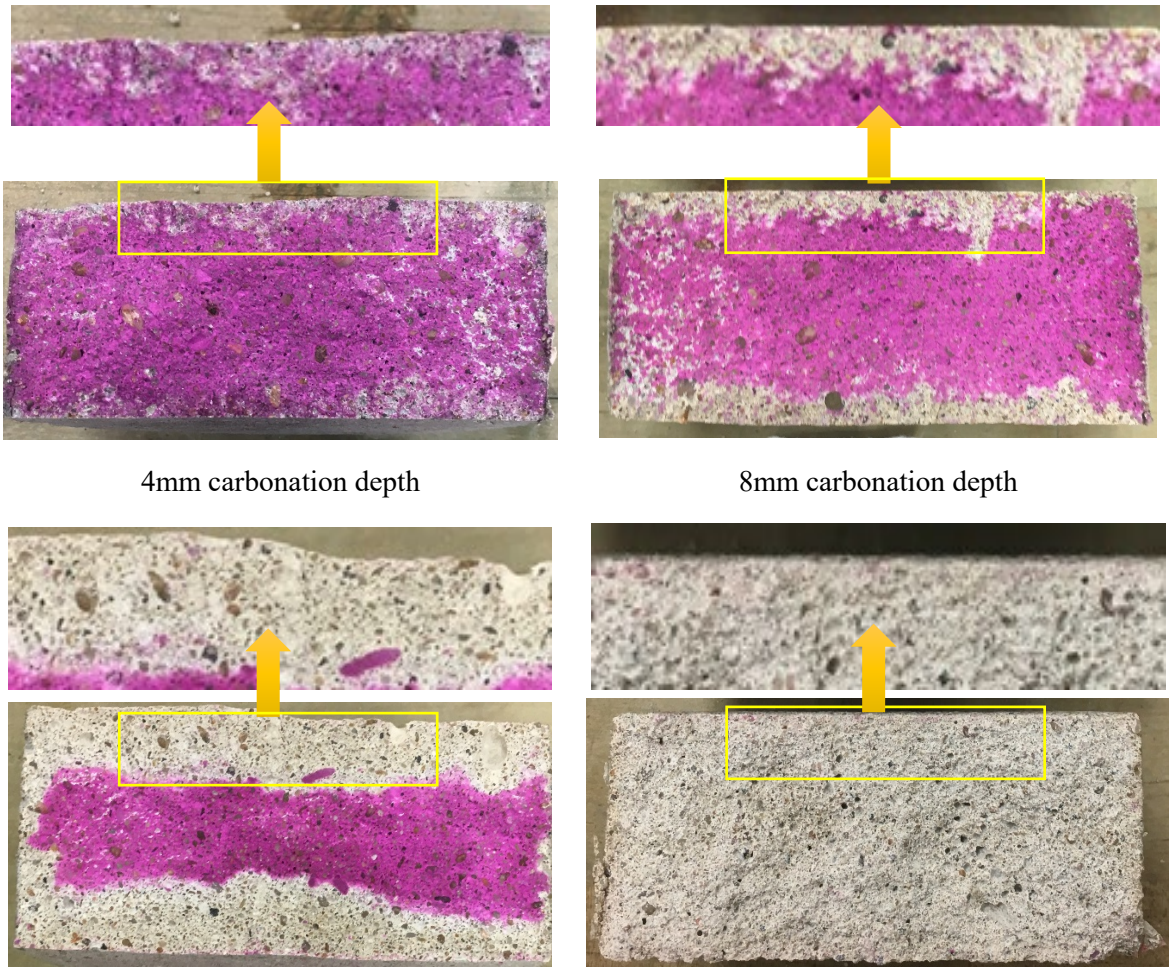

Figure 3.17: Different carbonation depths with different RFP or sand content.

Adding 5% or higher sand, the carbonation reached a full depth of the specimen. Adding RFP led to an approximately linear increase in the carbonation depth reaching 15 mm at 25% addition of RFP (Figure 3.18a). This behavior was due to the lack of compaction as a direct result of the relatively low workability of mixtures with w/c ratio of 0.51.

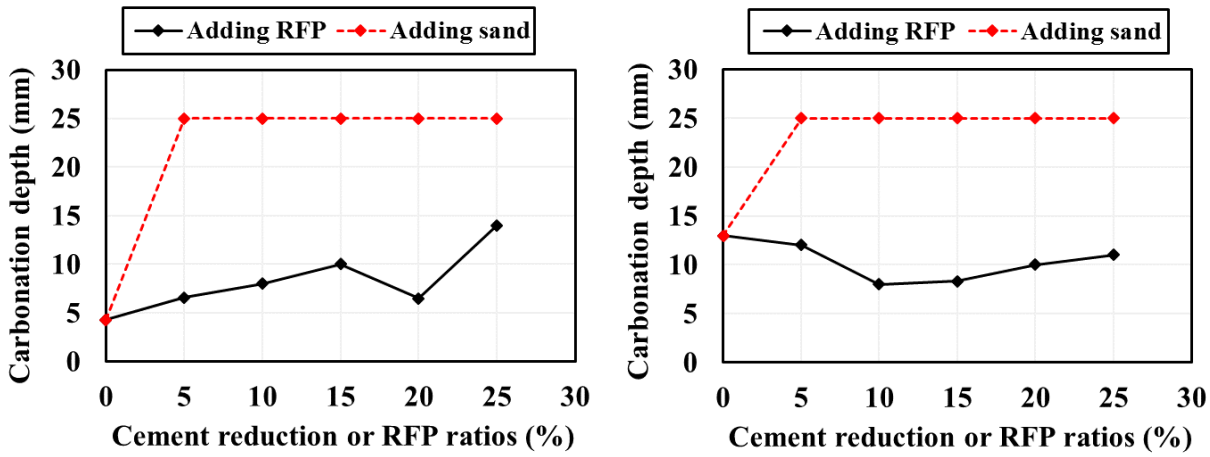

(a) (b)

Figure 3.18: Accelerated carbonation depth of mortar mixtures with: (a) W/C= 0.51, and (b) W/C= 0.56.

4. Mechanical Characterization of RCMU Prisms and Walls.

The first part of this chapter focuses on examining the mechanical characteristics of concrete masonry prisms constructed using RMCUs with four rubber ratios of 0%, 5%, 10%, and 15%, as explained in Chapter 2 of this report. The second part of this chapter reports the cyclic testing of a full-scale shear wall that has rubberized masonry units at its toes. The full-scale RCMU wall was compared with a reference conventional wall to highlight the advantages of incorporating RCMUs in masonry shear walls in terms of the cyclic and seismic performance.

4.1. Mechanical Characterization of RCMU Prisms

Twelve masonry prisms having heights of four blocks and crumb rubber replacement ratios of 0%, 5%, 10%, and 15%, were constructed and examined for their ultimate strength and strain. Three replicate prisms were tested for each rubber content, and the average values for each rubber content was calculated and reported in this chapter.

4.1.1. RCMU Prisms Preparation

Professional masons constructed the masonry prisms according to ASTM C1314–12 in a stack bond using fully bedding Portland cement lime mortar type S. Standard 200 mm CMUs and RCMUs produced as explained in Chapter 2 of this report were used to construct the prisms. Each prism was constructed to be one- block long and four- course blocks high. Grouting was completed immediately after the prisms were constructed. A rod vibrator was used to consolidate the grout in each cell immediately after the grout was poured into the prisms. The prisms were then cured in lab conditions until the day of testing.

Material samples were taken during the construction. Mortar cylinders measuring 100x50 mm and grout prisms measuring 100x100x200 mm were sampled according to ASTM C1019–11. The samples were tested on the same day when the prisms were tested and at 28 days to determine the mortar and grout compressive strengths.

4.1.2. Test Set-up, Loading, and Instrumentations

A displacement control compressive monotonic loading was used to test all specimens (Fig. 3). According to ACI 374.2R-13, the loading increment's magnitude should be small enough to capture the main features in the experiment. As a result, the test was run at a rate of 1.27 mm/min for each step.

Two linear variable displacement transducers (LVDTs) were used in each prism to measure the vertical displacement in the middle portion of the height. These displacements were used to calculate vertical strains within the masonry prisms (Figure 4.1).

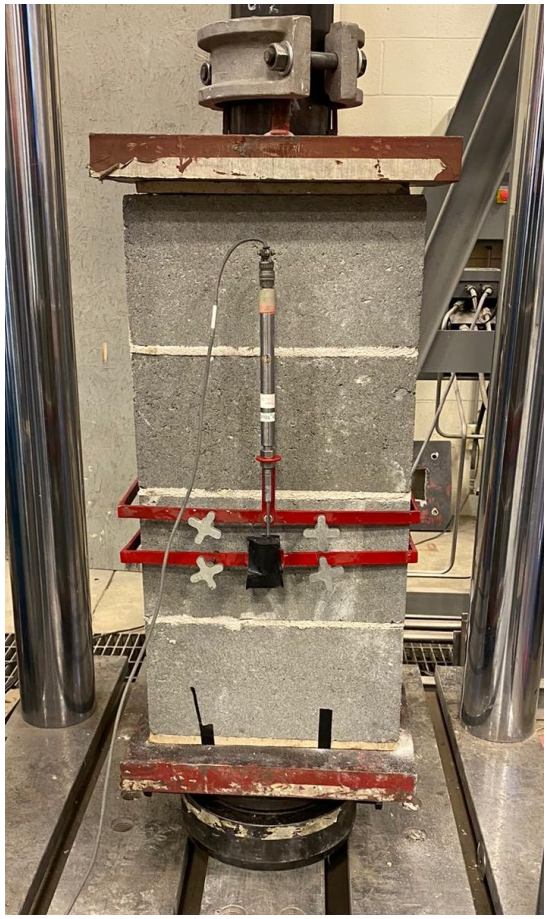

Figure 4.1: Vertical stress-strain test setup of four-block high prisms with the instrumentations.

4.1.3. Materials Properties

All the materials used in this research were sampled and tested according to the appropriate ASTM standard test methods. The results gathered during the materials property tests are listed in Table 4.1. The grout was sampled and tested according to ASTM C1019 – 13. The mortar was sampled and tested for compressive strength according to ASTM C270−12a.

Table 4.1: Material Properties

Items	Tests type	Results (MPa)	ASTM limits
Mortar	Compressive strength ASTM C109/C109M-13	20.7	Type S 12.4 MPa
Grout	Compressive strength ASTM C1019-13	30.4	14 MPa
RCMU	Compressive strength ASTM C140–14b	0% rubber 24.2 5% rubber 25.0 10% rubber 15.9 15% rubber 13.6	13.1 MPa
Masonry block prism	Compressive strength f'm ASTM C1314-12	see table 4.2	---------

4.1.4. Results and discussion

The results gathered from testing four-block high prisms using fibrous capping are listed in Table 4.2. These results indicate that the mechanical characterizations of masonry units were impacted significantly when crumb rubber was used as a partial sand replacement.

As shown in Table 4.2, the trend of the compressive strength matches the trend of the packing density results in Figure 2.9 where the highest dry density and strength for the RCMUS that were produced in both the Missouri S&T laboratory and Midwest Brick and Block production facility (Figures 2.15 and 2.20) were achieved with a 5% rubber ratio. The RCMU with 5% rubber content yielded the highest compressive strength compared with all investigated blocks including the reference CMUs. The compressive strength decreased in the case of 10% and 15% rubber ratios. Using rubber as a replacement for mineral sand in CMUs reduced the compressive strength and increased the ultimate strain. The effect of rubber on the descending branch of the stress-strain

curve prisms was more pronounced compared to the prism with conventional CMUs. Using RCUMs with 5% rubber content increased the compressive strength from 26.1 to 27.5 MPa. However, increasing the rubber content to 15% decreased the strength to 15.2 MPa which represents a reduction of 52% in the prism strength. However, RCMUs with 5%, 10%, and 15% were within the ASTM limits for loadbearing masonry units.

Table 4.2: Average Tests Results of Four Block Height Masonry Prisms

Specimen name	**maximum stress (MPa)**	**MicroStrain at maximum stress (mm/mm)**	**Initial Stiffness (GPa)**
0% Rubber	26.1	1300	20.07
5% Rubber	27.5	2300	11.96
10% Rubber	17.3	2860	11.01
15% Rubber	15.2	1540	10.02

In terms of the ultimate strain, increases in the peak strains of 77%, 120%, and 18% were recorded when rubber replacement ratios of 5%, 10%, and 15%, respectively, were used in the four-block high grouted prisms (Figure 4.2). It is worth noting that despite the relatively low compressive strength of the RCMUs prisms with rubber ratios of 10% and 15%, the peak strain (which was higher in the rubberized prisms) was achieved under relatively low stress, which is very advantageous; a high-energy dissipation can be achieved under low stress.

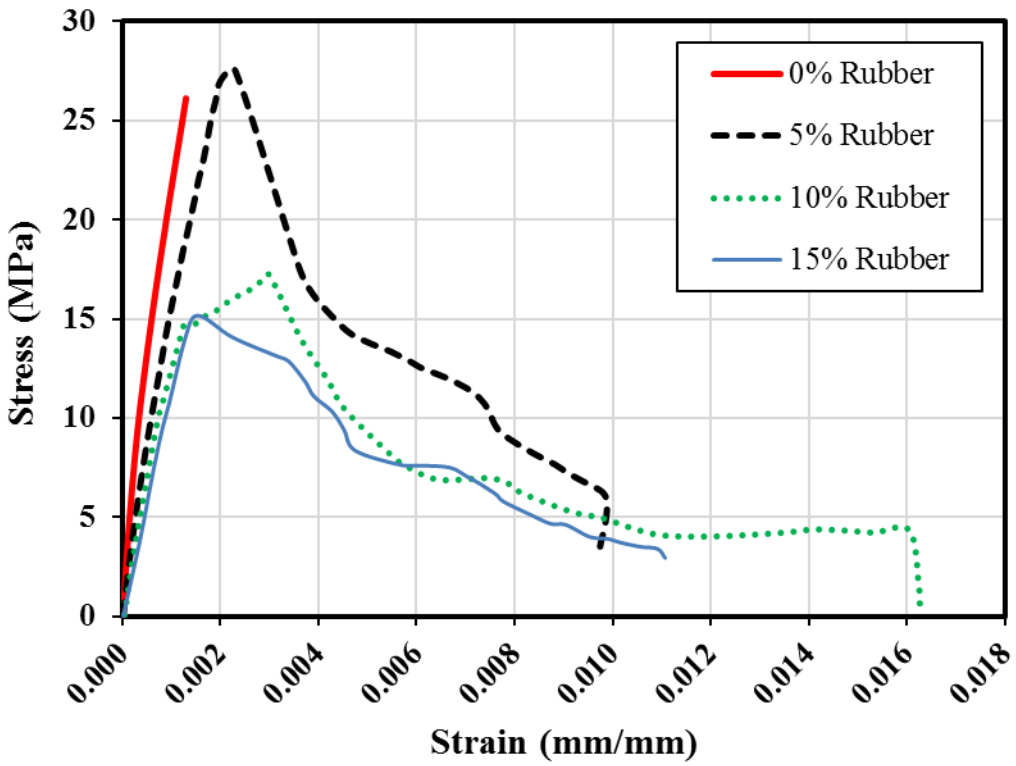

Figure 4.2: Stress vs. strain of grouted four blocks height masonry prisms.

The change in the strength in the case of grouted prisms was not proportional to the rubber content due to the presence of the grout. The strength of the grouted prisms results from two different components, namely, the block strength and grout. For a conventional CMUs, the block is quite brittle due to the severe stress concentrations which lead to very early failure of the CMUs' face-shells and webs before the filler grout was subjected to high axial stresses (Figure 4.3a). During testing of the CMUs prisms, the grout suffered a few micro to macro-cracks at the rupture of the prisms (Figure 4.3). Hence, the contribution of grout to prism strength was limited. Contrarily, RCMUs had the ability to go through higher axial deformation before failure, allowing higher grout deformations and higher grout contribution to the prism axial strength. However, the addition of rubber reduced the strength of the CMUs. For example, RCMUs having 15% rubber

replacement had the ability to go through very high axial strains without failure but the high rubber replacement ratio had a significant effect on the strength.

(a) (b)

Figure 4.3: Failure mechanism for four blocks height prisms with: (a) no rubber added, and (b) 5% rubber ratio.

The initial stiffness of the investigated prisms was calculated and presented in Table 4.2. The table shows the influence of crumb rubber content on the stiffness of the prisms. Increasing the rubber content from 0% to 15% decreased the stiffness from 20.07 GPa to 10.02 GPa, which represented a reduction of 50%.

Another beneficial feature was recorded for the RCMUs prisms regarding the failure mechanism. Failure in the conventional CMU prisms was quite brittle. In contrast, RCMU prisms were able to sustain displacement beyond the peak stress. For example, RCMUs having 15% rubber replacement ratio, exhibited gradual ductility and were able to resist displacement

corresponding to a strain of 121% of its peak strain at stress equal to 85% of the maximum stress (Figure 4.2). RCMU prisms reached their maximum stress under a relatively high strain because the rubberized block had the ability to deform until the high strength grout reached its maximum strain. In contrast, the conventional CMUs collapsed early due to face shell spalling while the grout displayed no or a few micro-cracks (Figure 4.3). This feature represents pseudo ductility for masonry, which allows engineers to do the required repair in the critical compression failure zones before the total collapse or failure can occur in the whole structural masonry element. However, this requires all other failure modes such as shear failure and reinforcement rupture be superseded. Finally, the large axial strains in RCMUs would help a structural masonry element to display higher ductility capacity, which is crucial for seismic regions.

4.2. Cyclic Behavior of Post-tensioned Rubberized Masonry Shear Wall

This section of the chapter deals with examining the performance of full-scale shear walls where RCMUs were utilized at the toes, which are the most critical zones within flexurally-dominant shear walls subjected to earthquake loads. The performance of a rubberized shear wall was compared to that of a conventional wall under cyclic lateral loading that can lead to a direct conclusion about their performances under earthquake loads.

4.2.1. Experimental Program

Two full-scale masonry shear walls were tested to investigate the effect of using rubberized masonry units (RCMUs) at their anticipated plastic hinge region. The RCMUs was used as a proposed alternative to conventional confining boundary elements used in masonry shear walls in high seismic regions to provide higher ultimate strain capacity. It is worth noting that providing confinement in masonry boundary elements is very challenging and hence is rarely used in practice despite its anticipated benefits. Therefore, should RCMUs be able to address this issue, that would be a unique solution for a significant problem.

The walls were 88 inches in high and 103.6 inches long. Both walls were constructed using 8-inch blocks. The rubberized walls were constructed using CMUs except at their toes as shown in Figure 4.4, where RCMUs were used. The reference wall (Figure 4.5) was built fully using conventional CMUs. Both walls were unbonded post-tensioned masonry walls with special construction and loading details discussed in later sections.

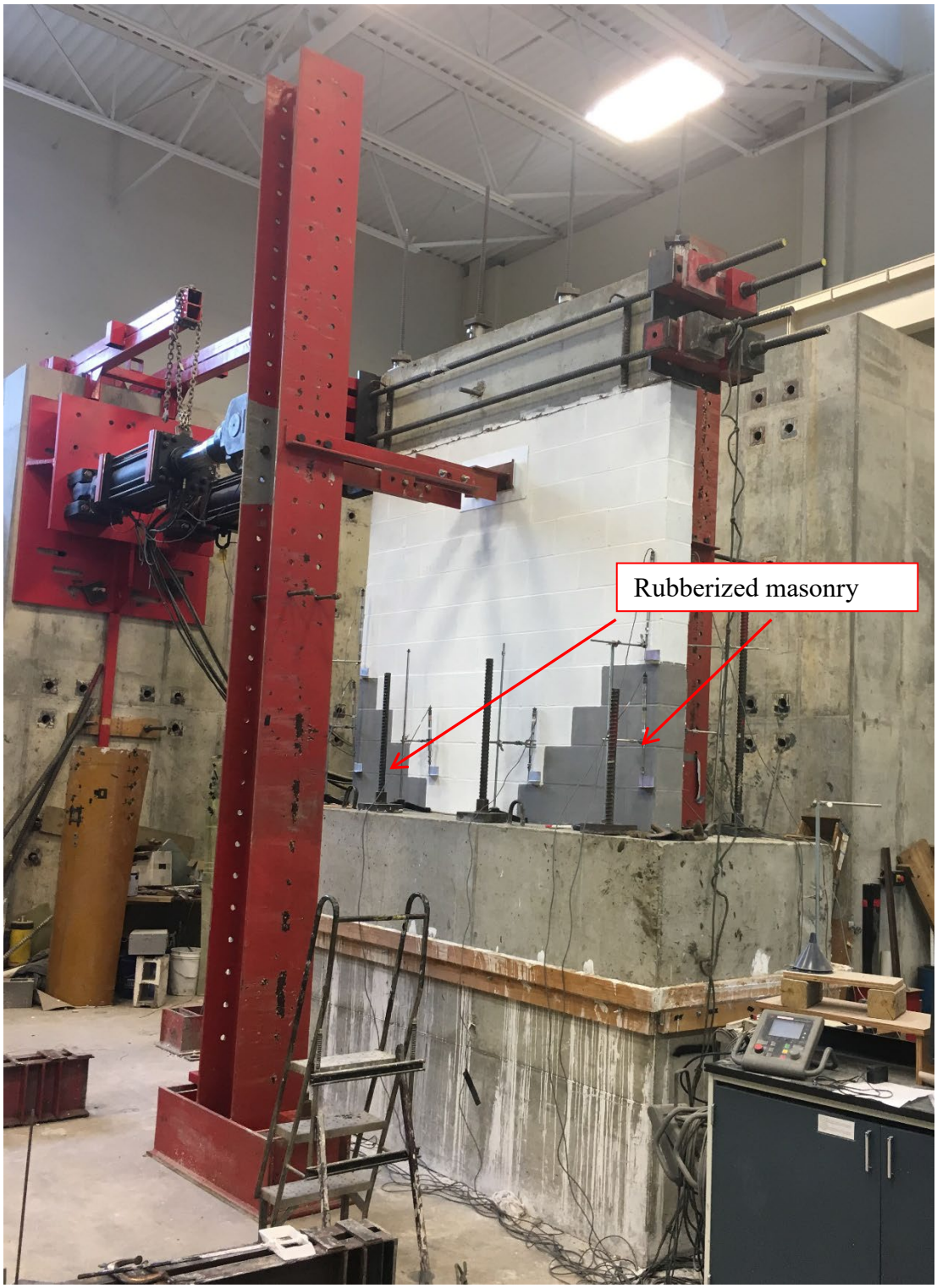

Figure 4.4: Rubberized masonry shear wall.

Figure 4.5: Conventional masonry shear wall.

4.2.1.1.Material Properties

Standard hollow 203 mm (8 in.) CMU blocks were used in constructing the walls in running bond and face shell bedding. The construction material characteristics, per the different ASTM standards, are presented in Table 4.3.

Table 4.3: Material Properties

Items	**Standard Tests**	**Results**	
Mortar (type S)	ASTM C39 / C39M-18	$f'_c = 20.7$ MPa	
Grout	ASTM C1019-18	$f'_g = 30.4$ MPa	
Masonry block prisms	ASTM C1314-18	Grouted stretcher block prisms	$f'_m = 24.2$ MPa
		Grouted end block prisms	$f'_m = 23.3$ MPa
Rubber block prisms		$f'_m = 21.4$ MPa	
Wall Footing	ASTM C39 / C39M-18	$f'_c = 41$ MPa	
RC pedestal	ASTM C39 / C39M-18	$f'_c = 41$ MPa	
Top beam,	ASTM C39 / C39M-18	$f'_c = 69$ MPa	
High strength post-tensioned bars	ASTM A325M − 18	$f_y = 1062$ MPa	

4.2.1.2.Wall construction

Both the walls had an aspect ratio of 0.85. The walls had PVC tubes (vertical ducts) running through the blocks at the intervals of the required vertical reinforcements. This allowed vertical PT bars to be integrated into the system and stressed later hence making the walls unbonded PT walls. The PT bars were placed in a fixed position in the footing as shown in Figure 4.6. The walls were fully grouted in three different lifts. The walls were constructed by experienced masons.

Figure 4.6: Wall construction.

4.2.1.3.Test Setup

The walls had a heavily reinforced foundation to act as a rigid base. The post-tension bars were connected to the footing using a base plate at the bottom of the footing that allowed post tensioning. The PVC duct detailing at the footing is shown in Figure 4.7; such details were required to install the nuts and plates. The wall foundation beams were post-tensioned on a heavily reinforced concrete pedestal as shown in Figure 4.5.

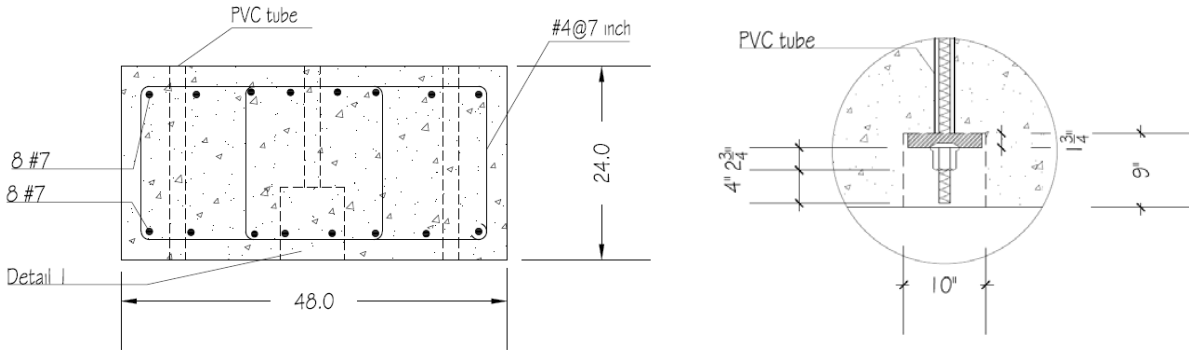

Figure 4.7: Detailing of post-tension inside the wall footings.

The walls were loaded using a top beam. This RC beam allowed even distribution of the post-tensioned loads on the entire cross-section of the wall and allowed transfer of the cyclic load to the wall. The top beam had PVC ducts that allowed the PT bars from the walls to pass through and be post-tensioned prior to testing. Figure 4.8 shows the top beam attached to the lateral load rigid built-up adaptor used to connect the the two lateral load actuators to the loading beam.

Figure 4.8: Loading top RC beam.

To resist any unintended out-of-plane deformations, bracings were used as shown in Figure 4.10. Both bracings had lubricated Teflon sheets attached to the walls to allow smooth sliding of the walls while loading in plane. The test setup details are shown in Figure 4.9.

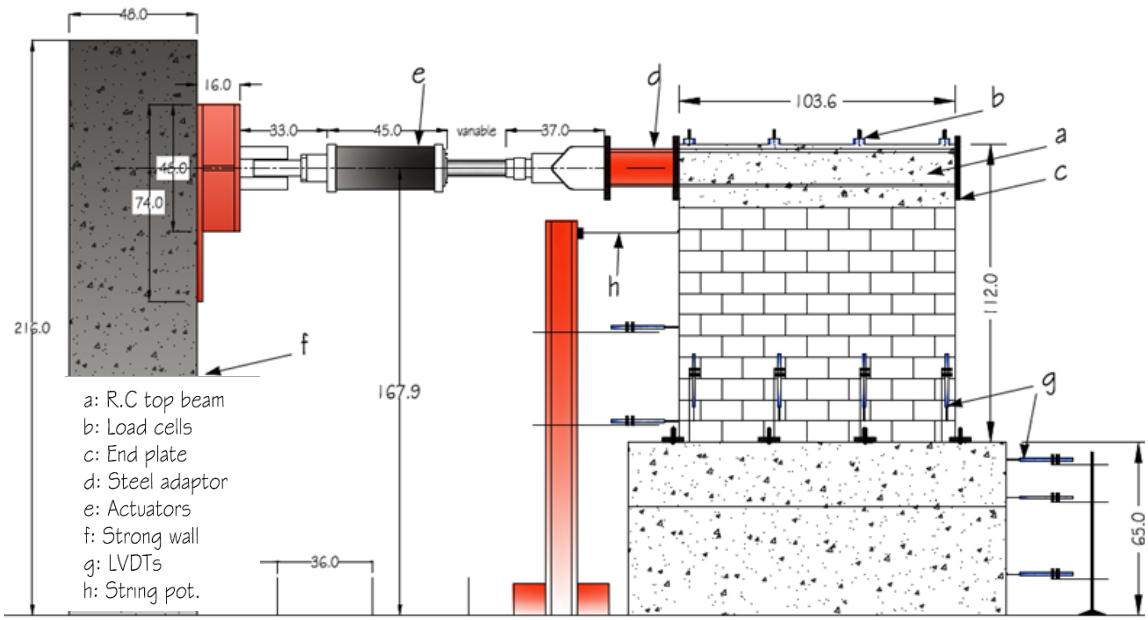

Figure 4.9: Details of the test setup.

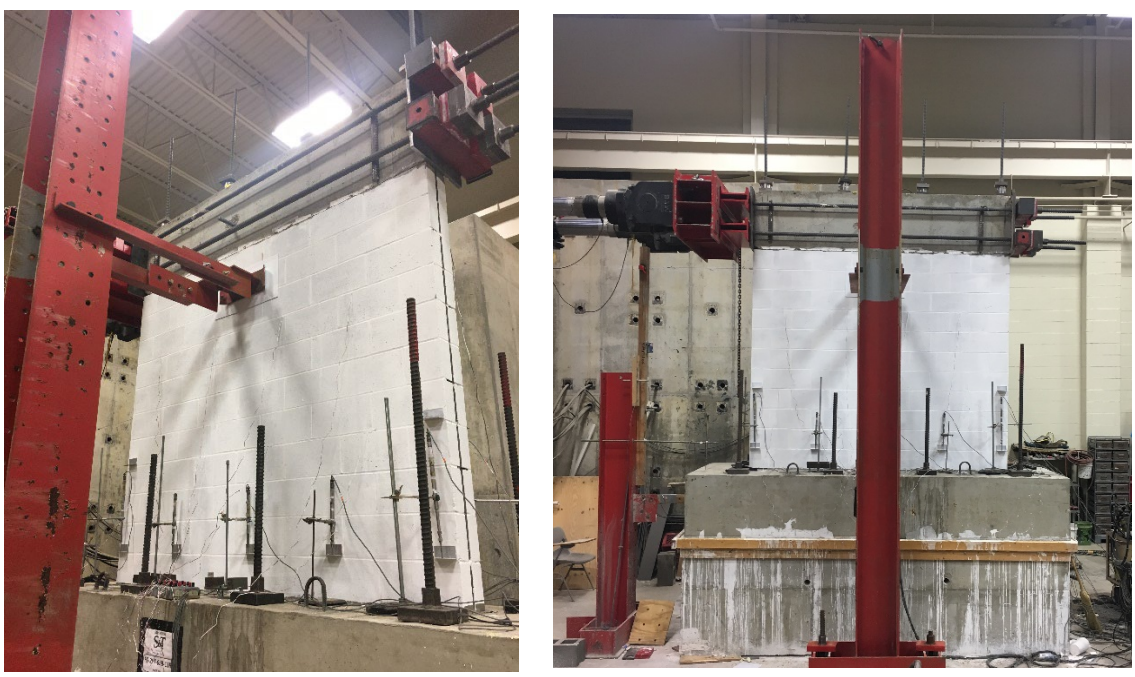

Figure 4.10: Overall test setup.

4.2.1.4.Loading protocol

The walls were subjected to a fully reversed in-plane cyclic load using two 200-kips actuators as shown in Figure 4.10. A constant frequency of 1.2 Hz was used to apply the cyclic load according to FEMA 461. As a result, every single cycle was finished within 50 seconds. The amplitude ai of the stepwise increasing deformation cycles is given by the equation $a_{i+1} = 1.4a_i$, where ai is the amplitude at i cycle. Two cycles were executed for each amplitude. The loading history is given in Figure 4.11.

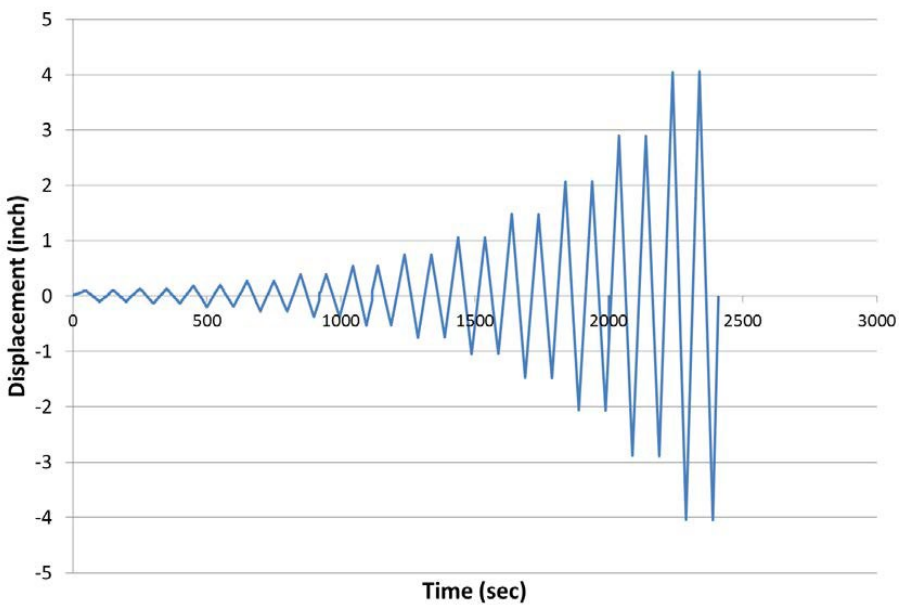

Figure 4.11: Loading history as per FEMA 461.

4.2.1.5.Instrumentation

Several LVDTs and displacement potentiometers were used to measure the load and horizontal and vertical displacements. Computerized data acquisition was used to record the readings at a rate of 10 readings per second. A total of 18 LVDTs and 2 displacement potentiometers were installed along the wall length and height to monitor the vertical and lateral displacements with respect to the wall foundation beam. This allowed separate measurement of the sliding and rocking of the foundation beam. Sensitive load cells were used to monitor the post-

tension loads prior to stressing the PT bars and during testing. The reference wall had a total 8 strain gauges attached to the horizontal rebars in the bond beams. Additionally, several digital video cameras were used from different angles to record the lateral drifting of the wall and failure modes. The instrumentation arrangement is shown in Figure 4.12.

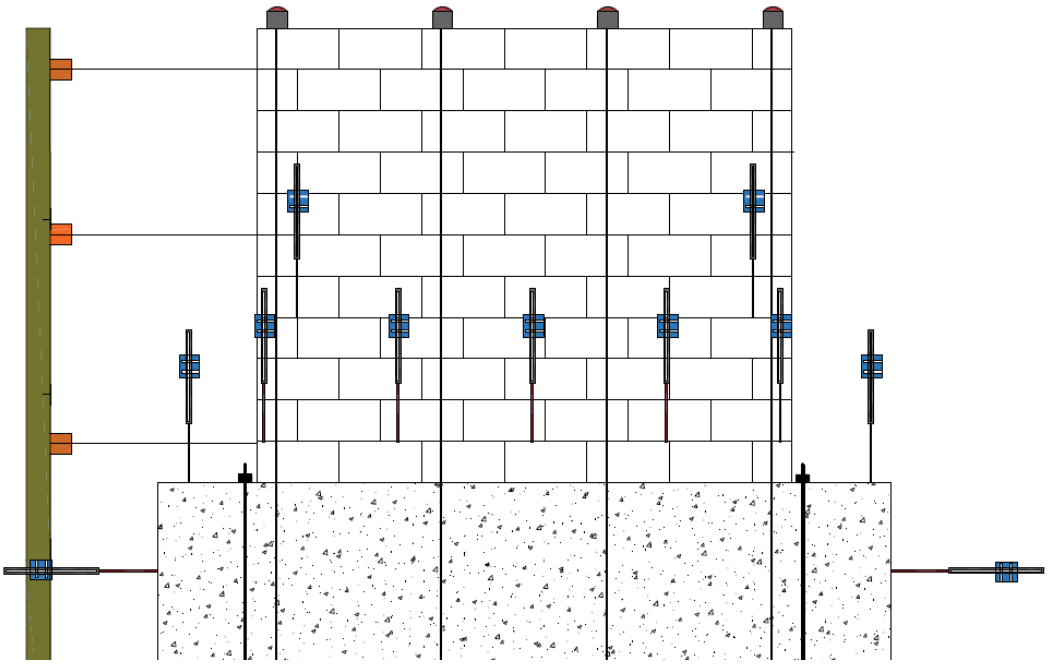

Figure 4.12: External instrumentation arrangement.

4.2.2. Experimental Results

4.2.2.1. Failure mode and extent of damage

4.2.2.1.1. The performance of the reference wall

This wall was constructed using standard CMUs. The wall maintained a linear response until yielding is observed at a displacement of 0.14 inches. The hysteresis loops are shown in Figure 4.13. Minor hairline diagonal cracks were observed and extended to the 4th course. Post-yield stiffness of the wall degraded as the wall continued with further displacement cycles. It reached a maximum load of 174 kips at a displacement of 0.67 inches, corresponding to a drift of 0.74%. Compression failure started to be observed at the toe at this point, as shown in Figure 4.14a.

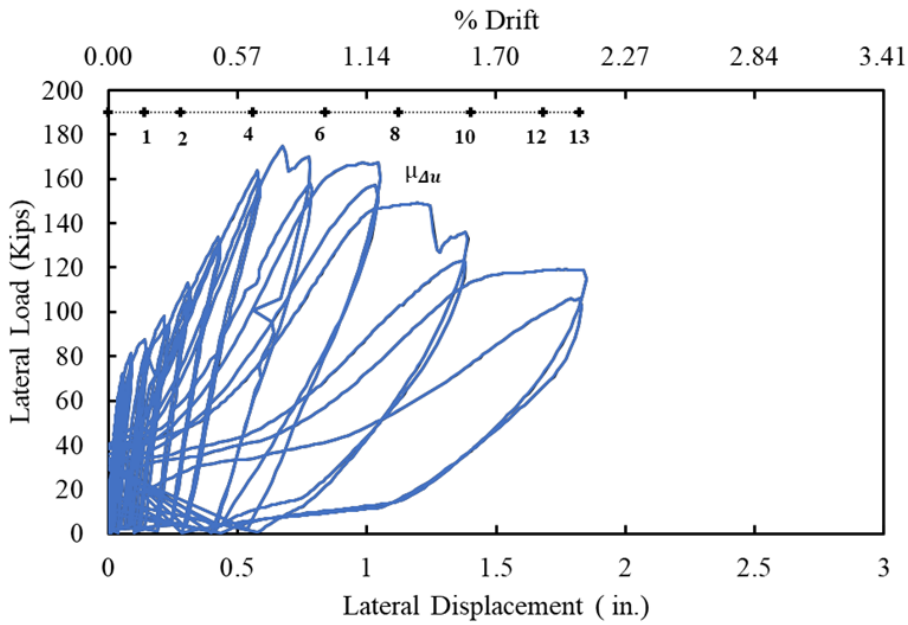

Figure 4.13: Hysteresis loops of the reference wall.

A slight drop in the maximum force was observed, and the wall continued at this maximum load for two more cycles, reaching a drift of 1.18% (Figure 4.14b). With imposing more displacement on the wall, load degradation was observed in the wall, and shear cracks developed. Spalling of the toe region as shown in Figure 4.14c was observed at 1.45% drift up to at least two blocks in length at the bottommost course. The wall displayed 42% load reduction at a drift of 2.08%. The deformation of the wall at the end of the test is shown in Figure 4.14d and 4.14e.

Figure 4.14: (a) Crushing of the toe at maximum load, (b) At drift of 1.18%, (c) Shear cracks and compression zone, (d) Deformed PVC with steel rebar embedded at the end of test, and (e) Extent of damage at the end of the test.

4.2.2.1.2. The performance of a rubberized wall

This wall had rubberized masonry units at the plastic hinge region as shown in Figure 4.4. The hysteresis loops of the wall are given in Figure 4.15. The wall reached its yield load at a displacement of 0.16 inches, corresponding to a lateral load of 102 kips. The wall maintained its linear initial stiffness up to yielding. The post-yield plateau is observed for the next 5 cycles of displacement. Compression cracks were observed at this point as shown in Figure 4.16b.

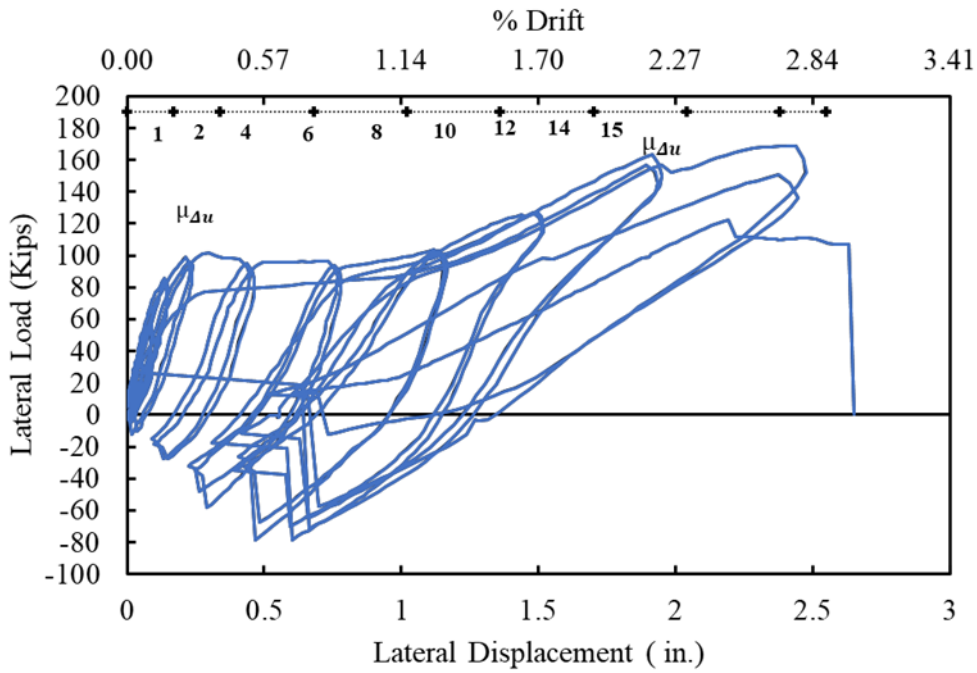

Figure 4.15: Hysteresis loops of the rubberized wall.

At a drift of 1.33%, the wall started to display hardening. At a drift of 1.7%, a compression crushing at the toe was observed with vertical splitting cracks as the wall reached a lateral load of 145 kips as shown in Figure 4.16c. In the next cycle, the wall reached its peak load of 161 kips at a drift of 2.80%. More shear cracks and spalling of face shells at the bottommost course were observed at this point. The shear cracks extended from the top corners and extended toward the toes (Figure 4.16d). In the next two displacement cycles, load degradation of 33% was observed with the wall reaching a drift of 2.88%. Beyond that the rubber blocks displayed crushing and

vertical splitting cracks (Figure 4.16e). The wide loops of the hysteresis curves show huge post-yield energy dissipation. This is discussed in detail in the later sections. The rubber blocks at the toe reached much higher strain at a higher drift compared to that of the reference wall.

(a) (b) (c)

(d) (e)

Figure 4.16: (a) Wall with rubberized blocks in the plastic hinge region, (b) Compression cracks, (c) Splitting cracks at the toe, (d) Damage extent of the different blocks at the end of the test, and (e) Damage at wall ends at the end cycles.

4.2.2.2.Deformation profile along the wall height

The curvatures over the wall height were determined based on strain profiles at different sections along the wall height. A typical strain profile for the wall cross-section is shown in Figure 4.17. The curvature, φi, corresponding to a gauge length i along the wall height, was calculated using Eq. (1) and (2). The curvature profile along the height of the wall is presented in Figure 4.18.

$$\varphi_i = \frac{\varepsilon_c}{c} \text{ or } \frac{\varepsilon_t}{l_w - c} \tag{4.1}$$

$$\varepsilon_c = \frac{\Delta_{c(i)}}{i} \text{ and } \varepsilon_t = \frac{\Delta_{t(i)}}{i} \tag{4.2}$$

where, as shown in Figure 4.17(a) and (b), φ_i = curvature at a given section along the wall height; $\Delta_{c(i)}$ = compressive displacement measurements at the compression end of the wall; $\Delta_{t(i)}$ = tensile displacement measurements at the tension end of the wall, and i is the gauge length corresponding to the measured $\Delta_{c(i)}$ and $\Delta_{t(i)}$.

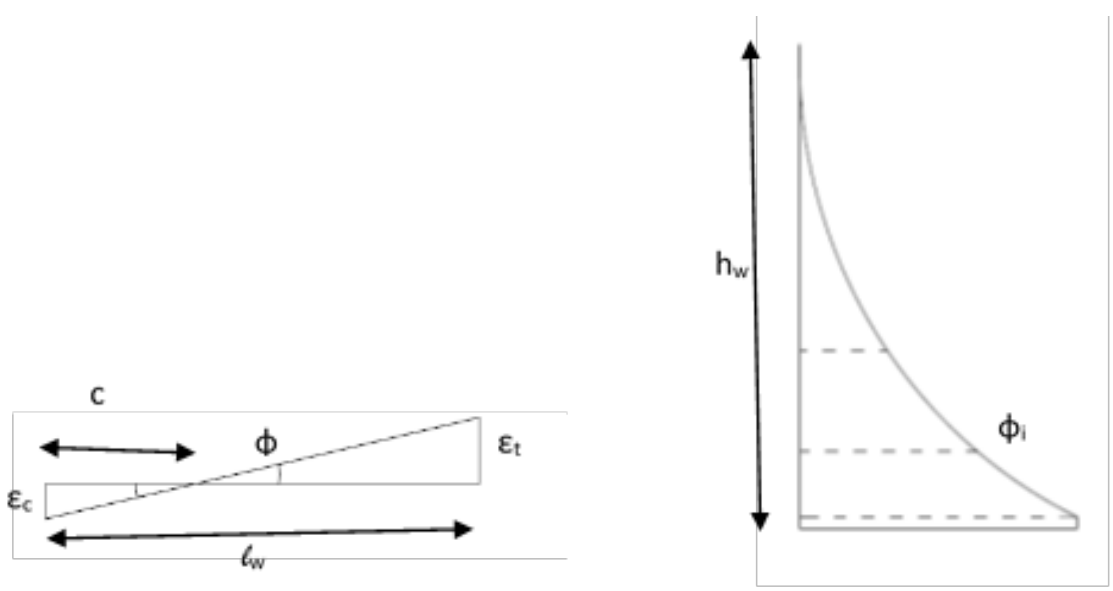

(a) (b)

Figure 4.17: Curvature: (a) At a cross section, and (b) Curvature profile along wall height.

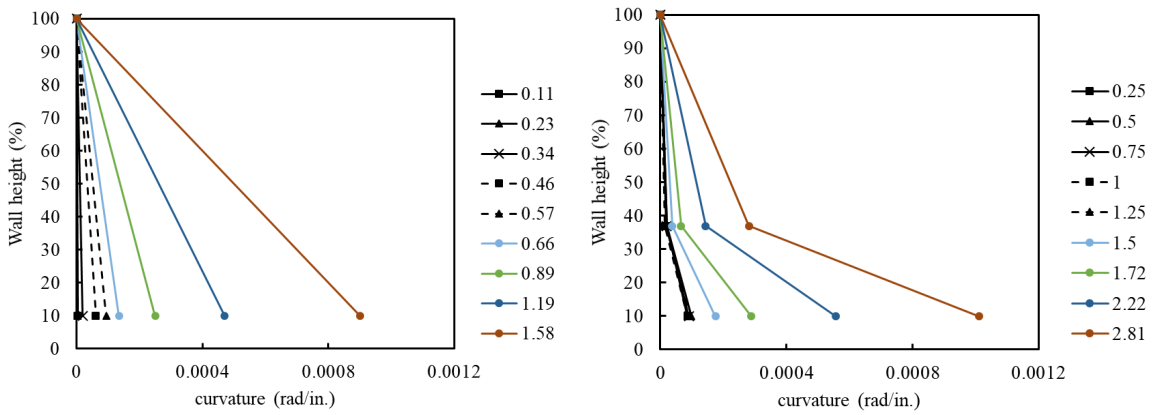

(a) (b)

Figure 4.18: Curvature profile along with wall height of the walls at different % drift levels: (a) Reference wall, and (b) Rubberized wall.

The curvatures over the wall height for the reference wall were measured only at the base course. Nonetheless, the rubberized wall displayed inelastic deformation at the plastic hinge region. At the bottommost sections of both walls, the average curvatures measured at initial drift levels were the same. However, the reference wall reached higher curvatures at much smaller drift levels. At the ultimate load, the rubberized wall reached a curvature 12% higher than that of the reference wall. It should be noted that the rubberized wall had an ultimate drift 1.8 times that of the reference wall. Furthermore, as shown in Figure 4.18, the rubberized wall displayed a significant inelastic deformation up to 37% of the height of the wall measured from the bottom of the wall, i.e., the four courses where RCMUs were used.

4.2.2.3.Strain profile along the wall length

Average strain profiles over several locations along the wall length at the bottommost section were calculated based on the measurements of the DCVTs. The rubberized wall had DCVTs attached at three different locations, whereas the reference wall had the DCVTs attached at four different spacings. Due to the spalling of the face shells at the wall toes, strain readings were not measured at the last cycle of each wall.

Figure 4.19 shows the strain profile along the length of the wall for both the reference and rubberized walls. The reference wall surpassed the TMS 402/602 specified maximum compressive strain of 0.00250 at a drift level of 0.66%, whereas the rubberized wall reached a compressive strain of 0.00312 at a drift level of 1.72%. Both the walls reached ultimate strains of almost eight times the specified ultimate strain. However, the rubberized wall attained this level of strain at a drift level of almost 1.8 times that of the reference wall.

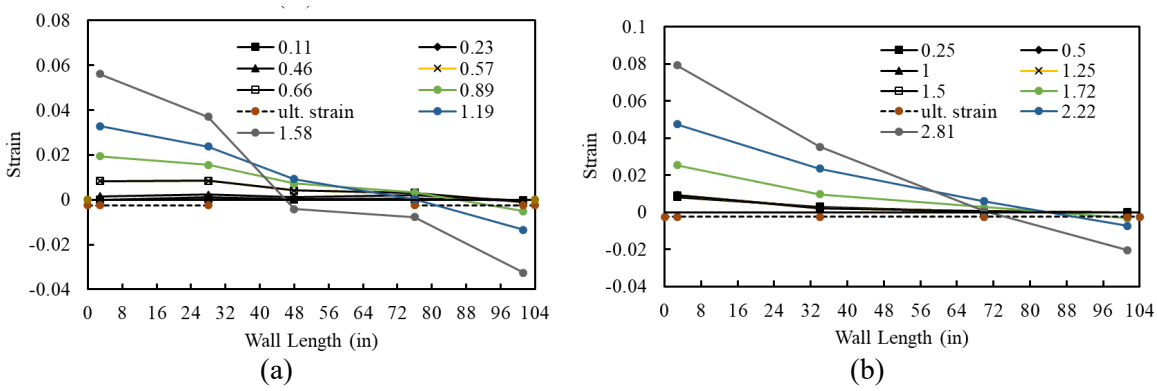

Figure 4.19: Strain profile along wall length at different % drift levels: (a) Reference wall, and (b) Rubberized wall.

4.2.2.4.Load displacement response

Figure 4.20 presents the load-displacement envelopes for both walls. The elastic stiffness of both walls is quite similar. The walls differed significantly in their post-yield behaviors. The rubberized wall underwent a perfectly plastic region post-yielding. It reached the peak load at a drift level 2.62 times that of the reference wall. Moreover, at 20% strength degradation, the drift displayed by the rubberized wall was 80% higher than that of the reference wall. Therefore, the use of RCMUs has enhanced the capability of the wall to significantly deform in the plastic region.

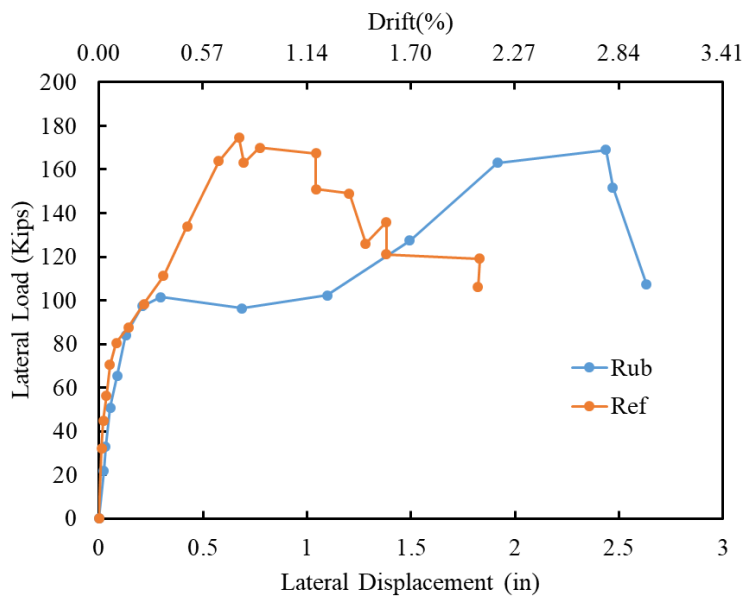

Figure 4.20: Load-displacement envelope for the investigated walls.

4.2.2.5.Displacement ductility

The displacement ductility measured for the walls is defined as the ratio between the measured top displacement at a specified limit and the idealized yield displacement. The displacement ductility is shown on the hysteresis loops for the walls in Figure 4.13 and 4.15. A trilinear idealization has been done to obtain the idealized load-displacement envelope of the walls. The measured displacement ductilities presented here are at maximum load, $\mu_{\Delta u} = \frac{\Delta_u}{\Delta_y}$, and at

failure, $\mu_{\Delta 0.8u} = \frac{\Delta_{0.8u}}{\Delta_y}$ where Δ_y is the effective yield displacement, and $\Delta_{0.8u}$ is the displacement at 20% reduction in ultimate strength. The displacement ductilities are given in Table 4.4.

The idealized yield displacement is quite similar for both walls. However, at ultimate load, $\mu_{\Delta u}$ the rubberized wall is almost 3 times the reference wall. At 20% strength degradation, $\mu_{\Delta 0.8u}$ for the rubberized wall is 1.5 times that of the reference wall. The ductility of the wall has been significantly enhanced with the use of RCMUs at the wall ends.

Table 4.4: Displacement Ductility

Wall ID	Δy	Δu	Δ0.8u	$\mu_{\Delta u}$	Drift %	$\mu_{\Delta 0.8u}$	Drift %
Reference wall	0.14	0.67	1.38	4.78	0.74	9.86	1.52
Rubberized wall	0.17	2.44	2.5	14.64	2.68	15.00	2.75

4.2.2.6.Energy dissipation

In seismic design, high energy dissipation is desirable as it reduces the seismic demand. The amount of energy dissipation is calculated as the area enclosed within the lateral load-displacement hysteresis loop at each displacement cycle (Hose et al. 2000). Figure 4.21 presents the total amount of energy dissipated for each wall at different displacement levels. As shown in the figure, the rubberized wall has high energy dissipation at each displacement level compared to the reference wall. For higher displacement levels, the rubber wall displayed a 20% increase in energy dissipation. The total energy dissipated by the rubberized wall is 64% higher than that of the reference wall.

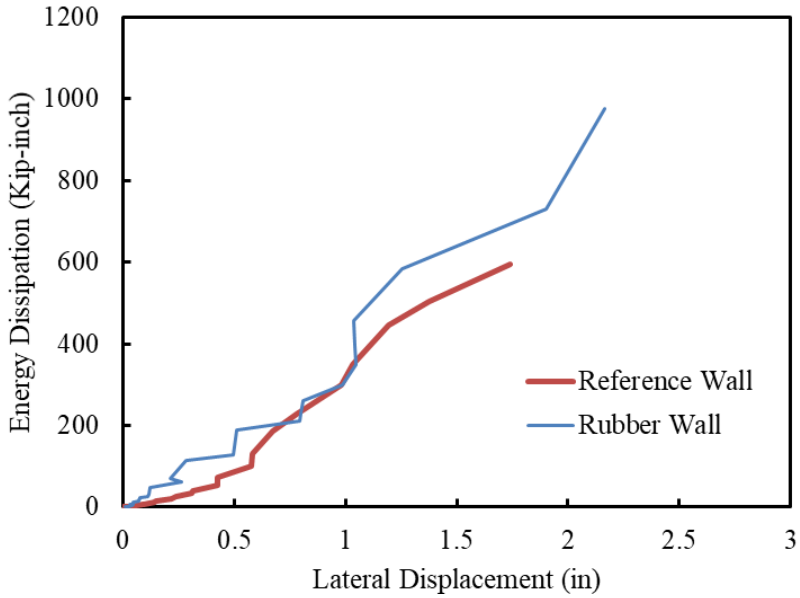

Figure 4.21: Energy dissipation.

4.2.2.7. Equivalent viscous damping

The equivalent viscous damping ratio, ζ, is plotted against the displacement in Figure 4.22 for both walls. The equivalent viscous damping was calculated as follows (Priestley 2006):

$$\zeta = \frac{1}{4\pi}\frac{E_d}{E_s} \tag{4.3}$$

where E_d = energy dissipated in a cycle (the area inside a loop) and E_s = strain energy at the peak load of the cycle. For each loading cycle, the equivalent viscous damping was calculated and added to find the total equivalent viscous damping up to that displacement level. Figure 4.22 shows that with increasing the displacement levels, ζ increased as well. The rubberized wall systematically displayed higher damping ratios compared to the reference wall. At the ultimate displacement of the reference wall, the rubberized wall displayed approximately twice the equivalent damping compared to that of the reference wall.

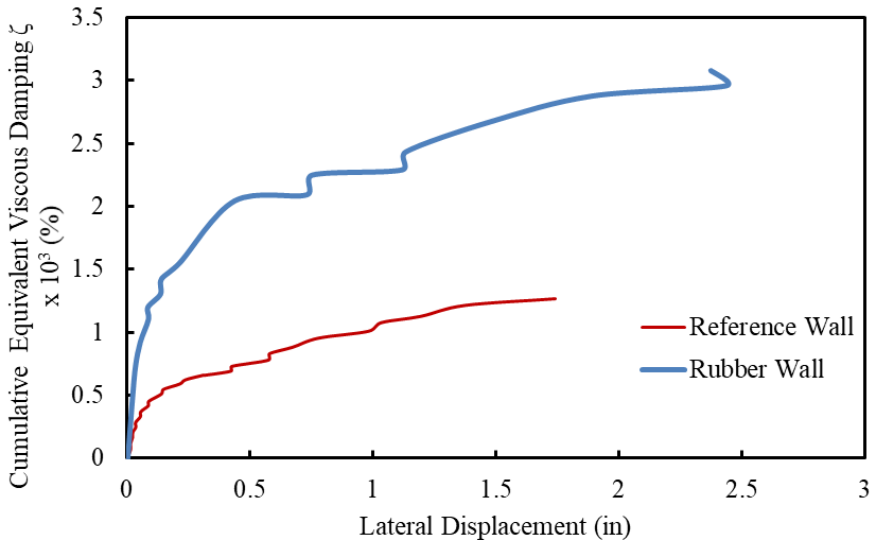

Figure 4.22: Equivalent viscous Damping, ζ (%).

4.2.3. Conclusions

Four different ratios of crumb rubber, namely, 0%, 5%, 10%, and 15%, were used as a replacement for mineral fine aggregate. RCMU prisms having a height of four blocks were investigated for their strength and strain capacity. The prisms were subjected to a monotonic load in a displacement control. The compressive strength, peak strain, and initial stiffness of the RCMUs prisms were compared to those of the CMU prisms. Furthermore, two full-scale masonry walls were investigated. One wall was constructed using reference CMUs while the second wall was constructed using CMUs except at the toes that were constructed using RCMUs. Based on the experimental investigation, the following conclusions can be drawn:

• There is no significant loss in the compressive strength when RCMUs were produced using 5% crumb rubber. However, using higher percentages of rubber decreased the masonry's compressive strength.

• The use of rubber in masonry block units has a significant impact on increasing the peak strain and ductility.

• The wall having RCMUs displayed similar strength to the reference wall. However, the rubberized wall displayed higher energy dissipation and ultimate strain.

5. Masonry Thermal Characterization

The first part of this chapter focuses on the thermal characterization of RCMUs having rubber contents of 0, 5, 10, and 15% as a partial replacement of natural fine aggregate. As a preliminary investigation, cement paste mixtures with the same rubber ratios of 0%, 5%, 10%, and 15% were prepared and tested for their thermal performance. The differential scanning calorimetry (DSC), differential thermal analysis (DTA), and thermogravimetric analysis (TGA) tests were conducted to determine the specific heat, the change in the mass under elevated temperature, and the phase transition point. Then, another four tests were conducted to study the effects of rubber content on the thermal conductivity of the RCMUs (ASTM C1363) or their material (ASTM D5334 and CRD-C 45-65) energy consumption (ASTM.C1363), and the time needed to reach steady state (ASTM C136). Figure 5.1 illustrates a schematic overview of the whole chapter.

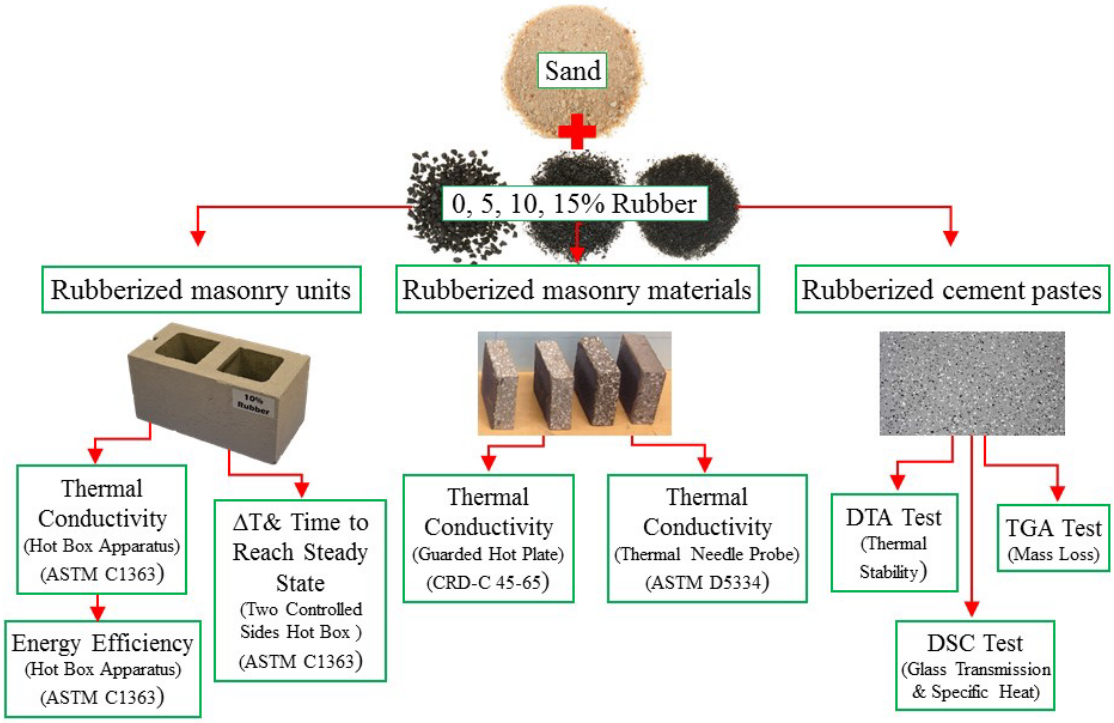

Figure 5.1: Gyratory compactor employed for determining the packing density of aggregate combinations.

The second part of this chapter focuses on retrofitting conventional masonry units with eco-friendly rubberized plastering. During this part, two grades of double recycled rubber that were collected as a byproduct from the scrap tire recycling plant were used in this study as a cement or fine aggregate replacement in plastering cement mortar. Ratios of 0, 10, 20, 30, and 40% of rubber powder were used as volume replacement of cement and fine aggregate, respectively. The physical characterizations of the new proposed materials were studied first including compressive strength, flexure strength, direct tensile strength, strain energy, toughness, drying shrinkage, thermal conductivity, heat resistivity, and sound absorption. The thermal and acoustic retrofitting performance was investigated for masonry units with a layer of the proposed material. They layers were plastered with varied ratios of rubber powder replacement and varied thicknesses. The effectiveness of the proposed retrofitting system was evaluated in cold and hot conditions to determine the effect of climate. In terms of the acoustic retrofitting, the sound absorption coefficient and the noise reduction factor were investigated under a varied range of frequency from 0 to 5000 Hz. All of the above characterizations were compared with the performance of conventional and lightweight masonry units.

5.1. Thermal characterization of rubberized concrete masonry units.

5.1.1. Experimental Program

As it was explained in chapter 2, crumb rubber from scrap tires was used as a mineral aggregate replacement to produce rubberized concrete masonry units (RCMUs) with four different ratios of rubber content, namely 0%, 5%, 10%, and 15%.

5.1.1.1.Thermal characterization of rubber particles

First, the rubber particles were examined for their thermal behavior before incorporating them within the concrete mixtures for thermal insulation purposes. The main reason behind these examinations was to clear any doubt by using a hydrocarbon material in relatively high and low-

temperature conditions. In addition, the thermal analysis of rubber particles can clarify and help in the prediction of mechanical behavior under high or low temperatures.

The first test was Differential Scanning Calorimetry (DSC), which exposes rubber particles to a wide temperature range. Thermal Analysis (TA) Instruments (DSC 2010) was used to determine the transition glass point. The instrument works under a temperature range of -180 to 725° C, while the heat flow associated with thermal transitions in the material is recorded. In the terms of low temperature, as shown in Figure 5.2, the glass transition point was at -65° C, which is far from the lowest expected temperature in the United States. The glass transition point is the point at which when rubber material hardens to a condition similar to glass, a well know phenomenon for the rubber material.

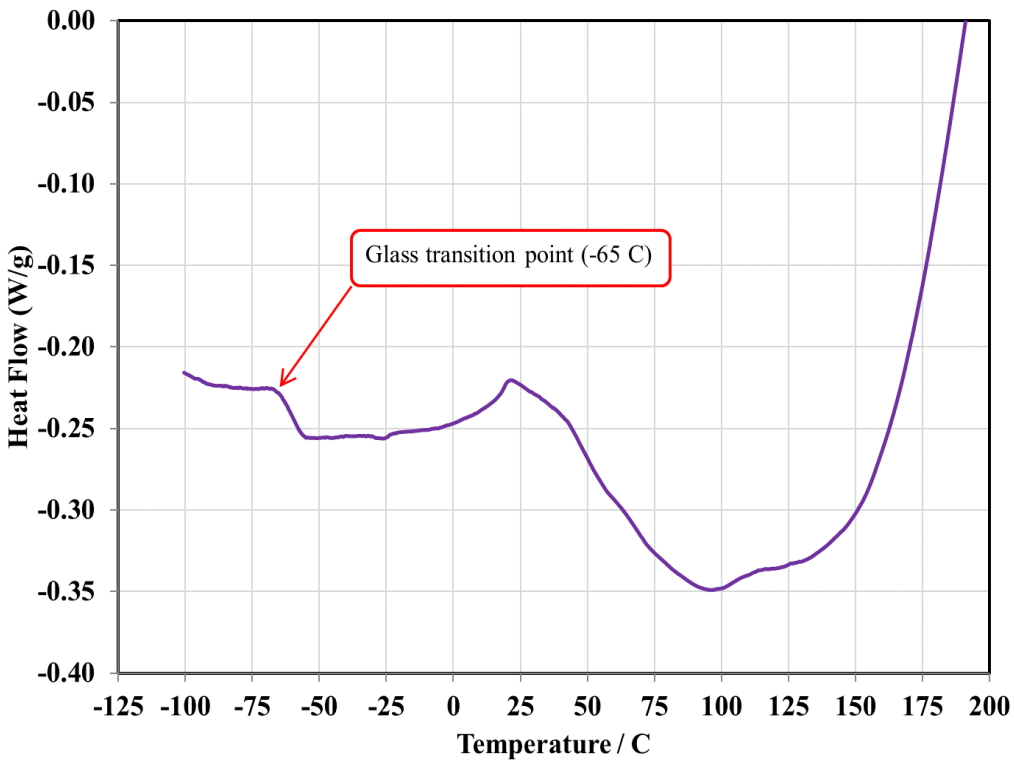

Figure 5.2: Differential scanning calorimetry (DSC) of crumb rubber.

5.1.1.2.Thermal characterization of rubberized cement paste

Mixes of cement and rubber powder were prepared using rubber replacement ratios of 0, 5, 10, and 15% of Portland cement by weight. The mixtures were used to preliminarily investigate the thermal characteristics of rubber-modified paste using differential scanning calorimetry (DSC), differential thermal analysis (DTA), thermogravimetric analysis (TGA), and specific heat tests. These tests can help to determine the potential of using rubber to improve the thermal efficiency of masonry units.

For mixture preparation, the rubber powder was added to cement in a stainless-steel mixer and mixed for two minutes. Then, the required amount of water was added to the mix and mixed for two minutes. The water to cement ratio in all investigated specimens was kept at 0.35. The paste was then poured into circular aluminum pan molds with a typical diameter of 8mm and depth of 5mm. The specimens were cured at ambient temperature in the lab for 28 days.

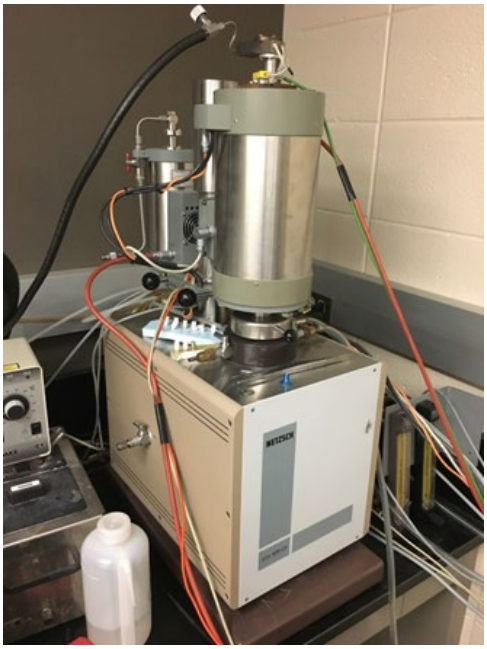

Figure 5.3: NETZSCH simultaneous TGA/DTA.

Both the TGA and DTA analyses were run simultaneously using Netzsch Simultaneous TGA/DTA (Figure 5.3), which is a thermal analysis instrument that can provide information such as phase changes, melting and glass transition temperatures, and weight loss as a function of temperature that varies from room temperature to 1500 °C under a controlled environment. The TGA analysis investigates the thermal stability and composition of the rubberized paste. The DTA studies the difference in temperature between the tested rubberized paste and a thermally inert reference under varied temperatures. As a result, the transition temperatures of the rubberized paste can be determined.

As shown in Figure 5.4, up to 300° C of all rubberized and reference mixtures behaved similarly. Within the 0 – 300° C range, each specimen lost about 2 - 3% of its weight due to dehydration of the hydrated paste. The TGA curves for rubberized paste mixtures show a noticeable mass loss in the 300 – 500° C interval with the 15% rubber content paste mixture displaying the highest mass loss with a mass loss of 8%.

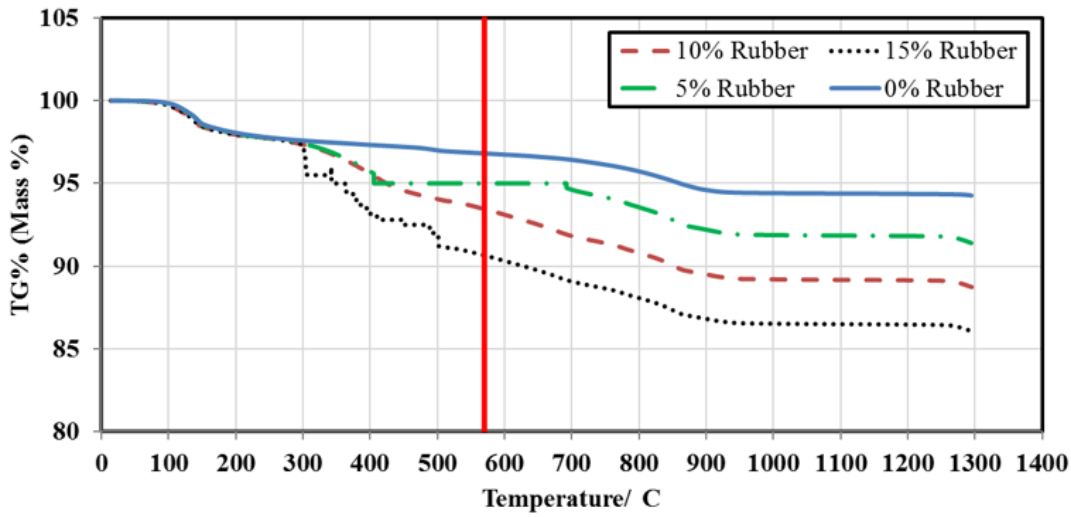

Figure 5.4: Thermogravimetric analysis (TGA) for cement mixes with varying rubber content.

DTA curve (Figure 5.5) shows an intense peak centered at 350° C for samples with 15% rubber. This peak is followed by a less intense range, due to the presence of liquid oil. The same

trend was reported for tests of scrap tire rubber only (Berrueco et al. 2005, Rada et al. 2012). However, the reference sample without rubber had a smooth curve without any point of inflection due to the absence of any organic liquid oil component. Samples with 5 and 10% rubber had a transition behavior between the samples with 0 and 15% rubber.

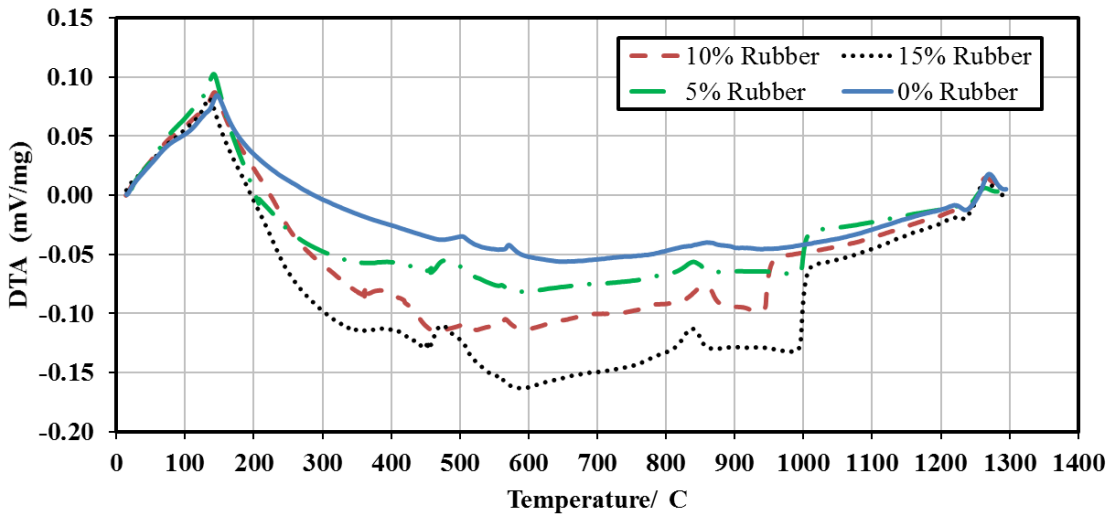

Figure 5.5: Differential thermal analysis (DTA) for cement mixes with varying rubber content.

The last test to examine the thermal characteristics of rubberized paste is the specific heat. Specific heat represents the heat required to raise the temperature of the unit mass by one degree. Therefore, samples with relatively high specific heat represent better thermal insulation. The specific heat was measured for five samples with varied rubber content, namely 0%, 5%, 10%, 15%, and 100% (rubber only). Samples similar to those used for thermal characterization of rubberized paste mixtures were used during this test.

Figure 5.6a shows the heat flow vs. temperatures for different rubberized paste mixtures. Figure 5.6b represents the specific heat of different mixes at 30° C, 45° C, and 60° C. The specific heat was calculated using the following equation:

$$C_p = \left[\frac{60E}{H_r}\right]\frac{\Delta H * 10^9}{m} \tag{5.1}$$

where:

E= cell calibration at the temperature of interest (dimensionless)

Hr= heating rate (°C /min)

ΔH= difference in y-axis deflection between the sample and blank curve at the temperature of interest

m= sample mass (kg)

Cp= specific heat (J /kg K)

As shown in Figure 5.6b, the relation between the rubber content and specific heat is approximately linear, which represents the impact of having rubber on the thermal insulation. The figure also shows that the effects of rubber on specific heat at high temperature, i.e., 60° C is less pronounced compared to its effects at lower temperature, i.e., 30° C and 45° C. The specific heat for rubberized paste mixtures at 30° C, 45° C, and 60° C can be determined using Equations 5.2 through 5.4, respectively.

$$C_p = 5.3110R + 922.04 \quad (5.2)$$

$$C_p = 5.5196R + 950.30 \quad (5.3)$$

$$C_p = 3.5353R + 1045.8 \quad (5.4)$$

where:

Cp= specific heat (J/kg. K)

R= rubber ratio (%)

The preliminary results presented from this set of tests indicate that the rubberized paste behaved thermally similarly to a conventional paste up to 300° C and can sustain extreme hot and cold weather and hence can be used for building envelopes. Therefore, it was encouraging to proceed with the second part of this research where the thermal characterization of RCMUs was determined.

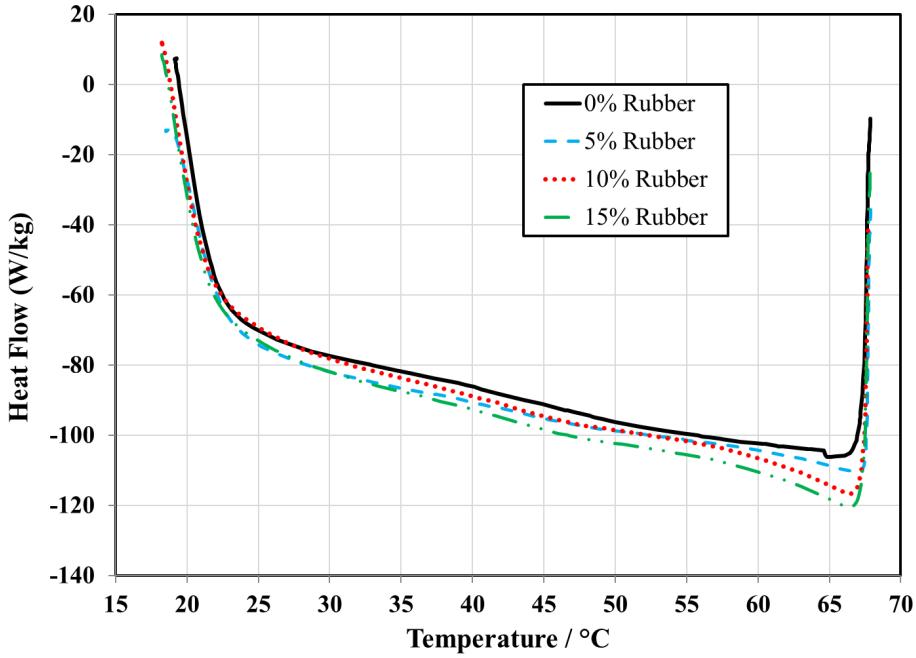

a

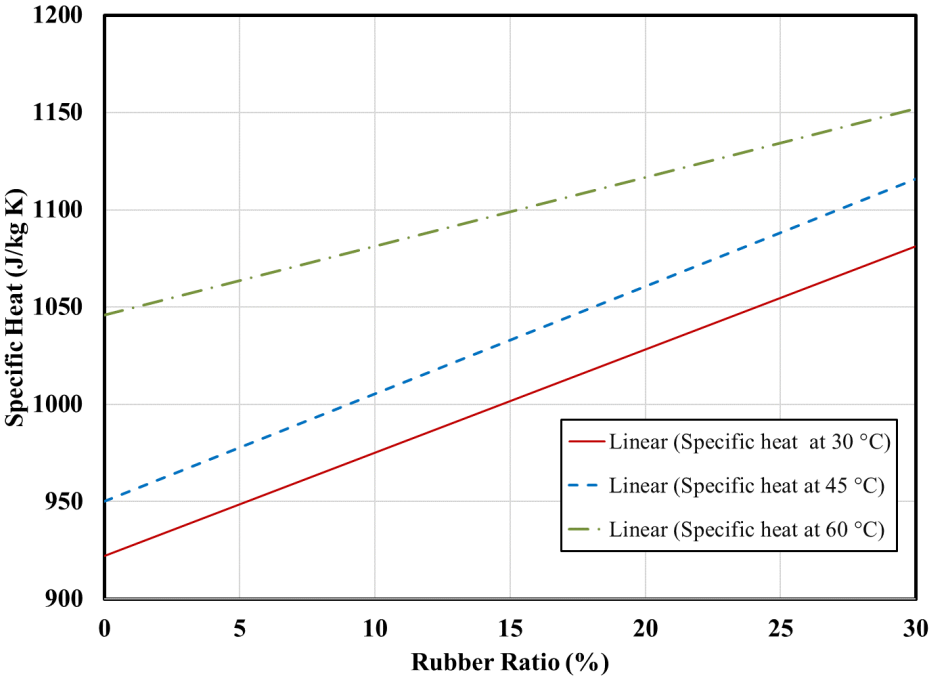

b

Figure 5.6: Specific heat test of rubberized cement paste (a) Heat flow vs. temperature, and (b) Specific heat vs. rubber content.

5.1.1.3.Thermal conductivity of RCMUs

During this experimental work, the thermal characteristics of RCMUs were determined using four different approaches, namely the thermal needle probe, the two controlled sides guarded hot box, the guarded hot box, and the guarded hot plate assembly.

5.1.1.3.1. Thermal needle probe method

A portable thermal analyzer that has a metal probe with a high aspect ratio can be used to measure the thermal conductivity of various kinds of materials, per ASTM D5334−14. This method was originally designed to measure the thermal conductivity of soil where the needle probe can be inserted with a small amount of pressure without the need to create a hole prior to inserting the probe for the test. In this case, full contact is assured between the probe and the tested material. However, the measurement of stiff materials such as masonry using the needle probe has some challenges compared to measurement of the soil medium. As the standard probe has a diameter of 3.9 mm, a drill bit was used to create a 4-mm diameter hole in an RCMU where the probe could be inserted. The probe was covered with a thermal grease to assure full contact between the probe and surrounding materials and eliminating any entrapped air that could lead to inaccurate results. The metal probe contained a heater element and a temperature sensor. Once the probe is inserted into the sample, a current is passed through the heater, which raises the temperature, and the temperature sensor records the change with time. After cycles of heating and cooling, the temperature degradation will be recorded with time to calculate the ability of the material to absorb and dissipate heat, determining the thermal conductivity using the KD2 Pro portable thermal properties analyzer (Figure 5.7a). The test was conducted in five different spots within the masonry unit, namely the face shell, end shell, web, the intersection between the face and web shells, and the intersection between the web and end shell (Figure 5.7b). The thermal conductivity was calculated for each RCMU.

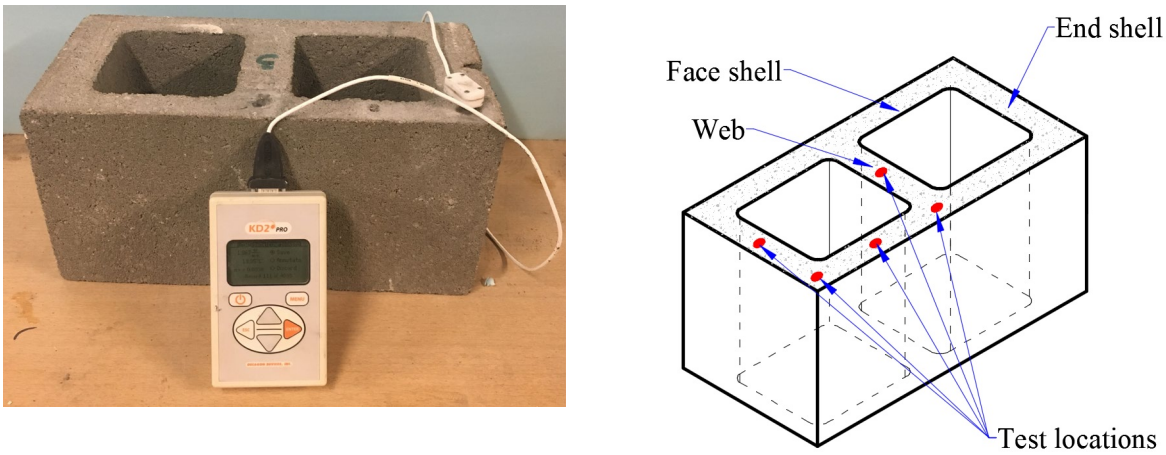

(a) (b)

Figure 5.7: Thermal needle probe test using KD2 PRO portable thermal properties analyzer (a) testing the RMCU (b) CMU component test locations.

5.1.1.3.2. Guarded hot plate assembly method

This test was conducted following the Whole Building Design Guide CRD-C 45-65 on 100 mm X 100 mm X 25 mm masonry plate specimens. As shown in Figures 5.8 and 5.9, the apparatus used in this test consisted of a guarded hot plate, controlled heat source, temperature measurement system and energy consumption meter. The guarded hot plate apparatus was fabricated using double layers of 50 mm thick corkboard surrounded by 20 mm thick plywood. The corkboard was preferred to Styrofoam because of its high insulation value even with full contact with the hot plate. As shown in Figure 5.8, the layers of corkboard were arranged around the tested specimen in a way that blocked the path of any possible leaks through the joints. Therefore, all the heat transferred vertically through the tested sample only without significant dissipation through the walls or the joints in the other directions.

A 100 mm X 100 mm X 3mm aluminum plate with a slim heat sheet was used as a heat source that kept the temperature at 60° C ± 2° C using a proportional integral derivative (PID) digital temperature controller. A similar aluminum plate was also placed atop each test specimen

to measure the temperature of the collected heat at the top side. To achieve full contact between the aluminum plates and the tested sample, thermal grease was used to cover the contact areas.

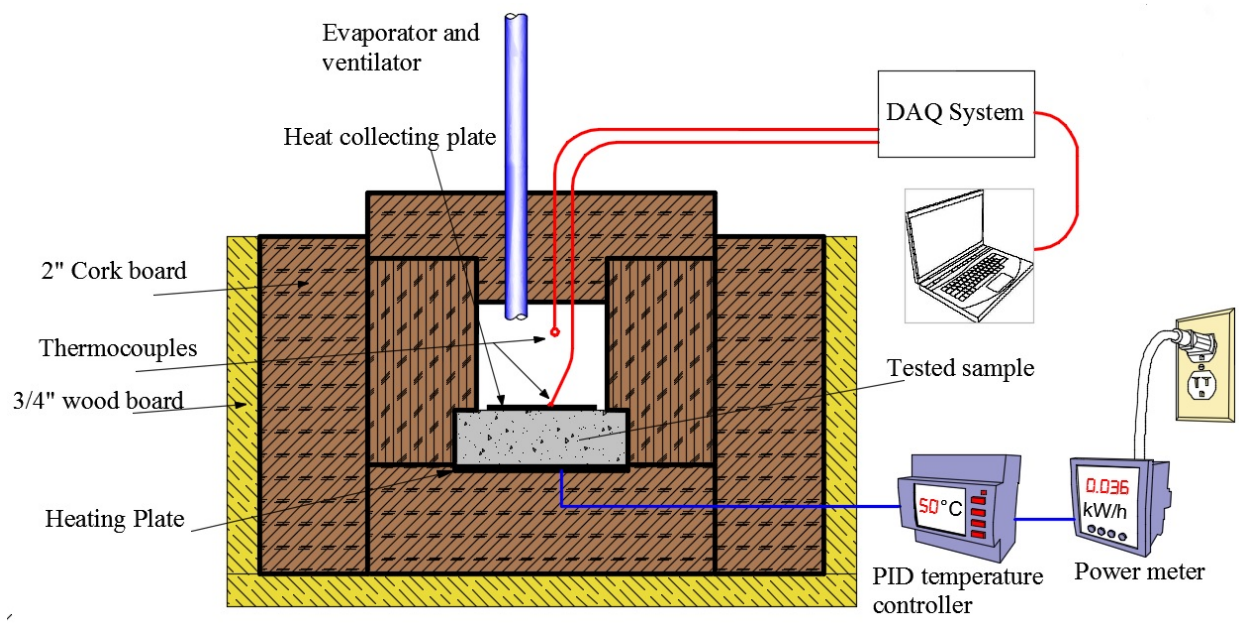

Figure 5.8: Thermal conductivity apparatus general layout.

The temperatures of the aluminum plates above and below each test specimen were measured using a set of thermocouples connected to a data acquisition system. Once a specimen is placed inside the Guarded Hot Plate apparatus, the upper box door (that made out of 50-mm thick layer of corkboard) was tightened and sealed to eliminate heat leaks. The heating plate was then turned on for 24 hours to reach a temperature of 60° C ± 2° C measured at the bottom side. The temperature data were collected at the top side with a rate of 10 readings per minute using the data acquisition system (Figure 9b), and the consumed energy was recorded for the whole testing time using a digital power meter. The thermal conductivity of each specimen was then calculated using Fourier's heat conduction equation, as follows:

$$k = \frac{qL}{A(t_1 - t_2)} \tag{5.5}$$

where:

k: thermal conductivity factor, (W/m K).

L: thickness of the tested specimen, (m).

A: area of the tested specimen, (m^2).

t_1: the temperature of the bottom aluminum (hot) plate face in contact with the specimen, K.

t_2: the temperature at the top aluminum (heat collecting) plate on the top face of the sample, K.

q: heat flow rate within the tested specimen, W/m^2. (q = 3.41 times the rate of electrical energy input to the hot plate, Watts).

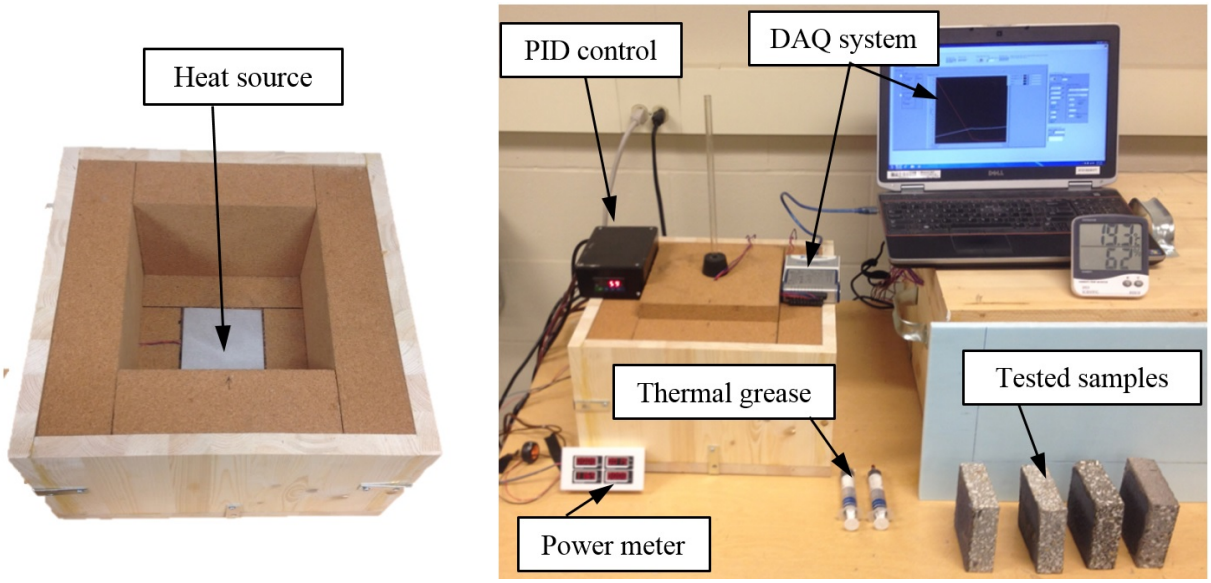

(a) (b)

Figure 5.9: Thermal conductivity measuring system: (a) Testing box, and (b) The entire system.

5.1.1.3.3. Two controlled sides guarded hot box apparatus

The heat transfer across a CMU was determined, per ASTM C1363−11, by placing a CMU in the middle of a well-insulated box (Figure 5.10) where one face shell of the CMU was subjected to a constant temperature of 49.5±0.5° C while the other face shell was not subjected to any heat. The heat was emitted from an aluminum plate and controlled by a PID controller, as explained earlier (Figure 5.10a). The testing apparatus was fabricated using an exterior 12.5 mm thick plywood and interior 50 mm thick Styrofoam with a thermal resistance value (R) equal to 10 on the inner face. The Styrofoam inner faces were engraved as shown in Figure 5.10a to assure a tight fit for the masonry unit to eliminate any masonry manufacturing tolerance that may cause a heat leak within any possible gaps between the tested masonry block and the Styrofoam layer.

The testing apparatus was first calibrated using a Styrofoam masonry unit (Figure 5.10c) with an R-value equal to 31 m^2.k/W. The results of the calibration were used to ensure that the flanking loss around the metered specimen was negligible.

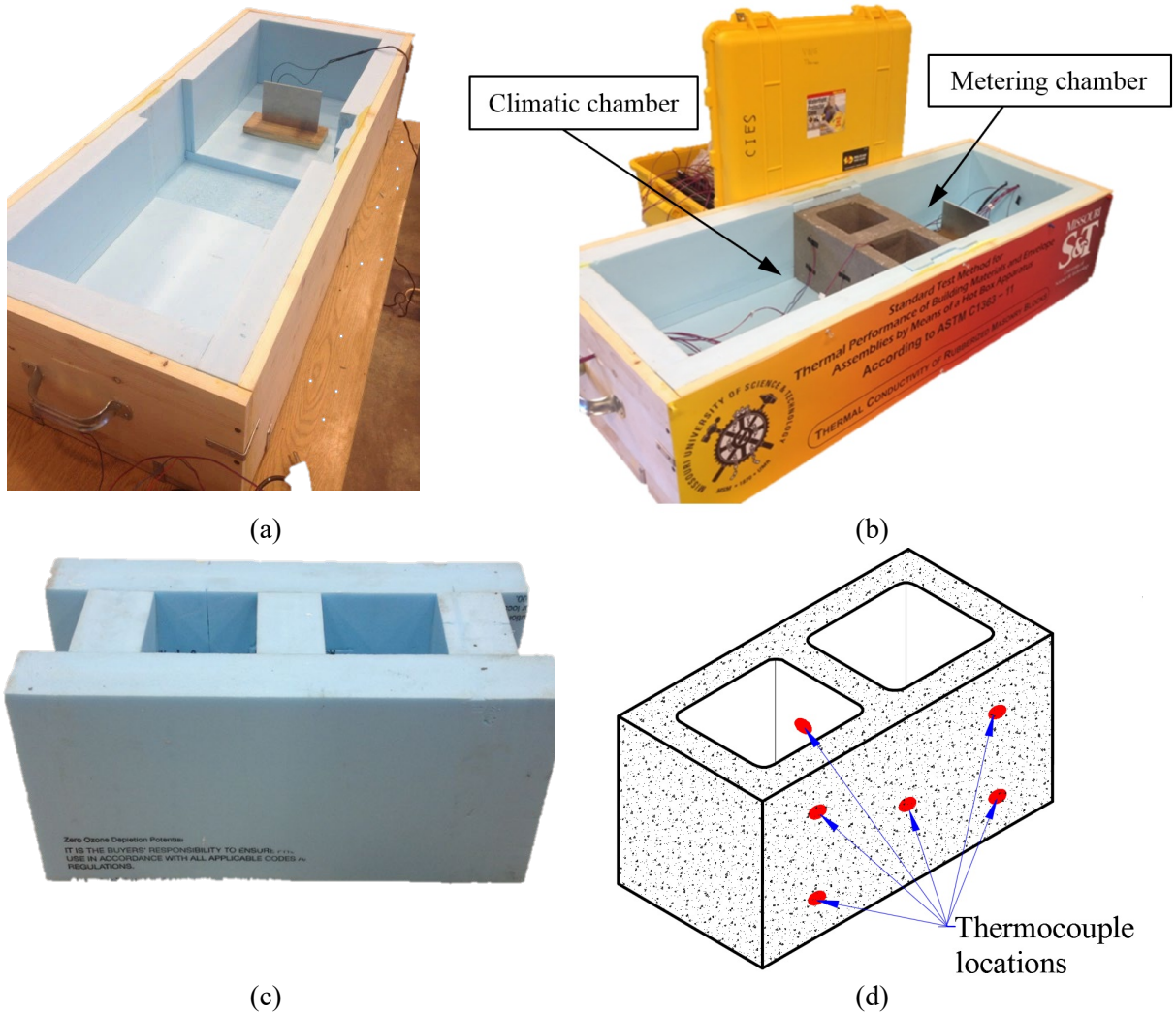

Figure 5.10: Two controlled sides apparatus: (a) The controlled heat source in the apparatus, (b) Testing specimen and data acquisition system, (c) Calibration block, and (d) Measuring the transferred heat with thermocouples.

Twenty thermocouples were used to monitor the heat transfer through each masonry block and across the two controlled rooms in the apparatus itself. The heat transfer was monitored by collecting the temperature at five separate locations on each side of the masonry unit and in the middle of the web (Figure 5.10d). As the inside of the hot box was under full monitoring for the temperature at various locations, the temperature outside the hot box was also monitored and recorded. Once a specimen is placed inside the hot box apparatus, the upper box door (that had a

50-mm thick layer of Styrofoam) was tightened and sealed to eliminate heat leaks. The heating plate was then turned on for 24 hours to get a temperature of 49.5° C ± 0.5° C measured at 25 mm from the middle of the face shell of the masonry unit at the metering chamber. The temperature data were collected at a rate of 10 readings per minute using a data acquisition system (Figure 5.10b). The time required for each specimen to reach its thermal steady state (i.e. the temperature recorded on both sides of the masonry unit remaining constant, with a variation within 5%) for each sensor was collected. This indicated the time needed for the heat to fully penetrate the materials since the material with good insulation required more time to reach the steady state. Furthermore, the differences in temperatures between both sides of the tested masonry unit at the thermal steady state were calculated for each tested specimen. These differences can be used to quantify the amount of insulation provided by the masonry unit. A significant difference between the temperatures on both sides indicated a higher capacity for transferring heat. STOPPED HERE

5.1.1.3.4. The hot box apparatus

A well-insulated thermal box was fabricated (Figure 5.11), following ASTM C1363, in order to calculate the thermal conductivity of a masonry unit at the thermal steady state that occurred after exposing a tested unit to a constant and continues heat source for 24 hours. The box was fabricated as explained in the previous section with one exception. Instead of having the masonry unit placed in the middle of the hot box, it was placed at one end of the hot box (Figure 5.11a).

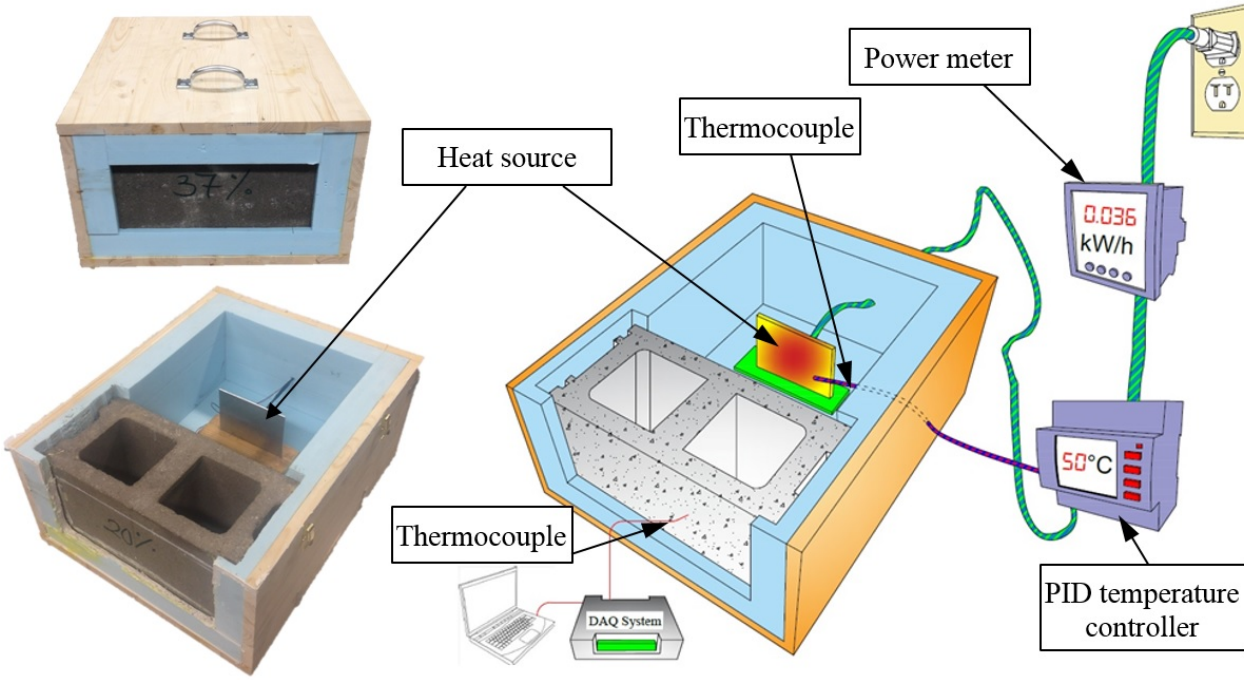

(a)

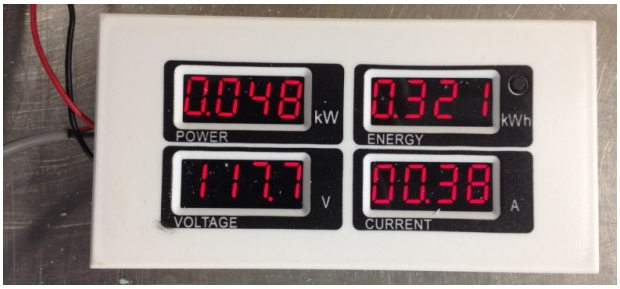

(b)

Figure 5.11: The hot box apparatus: (a) Hot box, and (b) Power monitoring meter.

These testing apparatuses simulate a well-insulated room with one exposed side, which is the test subject. Thermal images and videos (Figure 5.12) proved that there was no heat leak from the testing apparatus and the heat transferred through the tested blocks only.

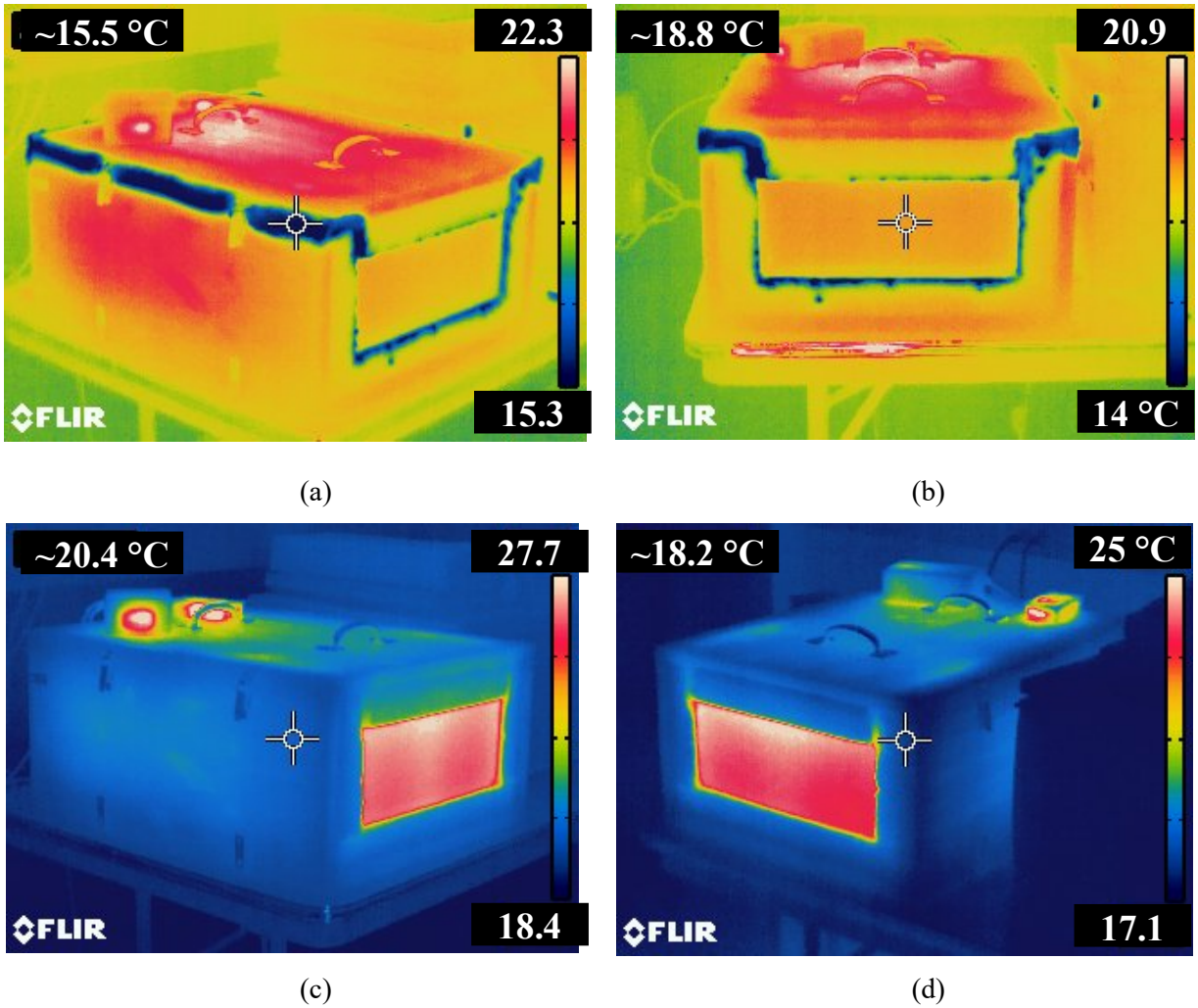

Figure 5.12: Thermal images of the guarded hot box: (a) Side view image before testing, (b) Front view image before, (c) Side view image during testing, and (d) Front view image during testing

The Styrofoam faces were engraved, and a masonry test specimen was placed in the testing apparatus with the interior side subjected to a constant temperature of 47.5±2.5° C, representing an extreme outdoor summer temperature. An aluminum plate and PID controller were used for emitting and controlling the heat, as explained earlier (Figure 5.11a). The exterior masonry

specimen face was subjected to a constant temperature of 18.5±1.5° C using the AC system simulating the temperature inside a residential building. The effect of masonry units having different rubber content were determined by measuring the consumed energy to maintain an average temperature inside the hot box apparatus at 47.5° C.

Since only one of the six sides of the testing apparatus is the tested masonry unit while the other five sides are made from plywood and Styrofoam, it was required to subtract the energy consumed by the other five walls and then determine and the energy consumption of the tested masonry unit only. This was achieved by using the Styrofoam unit (Figure 5.10c) as explained earlier. The test then was run to calculate the consumed energy by the testing apparatus itself without the masonry unit to be subtracted later from the total consumed energy by the same apparatus with the masonry unit on one side. Fourier's heat conduction equation, Equation 2, was used to compute the thermal conductivity of the tested masonry units where t_1: temperature of the face shell inside the hot box (the heated face), t_2: the temperature at the outside face (the cold face), and A: area of the tested masonry unit that faced the heat source.

A digital power meter was connected to the heating source to record the consumed energy during this test (Figure 5.11b). A data acquisition system and two thermocouples were used to monitor the temperatures inside and outside the testing apparatus (Figure 5.11a). The testing apparatus in the procedure described above were calibrated using six different materials having well known thermal conductivity (Figure 5.13).

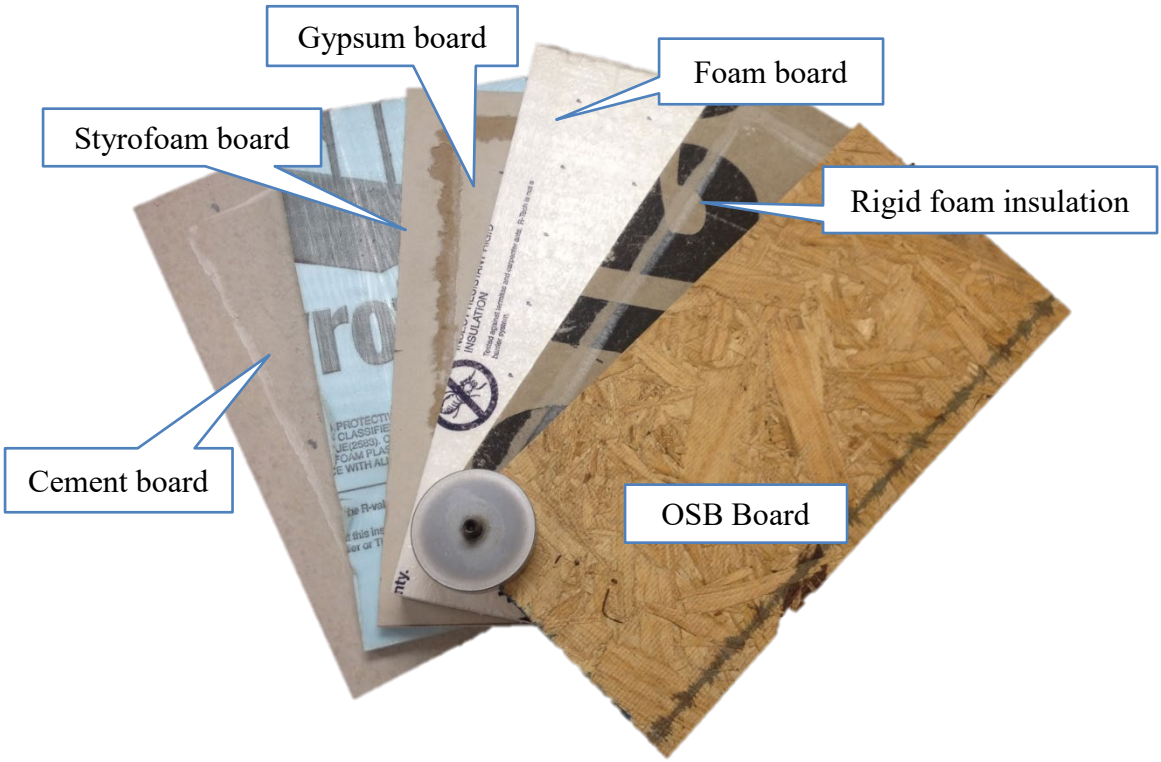

Figure 5.13: The materials used for calibration.

5.1.2. Results and discussion

In general, rubberized masonry units displayed higher thermal insulation, which was measured using four different approaches. While the general trend was similar for all methods, the measured insulation improvement was a function of the method of measurement. The hot box and the two controlled sides guarded hot box methods measure the thermal insulation of a masonry unit (as a structure), while the thermal probe and guarded hot plate assembly methods measure the thermal insulation at the material level through examining either a plate of material or inserting the thermal probe in various locations within the masonry unit.

5.1.2.1. Thermal needle probe method

The relationship between the rubber replacement ratio and the thermal conductivity factor was approximately linear and consistent (Figure 5.14). Replacing 5%, 10%, and 15% of the mineral aggregate with crumb rubber reduced the thermal conductivity factor by 7%, 12%, and 17% from 2.04 W/m.K to 1.9, 1.8, and 1.7 W/m.K. In addition, the results of lightweight of concrete masonry unit (LWCMU) are shown in the figure for comparison. As shown in the figure, the thermal conductivity of the LWCMUs is 60% of that of the CMU.

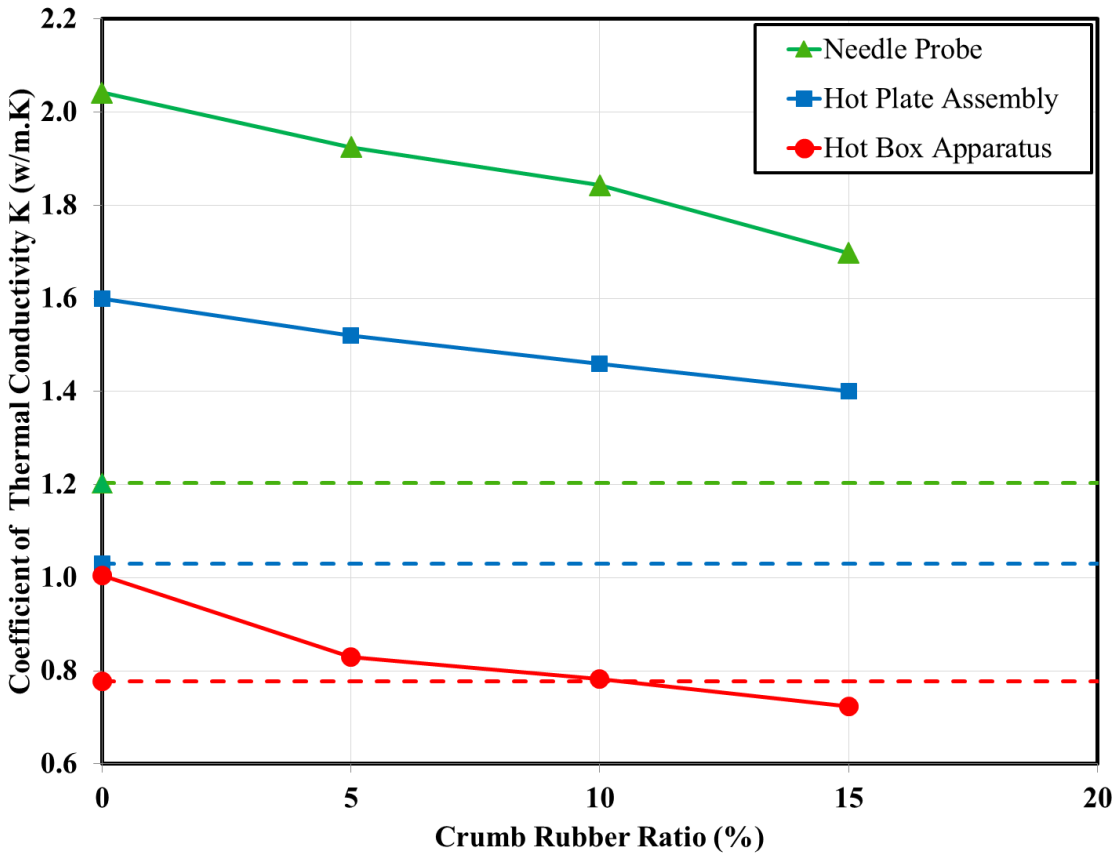

Figure 5.14: Thermal conductivity factor for RCMUs (solid lines) and LWCMUs (dotted lines) using different approaches.

5.1.2.2. Guarded hot plate assembly method

Figure 5.14 shows the thermal conductivity measured on masonry plate specimens. Replacing 5%, 10%, and 15% of the mineral aggregate with crumb rubber reduced the thermal conductivity factor by 5.0%, 8.7% and 12.5% from 1.6 W/m.K to 1.52, 1.46, and 1.4 W/m.K, respectively. As shown in the figure, the thermal conductivity of the LWCMUs is 60% of that of the CMU. These results are similar to those obtained using the thermal needle probe procedure, as both methods deal with thermal conductivity at the material level, not the masonry unit. It is of interest that the thermal conductivity values measured using the needle probe method are 20% to 25% higher than those obtained using the guarded hot plate assembly method. This difference is attributed to the difference in the specimen exposure, as the specimen in the needle probe procedure is fully exposed to the ambient temperature which helps to dissipate the heat more easily than in the guarded hot plate assembly where the specimen is fully insulated.

5.1.2.3. Two Controlled sides guarded hot box method

This test quantified the thermal effects of rubber content using two different measures, namely difference in temperature and time to reach a steady state. The heat flow through a tested masonry unit became steady after 24 hours. The difference between the temperatures on both sides of the apparatus (ΔT) was measured for each test specimen as an indication of the thermal insulation (Figure 5.15). The higher content of rubber led to a higher ΔT. RCMU with a 15% rubber ratio had a ΔT of 17.3° C after 24 hours, while the unit with 0% rubber had a ΔT of 14.0° C.

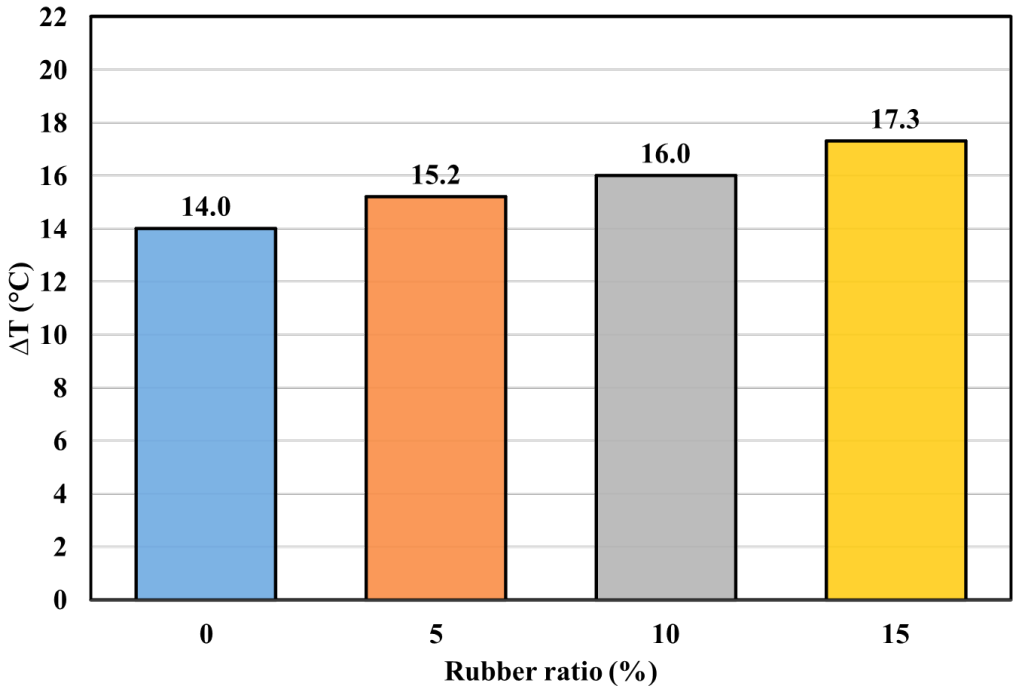

Figure 5.15: ΔT between the inner and outer faces of blocks at the steady-state case.

Another measure for the thermal efficiency of RCMUs was noticed through monitoring the rate of increase of the interior temperature (Figure 5.16). The interior temperature recorded for units with 0% of rubber reached a steady state faster than the units with rubber. Units with 15% rubber took 6.5 hours to reach the steady state, compared to 5.5 hours for the conventional CMU. This proved that rubberized units do not lose heat as quickly as a conventional CMU due to the relatively low thermal conductivity of the rubberized blocks.

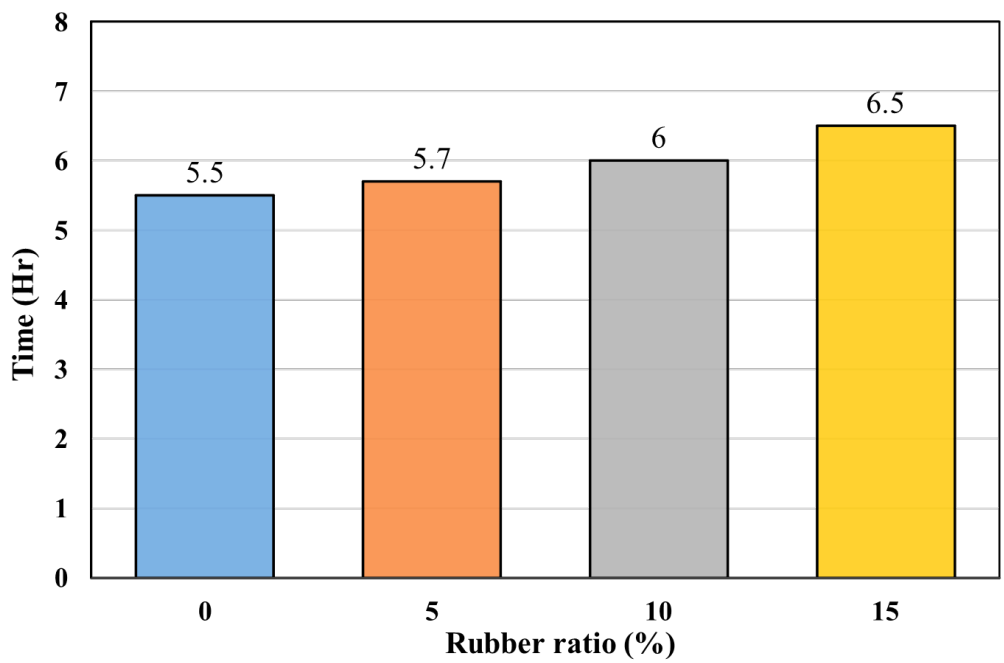

Figure 5.16: Time to reach steady state.

5.1.2.4. The hot box apparatus method

Before running the test, the hot box apparatus was calibrated by using it to compute the thermal conductivity of well-known thermal materials (Figure 5.13). The second-degree approach (Equation 3) was able to predict the manufacturer-provided thermal conductivity with an R^2 value of 0.971.

$$K_{actual} = -0.1269\left(K_{exp}\right)^2 + 2.0155\ K_{exp} - \ 0.1584 \qquad (5.6)$$

Where:

K_{actual} = the actual thermal conductivity (W/m.K).

K_{exp} = the calculated thermal conductivity using the hot box apparatus method (W/m.K).

The impact of crumb rubber on the coefficient of thermal conductivity is shown in Figure 5.14. Replacing 5%, 10%, and 15% of the mineral aggregate with crumb rubber reduced the thermal conductivity factor by 17%, 22%, and 28% from 1.0 W/m.K to 0.83, 0.78, and 0.72 W/m.K, respectively. These values are smaller than those obtained using the needle probe and guarded hot plate assembly. Both the needle probe and guarded hot plate assembly measure the thermal conductivity at the material level, which is different from the hot box apparatus where the thermal conductivity is measured at the block level. Therefore, the shape of the block including thermal bridging and empty cells with low thermal conductivity plays an essential role in determining the thermal conductivity using the hot box apparatus. Furthermore, the relationship of the crumb rubber to the reduction of thermal conductivity at the material level was linear. However, a large drop was noticed in the thermal conductivity factor when 10% rubber was used. The reason behind that was the significant difference between the thermal conductivity of concrete and rubber. The average thermal conductivity of masonry material at the ambient temperature was 8.4 times that of the rubber, i.e., 1.01 (W/m.K) for masonry (Figure 5.14) and 0.12 (W/m.K) for rubber. The specific heat for masonry material was also 0.47 times that of the rubber, i.e., 950 J/kg.K for masonry and 2010 J/kg.K for rubber. Therefore, the thermal diffusivity of masonry is about 5.6 times that of rubber. The thermal diffusivity, calculated as the thermal conductivity divided by the density and specific heat capacity, measures the rate of transfer of heat of material from the hot side to the cold side. Using a small amount of rubber content will cause a significant drop in the thermal diffusivity of rubberized masonry units. The thermal conductivity of LWCMU measured using the hot box apparatus is also presented in Figure 5.14. As shown in the figure, the thermal conductivity of the LWCMU was equivalent to RCMU having 12% rubber content.

Another measure of the thermal efficiency of RCMUs is the amount of energy consumed to maintain an average temperature inside the testing apparatus at 50° C for 24 hours with an average

outside temperature of 18.5° C. This energy was computed for each RMCU and compared with that of the conventional CMU and LWCMU (Figure 5.17). Reductions of 18%, 26%, and 29% were achieved for RCMUs with 5%, 10%, and 15% rubber content ratios, respectively, while using the LWCMU cut the energy consumption by only 28%.

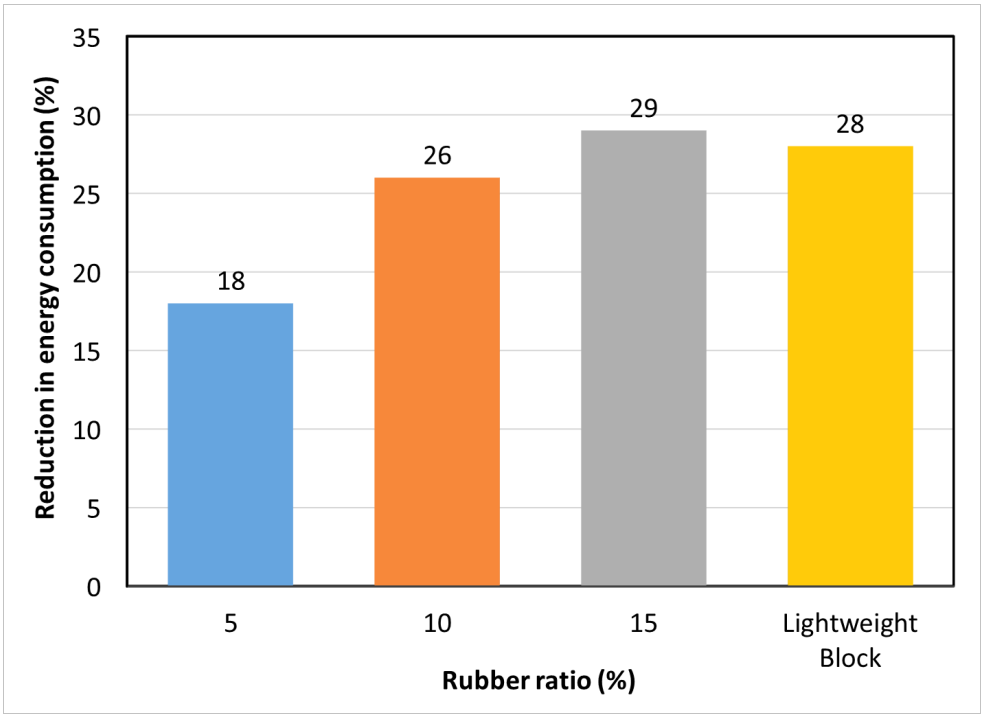

Figure 5.17: Reduction in energy consumption for rubberized and lightweight masonry units.

5.2. Thermal and acoustic retrofitting of CMU using eco-friendly rubberized plastering

5.2.1. Material properties

The waste of the scrap tires' processing was collected in the form of rubber dust with fibers from a scrap tire processing factory in Macon, Missouri, USA. The rubber dust was sieved to remove any unwanted particles and to split it into different grades based on the size. Two grades of recycled rubber were used during this study. The first grade was a recycled rubber with particles passing sieve No. 50 and retained on sieve No. 100, which leads to a particle size between 0.297 and 0.149 mm. Based on the size, this grade was used as a replacement of fine aggregate. The second grade was for recycled rubber particles passing sieve No. 200, which leads to a particle size smaller than 0.074 mm (74 µm). Based on the size, this grade was used as a replacement for cement powder. Figure 5.18 shows the particle size distribution of both sizes of recycled rubber in addition to cement using the laser diffraction analyzer.

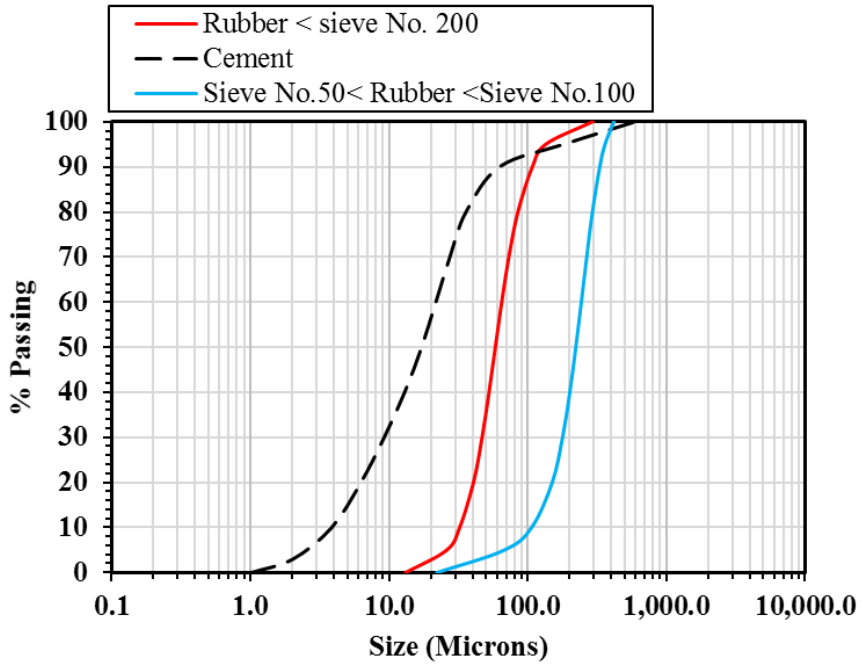

Figure 5.18: Sieve analysis of the two grades of rubber and cement.

A scanning electron microscope (SEM) was used to explore the shape and the element analysis of the two grades of recycled rubber. As shown in Figure 5.19, the rubber particles have a rough and irregular shape for both grades. In addition, pieces of fiber were accompanied with the rubber particles. The element analysis of the fiber (Figure 5.19b) shows that the major component of these fibers is carbon followed by oxygen with a very small amount of silicon which refers to a cellulosic fiber. Well-graded river sand passed through a No. 4 (4.75 mm) sieve was used in this study.

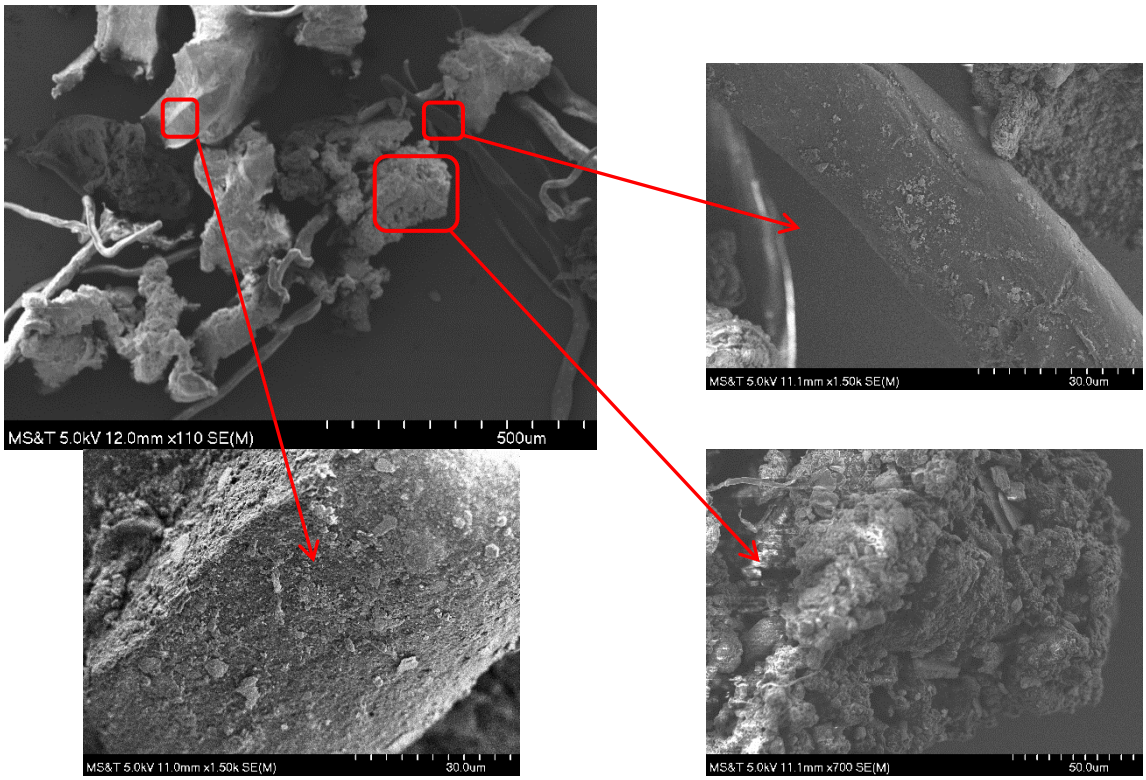

(a)

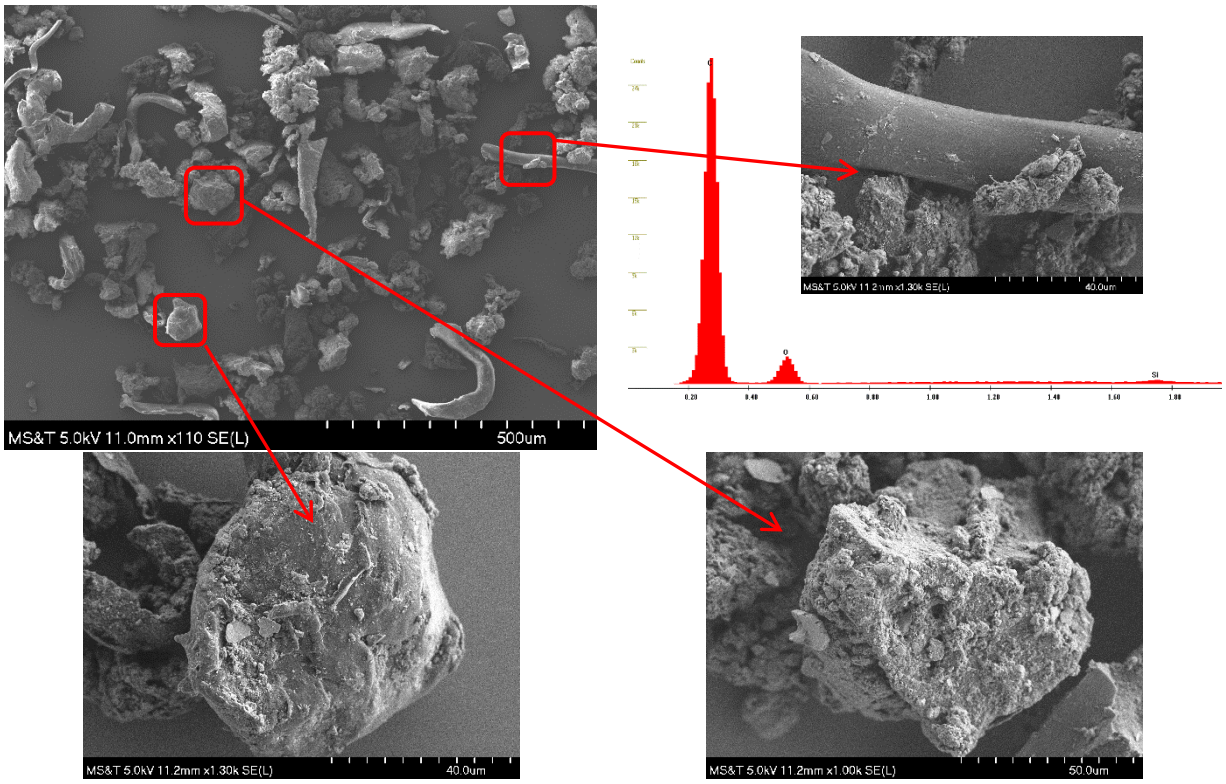

(b)

Figure 5.19: SEM analysis of the two grades of rubber: (a) rubber < sieve No. 200, and (b) rubber between sieves No. 50 and 100.

5.2.2. Experimental program

Two sets of cement mortar mixtures with varied rubber ratios were prepared (Table 5.1). Rubber powder with particles passing sieve No. 200 (74 µm) was used in the first set as a replacement for the cement with volume replacement ratios of 0, 10, 20, 30, and 40%. In the second set, rubber powder with particles passing sieve No. 50 (297 µm) and retaining on sieve No. 100 (149 µm) was used as a replacement for the fine aggregate with volume replacement ratios of 0, 10, 20, 30, and 40%.

Table 5.1: Mix Proportions for Cement Mortar Mixes with Cement or Fine Aggregate Replacement by Recycled Rubber Powder

	Mix ID	Cement		Fine aggregate		Rubber		Total volume	Water	W/C ratio
		Weight (kg)	*Volume (cm^3)*	*Weight (kg)*	*Volume (cm^3)*	*Weight (kg)*	*Volume (cm^3)*	*(cm^3)*	*Volume (liter)*	
	0% R	6.80	2152	20.4	7701	0.00	0.00	9852	2.90	0.43
Set 1	10%R200	6.12	1937	20.4	7701	0.21	217	9852	2.89	0.47
	20%R200	5.44	1722	20.4	7701	0.42	434	9852	2.95	0.54
	30%R200	4.76	1506	20.4	7701	0.62	641	9852	2.95	0.62
	40%R200	4.08	1291	20.4	7701	0.83	857	9852	2.95	0.72
Set 2	10%R50	6.80	2152	18.4	6926	0.75	775	9852	3.27	0.48
	20%R50	6.80	2152	16.3	6161	1.49	1539	9852	3.67	0.54
	30%R50	6.80	2152	14.3	5386	2.24	2314	9852	3.99	0.59
	40%R50	6.80	2152	12.2	4611	2.99	3089	9852	4.60	0.72

5.2.2.1. Mechanical properties of rubberized mortar

5.2.2.1.1. Density, water absorption, and air voids

Concrete cylinders, 100×200 mm, out of each mixture were used to measure the density and voids in hardened mortar according to the ASTM C642-13 method which can be used to deduce the permeability of concrete and yield results similar to that of the vacuum saturation method; however, the former approach is more versatile. The test procedure can be summarized as follows: the oven-dried masses of all specimens were determined followed by saturating them in water and determine their surface-dry masses after immersion for not less than 48 hrs. After boiling

the specimens in water for 5 hours, the soaked, boiled, and surface-dried masses were determined. Finally, after suspending the specimens in water, the apparent masses in water after immersion and boiling were determined. Based on the results from this procedure, the following characteristics can be calculated:

Absorption after immersion, % = $[(B - A)/A] \times 100$ (5.6)

Absorption after immersion and boiling, % = $[(C - A)/A] \times 100$ (5.7)

Bulk density, dry = $[A/(C - D)].\rho = g_1$ (5.8)

Bulk density after immersion =$[B/(C - D)].\rho$ (5.9)

Bulk density after immersion and boiling = $[C/(C - D)].\rho$ (5.10)

Apparent density = $[A/(A - D)].\rho = g_2$ (5.11)

Volume of permeable pore space (voids), % = $(g_1 - g_2)/g_2 \times 100$ (5.12)

Where: A = mass of oven-dried sample in air, B = mass of surface-dry sample in the air after immersion, C = mass of surface-dry sample in the air after immersion and boiling, D = apparent mass of sample in water after immersion and boiling, g_1 = dry bulk density, g_2= apparent density, and ρ = density of water.

5.2.2.1.2. Compressive strength

Three 50 mm mortar cubes were prepared and tested for each mixture. The compressive strength test was performed according to ASTM C109-16a at the ages of 28 and 56 days. For a given mixture, the testing result of any specimen with a range of 8.7% or more from the average of the results of the three cubes of that mixture were excluded from the average.

5.2.2.1.3. Flexural strength and toughness

The modulus of rupture, at the ages of 28 and 56 days, of each mixture, was determined using a three-point bending test (Figure 5.20) carried out on three 40×40×160 mm prisms constructed out of that mixture, per ASTM C348–14. After discarding the strength values that differed by more

than 10% from the average value of all test specimens for a given mixture, the flexural strength was calculated in MPa as follows:

$$S_f = 0.0028\,P, \tag{5.13}$$

where

S_f= flexural strength, MPa, and

P = total maximum load, N.

In addition to the modulus of rupture, the modulus of toughness was measured. The toughness of a material is its ability to absorb energy within the plastic region without rupture, and it represents the balance between the strength and the ductility. For the behavior shown in Figure 20b, the toughness is calculated as the area under the curve. The toughness factor, T.F., was taken as equal to the toughness of the rubberized beam to the toughness of the reference beam. The toughness was then calculated as the area under the load-deflection curve.

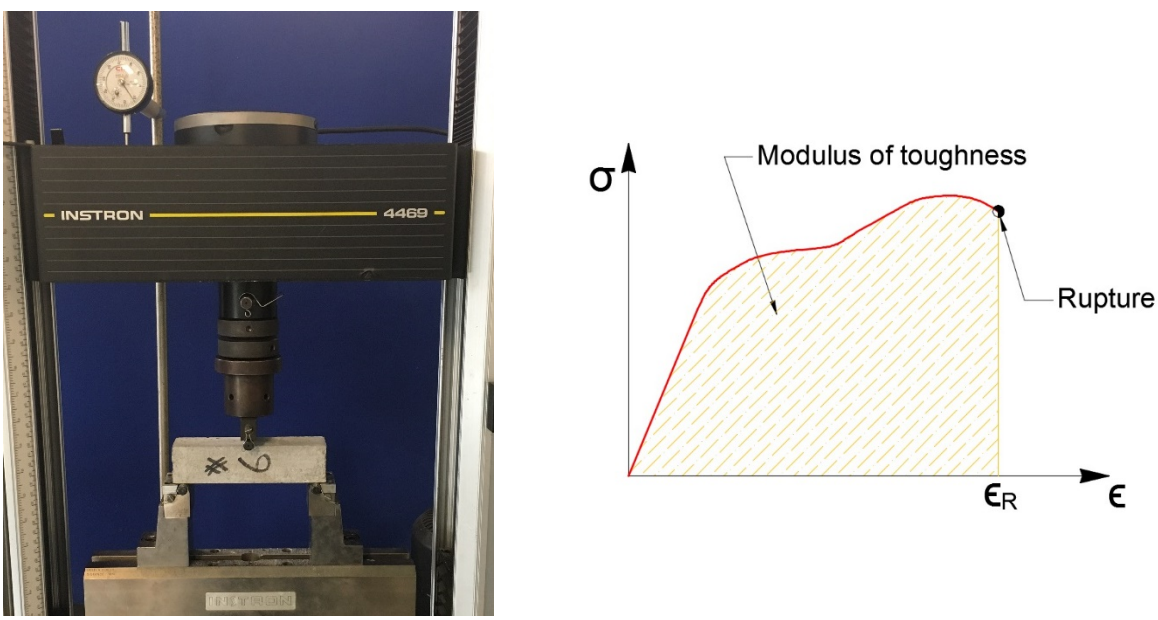

Figure 5.20: Flexural strength and toughness: (a) Flexural strength test setup, and (b) Modulus of toughness calculation.

In addition, the brittleness of the new rubberized mortar could be represented by the brittleness coefficient which is defined as the ratio of the compressive strength to the flexural strength.

5.2.2.1.4. Tensile strength and strain energy

Three 3-inch length dog-bone-shaped cement mortar specimens (Figure 5.21a) were cast for each rubber replacement ratio. Special clips were used to hold the specimens to the tensile strength testing machine (Figure 5.21b). The test was performed according to ASTM C307 with a loading speed of 6 mm/min. As shown in Figure 5.21c, a two-inch digital extensometer was mounted at the middle of the specimens to measure the axial elongation within the test specimens. Based on the displacement readings from the digital extensometer, the strain and later the modulus of resilience were calculated from the strain-stress curve. The modulus of resilience is defined as the maximum energy that can be absorbed per unit volume without creating a permanent distortion. It can be calculated by integrating the stress-strain curve from zero to the elastic limit (Figure 5.21d).

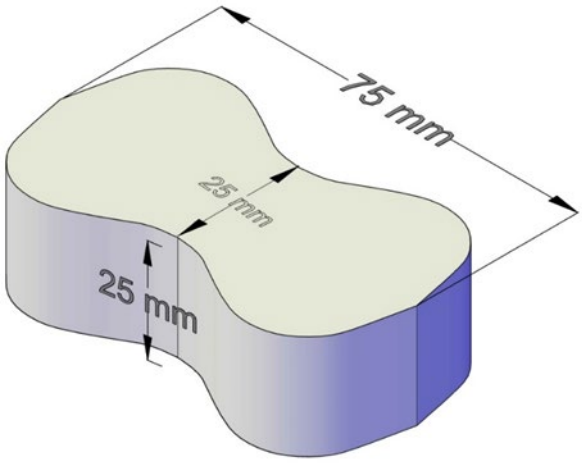

(a)

(b)

(c)

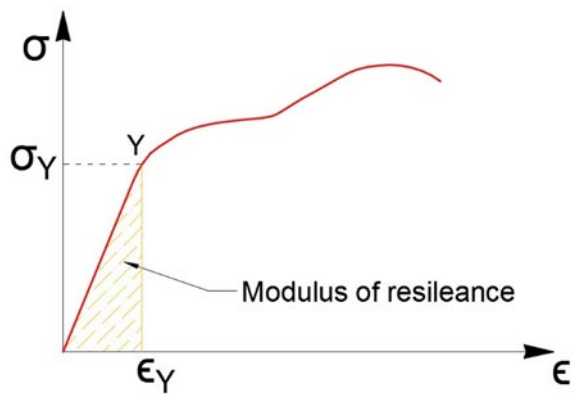

(d)

Figure 5.21: Tensile strength and resilience: (a) Test specimen, (b) Test setup, (c) Digital extensometer for strain measurement, and (d) Modulus of resilience calculation.

5.2.2.2. Thermal characterization of rubberized cement mortar at different temperatures

Three thicknesses of rubberized mortar with cement or sand replaced with five different ratios of rubber-fiber powder of 0, 10, 20, 30, and 40% were used as a plastering layer on conventional concrete masonry units (Figure 5.22). The thermal conductivity of the new proposed plastering materials was measured according to ASTM D5334-14, while the thermal conductivity of the plastered masonry units was examined according to ASTM C1363−11 in order to determine the steady-state thermal performance of construction units exposed to a constant heat source.

Figure 5.22: Different thicknesses of rubberized mortar plaster with five different ratios of RFP.

5.2.2.2.1. Thermal needle probe method for plastering materials

This test was performed according to ASTM D5334-14 using a transient heat method. This test measures the thermal conductivity using a metal probe that contains both a heating source element and temperature-measuring element. By inserting the probe in the sample, the heating element raises the temperature with time, and the temperature measuring element records the change over a period of time. The temperature decay with time after the cessation of heating was recorded to be included in the calculations to minimize the effects of temperature drift during measurement. The thermal conductivity was calculated after two heating and cooling cycles. All the measurements and the analysis were performed using a fully portable field and lab thermal properties analyzer (Figure 5.23). The analyzer uses the transient line heat source method to measure thermal conductivity, resistivity, diffusivity, and specific heat. This test was originally designed to determine the thermal conductivity of soil and soft rock by inserting the thermal needle probe in the soft material using hand pressure without creating a prior hole. Since it is impossible to insert the thermal needle probe in hard materials such as concrete or mortar using hand pressure, a modified method that uses the same technology as in ASTM D5334-14 was used. The modification came from using a 4 mm rotary hammer drill bit to create a properly sized pilot hole. Thermal grease was then squeezed up around the thermal probe (Figure 23b) before inserting the probe in the hole to ensure full contact between the thermal needle probe and the tested material. Using thermal grease eliminates any air gaps between the concrete and the probe surface due to the drilling action.

To examine the thermal performance of the newly proposed rubberized mortar under different temperatures, which simulate different seasons, the thermal needle probe test was performed at temperatures of 22° C and -10° C.

(a) (b)

Figure 5.23: Thermal needle probe test: (a) Testing mortar specimen with KD2 PRO portable thermal properties analyzer, and (b) Thermal needle probe with and without thermal grease.

5.2.2.2.2. The guarded hot box method

A guarded hot box, in section 5.1.1.3.4, was used in accordance with ASTM C1363−11 in order to determine the steady-state thermal performance of building units exposed to a constant heat source. The tested plastered masonry unit was located on one of the six sides of the guarded hot box. This test represented a close simulation of the thermal insulation of a building. The heat source was kept inside the box to keep the temperature between 48° C and 52° C, which represented very hot weather during the summer season. The temperature outside the box was kept between 18° C and 20° C using the lab AC system to represent the semi-cool temperature inside a building. This test system shows the amount of the saved energy by comparing the power consumption required to keep the temperature between 45° C and 55° C using masonry block with a plastering mortar layer with varied RFP content. The energy consumptions were then calculated for masonry units with rubberized plastering and compared with the conventional masonry unit. The Fourier

heat conduction equation (Eq.14) was used to calculate the thermal conductivity for each type of masonry block. The heat flow at steady state was assumed to be the same as the rate of heat output from the heat source. It was computed as 3.41 times the rate of the inputted electrical energy to the heat source. A sensitive meter was used to monitor and record the energy consumption during each test to obtain the most accurate measurement of electrical energy consumption. The inside and outside temperature data were collected using two thermocouple wires that connected to a computerized data acquisition system. During the test, the guarded hot box was checked for heat leaking using a sensitive thermal camera.

The net exposed area of the tested masonry unit was calculated. The thermal conductivity factor was calculated using the measured heat flow and temperatures on both sides of the masonry as follows:

$$k = \left(-\frac{qL}{A(t_1 - t_2)} \right) \tag{5.14}$$

Heat resistivity was then calculated as follows:

$$r = \frac{L}{k} \tag{5.10}$$

where:

k: thermal conductivity factor, (W/m K).

r: heat resistivity, (m2 K /W).

L: thickness of the tested specimen, (m).

A: area of the tested specimen, (m2).

t1: the temperature of hot plate face in contact with the specimen, K.

t2: the temperature at the heat collecting plate on the top face of the sample, K.

q: heat flow rate within the tested specimen, W/m2. (q = 3.41 times the rate of electrical energy input to the hot plate, Watts).

5.2.2.3. Acoustic characterization of rubberized cement mortar

5.2.2.3.1. Sound absorption

The ability of a material to absorb sound can be measured using the sound absorption coefficient (α). According to ASTM E1050−12, the Acoustical Properties of Materials and Systems (ACUPRO) was used to measure both absorption coefficient under varied frequencies and noise reduction coefficient. The plane wave tube was carefully machined using stainless steel tube with a wall thickness of 3.2 mm for an accurate measurement of sound pressure amplitude and phase (Figure 5.24a). The phase response of the tube is less than 0.1 degrees over the operating range from 50-5650 Hz. The precision machined flanges, side ports, and microphone holders accurately maintain microphone alignment. A 16-ohm high-frequency compression JBL compression driver was used to produce sound (Figure 5.24b). Two 13 mm high accuracy microphones were used with microphone holders to ensure stable posting of the testing apparatus (Figure 5.24c). A fully integrated ACUPRO Software and DT 9837A data acquisition module was used to collect and analyze the output data from the testing apparatus (Figure 5.24d).

Since the sound absorption of materials is varied under different frequency ranges, it required the use of a single value that evaluates the sound absorption of the particular material. To solve this problem, the noise reduction coefficient (NRC) was calculated for each masonry material with different rubber ratio using Eq. 15. The NRC can be calculated using the following equation (Thumann and Miller 1986, Sukontasukkul 2009):

$$NRC = (\alpha_{250} + \alpha_{500} + \alpha_{1000} + \alpha_{2000})/4 \tag{5.15}$$

Where $\alpha 250$, $\alpha 500$, $\alpha 1000$, $\alpha 2000$ are the sound absorption coefficients (α) at 250, 500, 1000, and 2000 Hz, respectively.

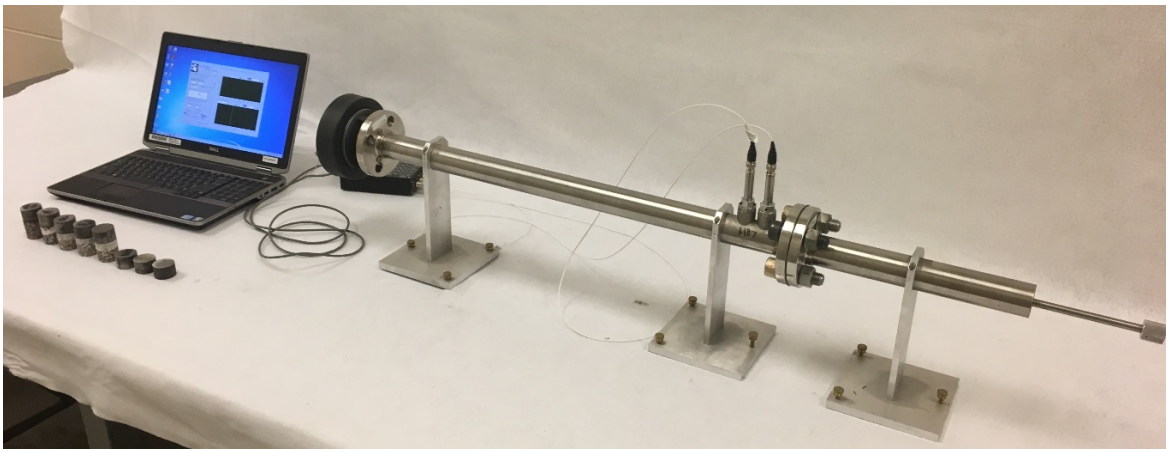

(a)

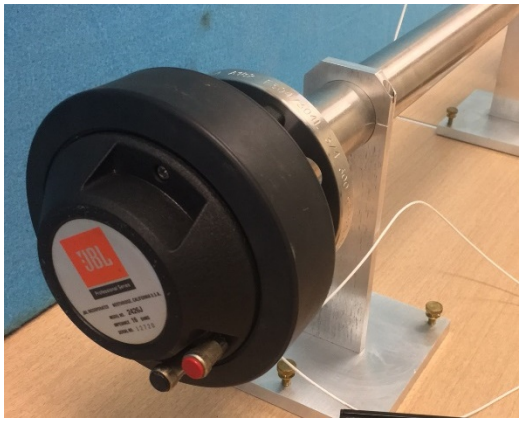

(b)

(c)

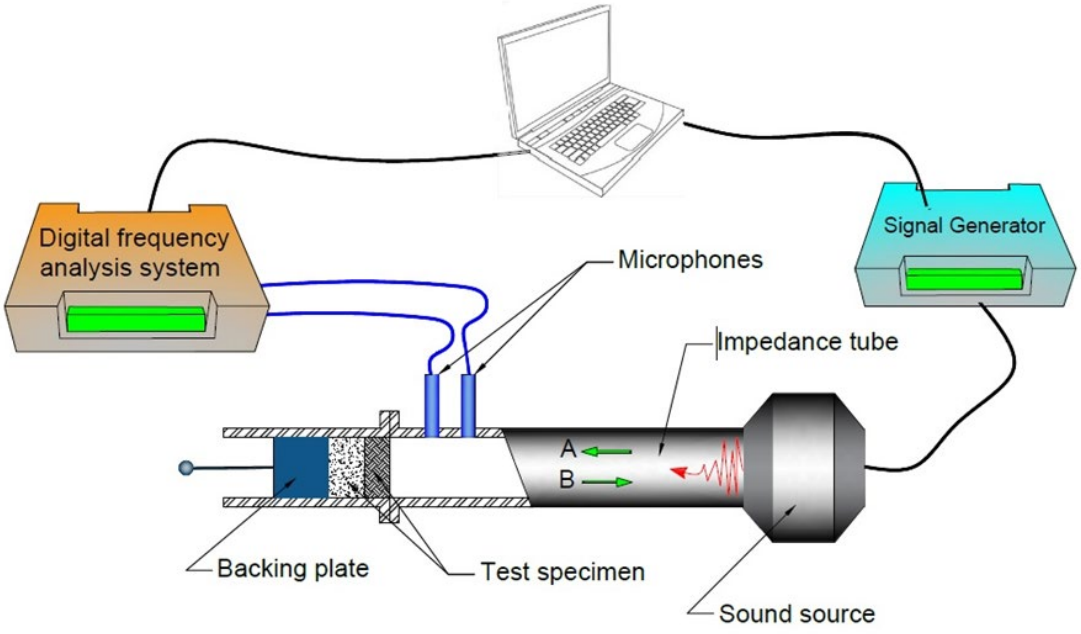

(d)

Figure 5.24: Acoustic absorption test: (a) Testing apparatus, (b) Sound source (compression driver), (c) Microphones with holders, and (d) ACUPRO Software with data acquisition module.

5.2.2.3.2. Sound transmission

In addition to sound absorption, sound transmission and later transmission loss of retrofitted masonry materials can be measured. This test is similar to the sound absorption test method (ASTM E1050-12) in that it also uses a tube with a sound source connected to one end and the test sample mounted in the tube. However, for sound transmission, four microphones were used instead of two, at two locations on each side of the sample. Plane waves were generated in the testing tube using a broadband signal from a noise source. The resulting standing wave pattern is decomposed into forward- and backward-traveling components by measuring sound pressure simultaneously at the four locations and examining their relative amplitude and phase. The acoustic transfer matrix is calculated from the pressure and particle velocity, or equivalently, the acoustic impedance, of the traveling waves on either side of the specimen. Finally, a fully integrated ACUPRO software and DT 9837A data acquisition module was used to collect and analyze the output data from the testing apparatus (Figure 5.25).

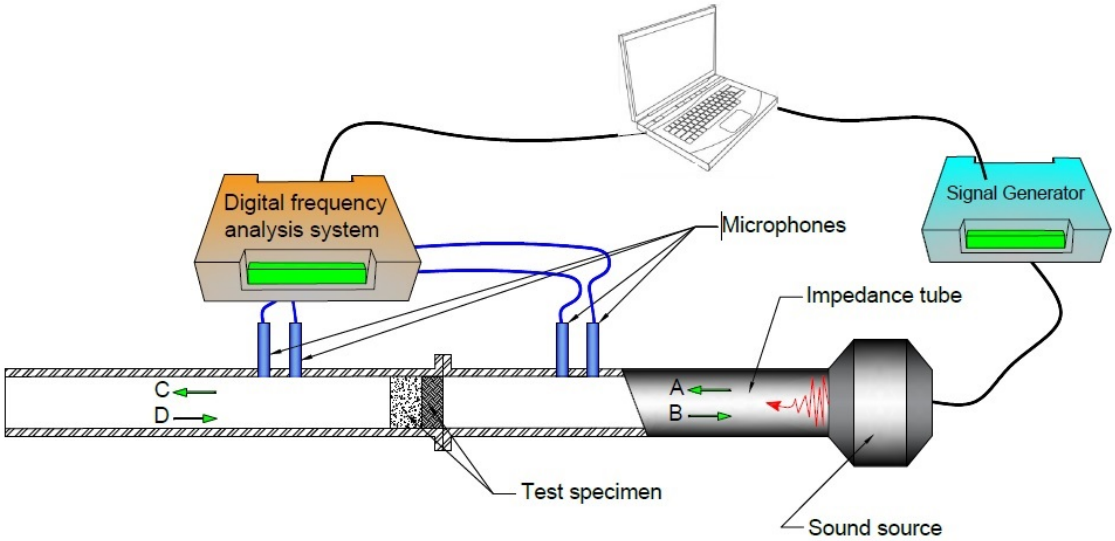

Figure 5.25: Sound transmission testing apparatus.

The tested specimens were prepared by using a high precision water jet cutter (Figure 5.26a) to cut masonry specimens that fit tightly inside the ACUPRO testing system (Figure 5.26b).

(a)

(b)

Figure 5.26: Preparing specimens for acoustic tests: (a) Using a water jet cutter to cut masonry specimens, and (b) Masonry specimen to be used in ACUPRO testing system.

5.2.3. Results and discussion

5.2.3.1. Mechanical properties

5.2.3.1.1. Density, water absorption, and air voids

Figure 5.27 shows the influence of using varied RFP ratios and sizes on each of the apparent and bulk dry densities. Adding RFP with a size smaller than 75 µm (R200) up to 20%, decreased the apparent and bulk densities. Replacing 20% of cement with RFP decreased both apparent and bulk dry densities by 17 and 12%, respectively. However, using RFP with a size between 150 and 300 µm (R50) as a sand replacement was more influential on both densities, and it continued up to 40% replacement of sand. Replacing 20% of the sand with RFP decreased both apparent and bulk dry densities by 23 and 20%, respectively. Although a lower bulk density was anticipated after increasing the RFP content, due to the relatively low density of RFP compared to sand or cement, adding RFP beyond a certain amount did not change the density. This was due to the change in mortar packing density, which led to a more condensed mixture. However, there was no consistent trend since the w/c ratio was changed when adding the RFP as a cement or sand replacement. The strong influence of the RFP with particle sizes between 150 and 300 µm (R50) on the density, compared to RFP with particle sizes smaller than 75 µm (R200), is attributed to the total ratio of RFP within the mortar matrix since the sand represents 78% of the volume reference mortar matrix, compared to 22% for the cement. For example, replacing 20% of the cement with RFP (R200) leading to a total RFP within the mortar matrix of 4.4% compared to 15.6% when 20% of the sand was replaced with RFP (R50).

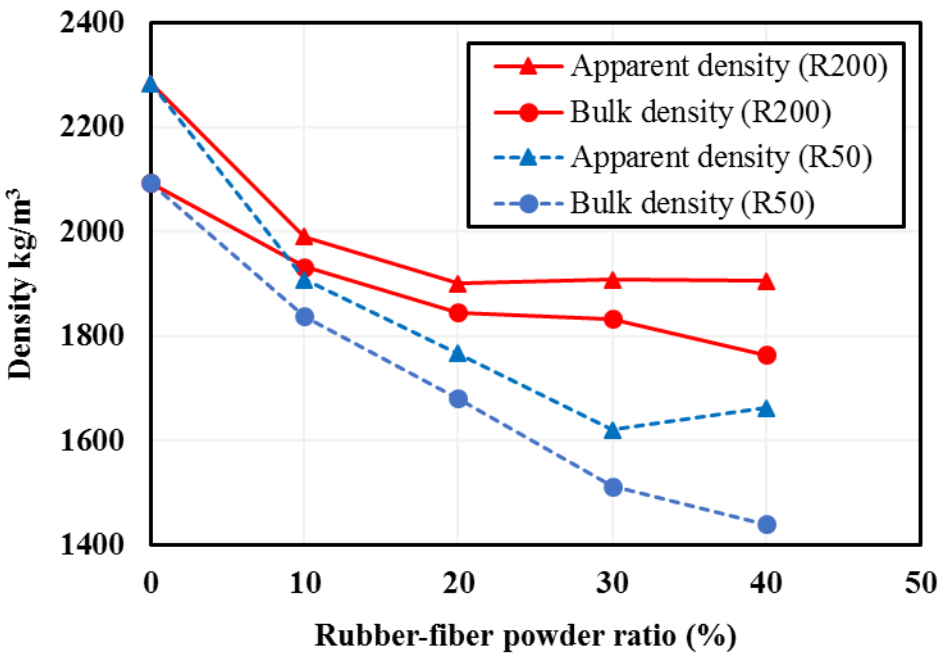

Figure 5.27: Apparent and bulk densities of rubberized plastering mortar with varied sizes and ratios of rubber-fiber powder.

5.2.3.1.2. Compressive strength

Figure 5.28 shows the compressive strength at 28 days for the different mortar mixtures with error bars that represent the statistical range of the results. A systematic reduction in the compressive strength was recorded when increasing the RFP replacement ratio. This reduction was expected as a result of replacing a portion of the cementitious material with a non-reactive material in the case of replacing cement or replacing sand with low stiffness material. Figure 5.28 shows that, per ASTM C270−14a, replacing up to 30% of the cement with RFP maintains a class M designation, which requires that the highest grade of mortar have minimum compressive strength of 17.2 MPa at the age of 28 days. In the case of replacing the sand, class M mortar designation was maintained when replacing up to 25% of sand with RFP.

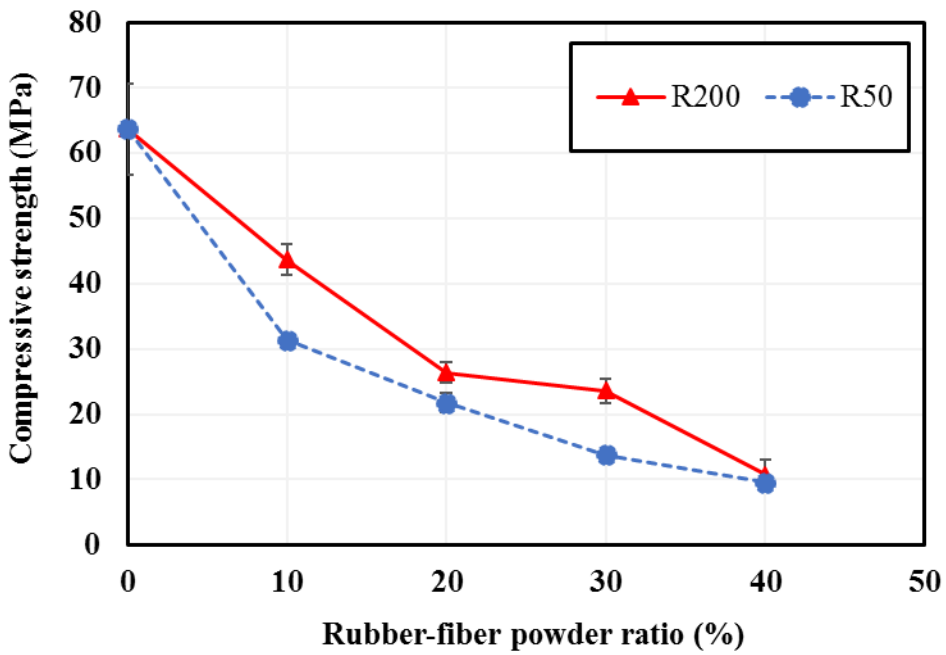

Figure 5.28: Compressive strength of rubberized plastering mortar with varied sizes and ratios of rubber-fiber powder.

5.2.3.1.3. Flexural and tensile strength

Figure 5.29 shows the modulus of rupture (MOR) of the rubberized mortar prisms with varied RFP replacement ratios. The test was performed on three prisms for each RFP replacement ratio at the age of 28 days. A systematic reduction in flexural strength was noticed in both cases of replacing cement or sand with up to 40% RFP.

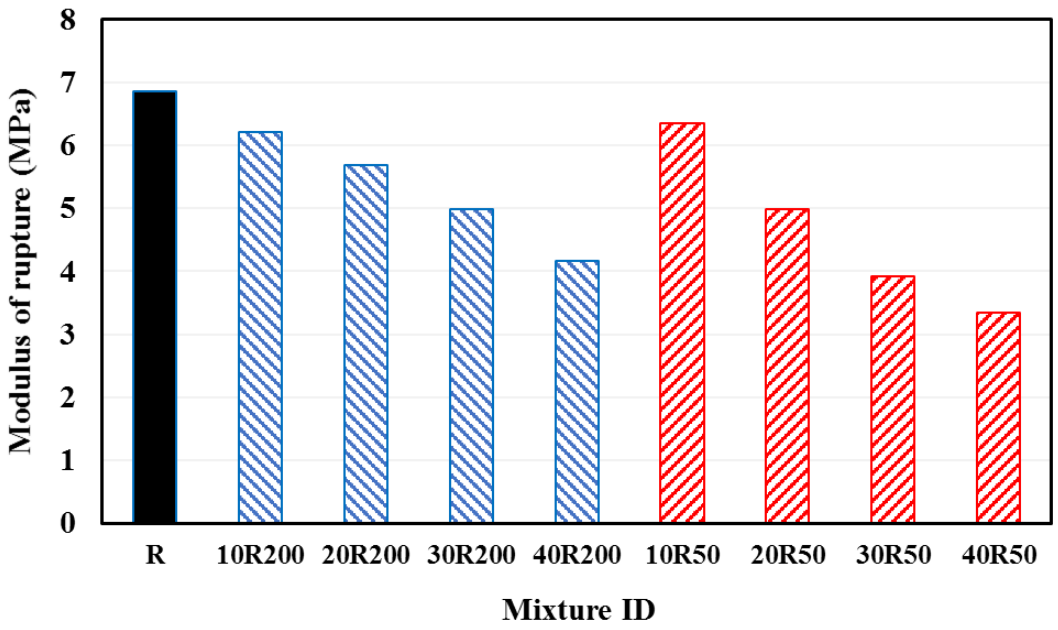

Figure 5.29: Flexural strength of rubberized plastering mortar with varied sizes and ratios of rubber-fiber powder.

Regarding the tensile strength, the results of the direct tensile strength of dog bone shape mortar specimens with varied RFP sizes and replacement ratios are presented in Figure 5.30. As shown in Figure 5.30a, increasing the amount of RFP replacement in the mortar decreased the tensile strength with a relatively higher reduction when cement was replaced, compared to the case of replacing sand with RFP. For example, replacing 20% of cement with RFP decreased the tensile strength from 3.80 to 2.76 MPa, which represents a reduction of 27%, while replacing 20% of sand with RFP resulted in a reduction of 21%. However, increasing the RFP content increased the ultimate strain of rubberized mortar (Figure 5.30b). Mixtures with 40% RFP had an increase in the ultimate strain of 63 and 122%, respectively, when cement and sand were replaced. When using rubberized cement mortar for plastering, increasing the ultimate strain is more advantageous and recommended over increasing the strength, since it is exposed to continuous cycles of thermal expansion, rather than a direct physical load.

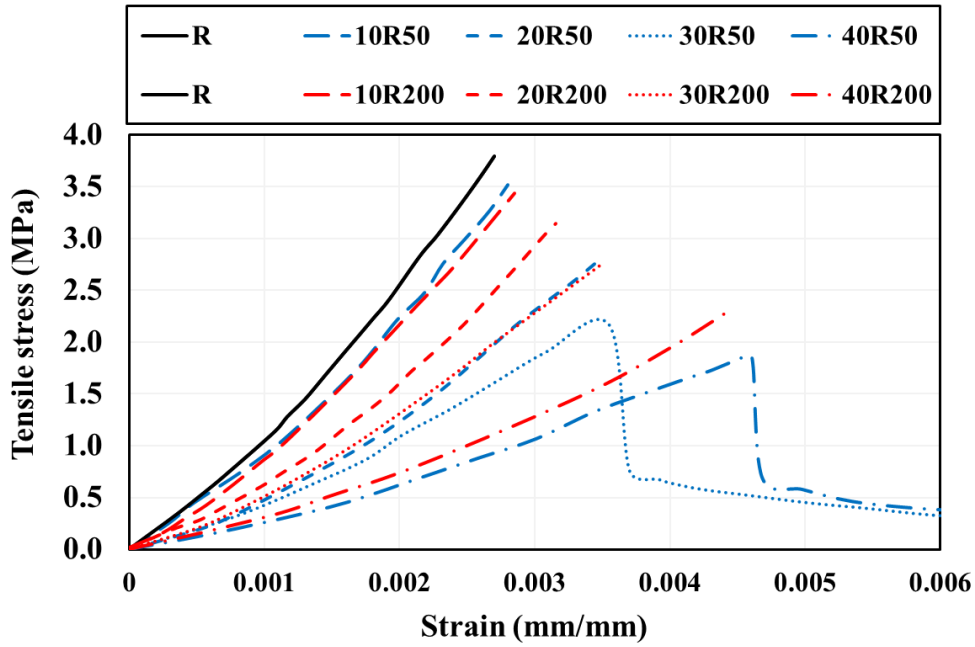

(a)

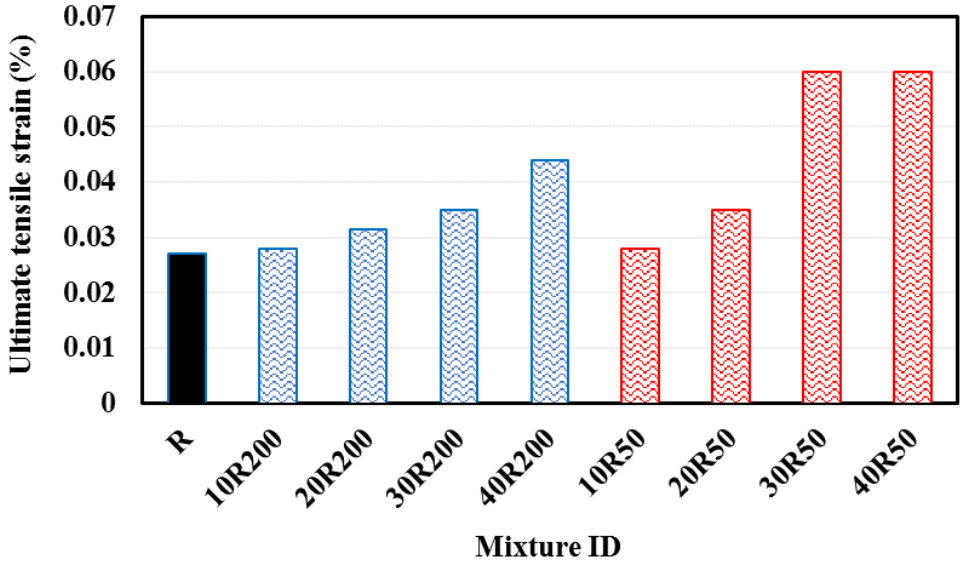

(b)

Figure 5.30: Tensile strength test: (a) Stress-strain behavior of cement mortar with different rubber powder sizes and content, and (b) The ultimate strain of cement mortar with different rubber powder sizes and content.

Although there was a reduction in the tensile and flexure strength, the modulus of toughness showed an increase of 19 and 16% when sand was replaced by 30 and 40%, respectively (Figure 5.31). These results show that increasing the RFP ratio will increase the strain energy that the rubberized mortar can absorb just before it fractures, which address the main cause of using plaster mortar. The modulus of resilience showed a relatively slight reduction with all RFP replacement ratios. These results show that an increasing RFP ratio will maintain approximately the same amount of strain energy that the rubberized mortar can absorb without permanent deformation.

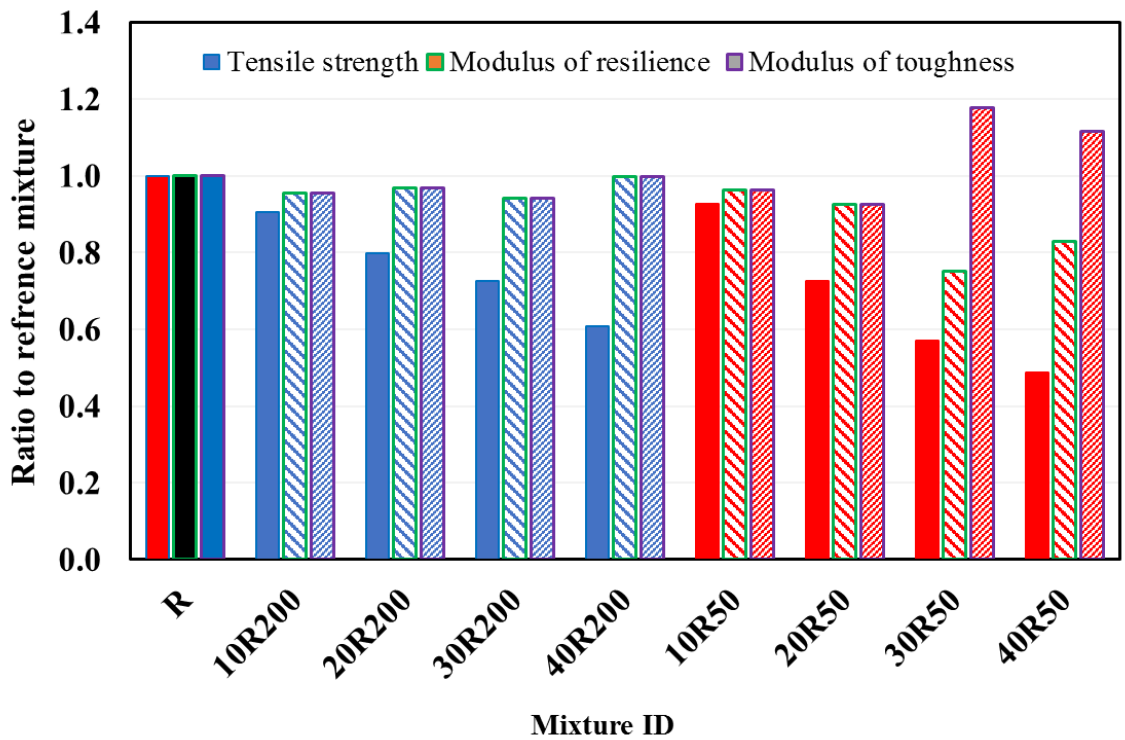

Figure 5.31: Compressive strength of rubberized plastering mortar with varied sizes and ratios of rubber-fiber powder.

5.2.3.2.Thermal conductivity

5.2.3.2.1. The thermal needle probe method for plastering materials

The relationship between the rubber replacement ratio and the thermal conductivity factor was approximately consistent (Figure 5.32). At a temperature of 25˚ C, replacing 10, 20, 30 and 40% of cement with RFP (R200) reduced the thermal conductivity factor of rubberized plastering mortar by 29, 41, 47, and 52% respectively. A higher reduction in thermal conductivity was noticed when sand was partially replaced with RFP. At a temperature of 25˚ C, replacing 10, 20, 30 and 40% of sand with RFP (R50) reduced the thermal conductivity factor of rubberized plastering mortar by 35, 53, 63, and 64%, respectively. Like the explanation in the density section, the strong influence on the thermal conductivity of the RFP with particle size between 150 and 300 µm (R50) compared to RFP with particle size smaller than 75 µm (R200) is attributed to the total ratio of RFP within the mortar matrix. This is because the sand represents 78% of the volume reference mortar matrix compared to 22% for the cement. For example, replacing 20% of cement with RFP (R200) led to a total RFP within the mortar matrix of 4.4%, compared to 15.6% when 20% of the sand was replaced with RFP (R50).

The coefficient of thermal conductivity showed a systematic reduction at low temperatures. For example, at a temperature of -10˚ C and RFP ratio of 20%, the coefficient of thermal conductivity decreased by 57 and 62% when cement and sand were replaced, respectively.

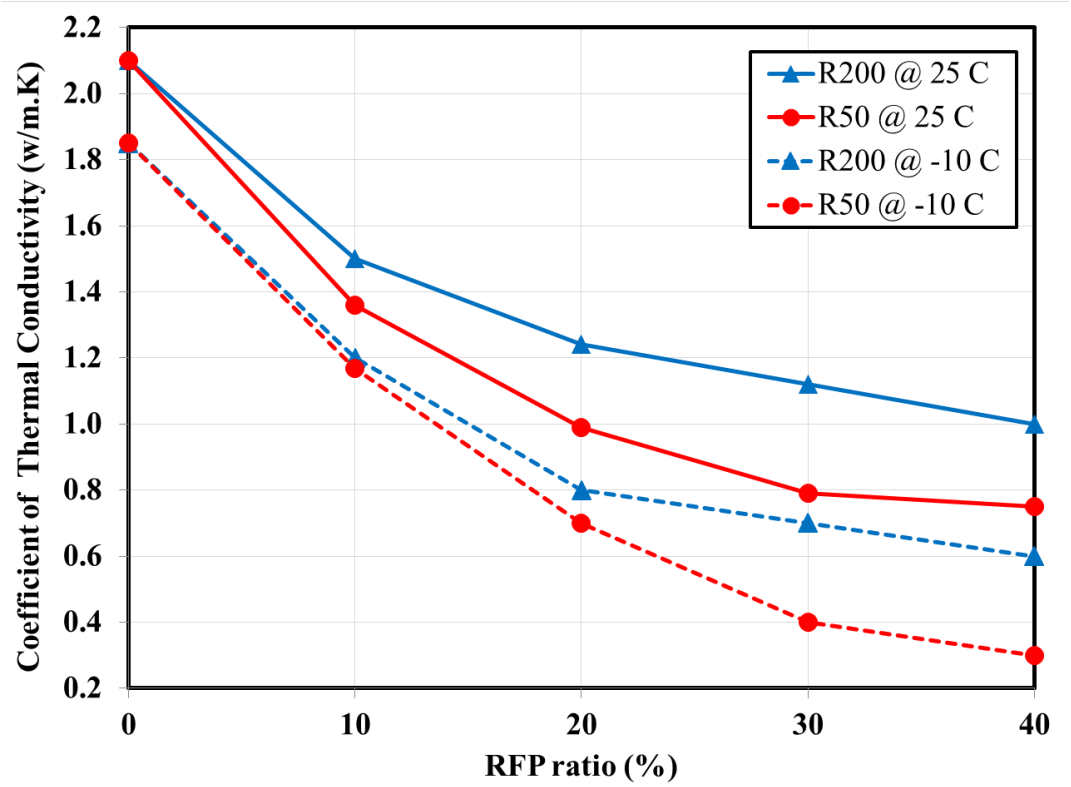

Figure 5.32: Thermal conductivity factor for rubberized mortar with different sizes and ratios of RFP.

5.2.3.2.2. Thermal conductivity of plaster masonry units using the guarded hot box method

Figure 5.33 shows the influence of applying three different thicknesses of mortar plastering with varied RFP ratios. Using RFP in plastering mortar as a partial replacement for either cement or sand had a significant effect on the thermal conductivity of plastered masonry units, based on the size and the amount of RFP within the plastering matrix. Applying 0.25-inch thick mortar plastering with 40% of the cement replaced by RFP decreased the thermal conductivity of the plastered unit from 1.02 to 0.9 (W/m.k). Simultaneously, by applying 0.75-inch thick mortar plastering with 40% of the cement replaced by RFP, the thermal conductivity of the plastered unit decreased from 0.96 to 0.72 (W/m.k). These results represent a reduction of 12% and 25% in thermal conductivity, respectively. The influence of replacing sand instead of cement on the

thermal conductivity was higher. For example, using 0.25, 0.50, and 0.75-inch thick mortar plastering with 40% of the sand replaced by RFP decreased the thermal conductivity by 34, 41, and 48% respectively, compared to 12, 19, and 25% respectively, when the cement was replaced at the same ratio. Comparing these results with the conventional masonry units without any plastering shows that a reduction varied from 11 to 53% can be achieved in thermal conductivity of masonry unit based on the size and amount of RFP as well as the thickness of the plastering lawyer. These reductions in thermal conductivity will be reflected in the same trend on the energy consumption of buildings using this type of rubberized mortar plastering. Figure 5.34 shows the effect of using RFP as a sand replacement on the reduction in energy consumption of masonry units with three plastering thicknesses.

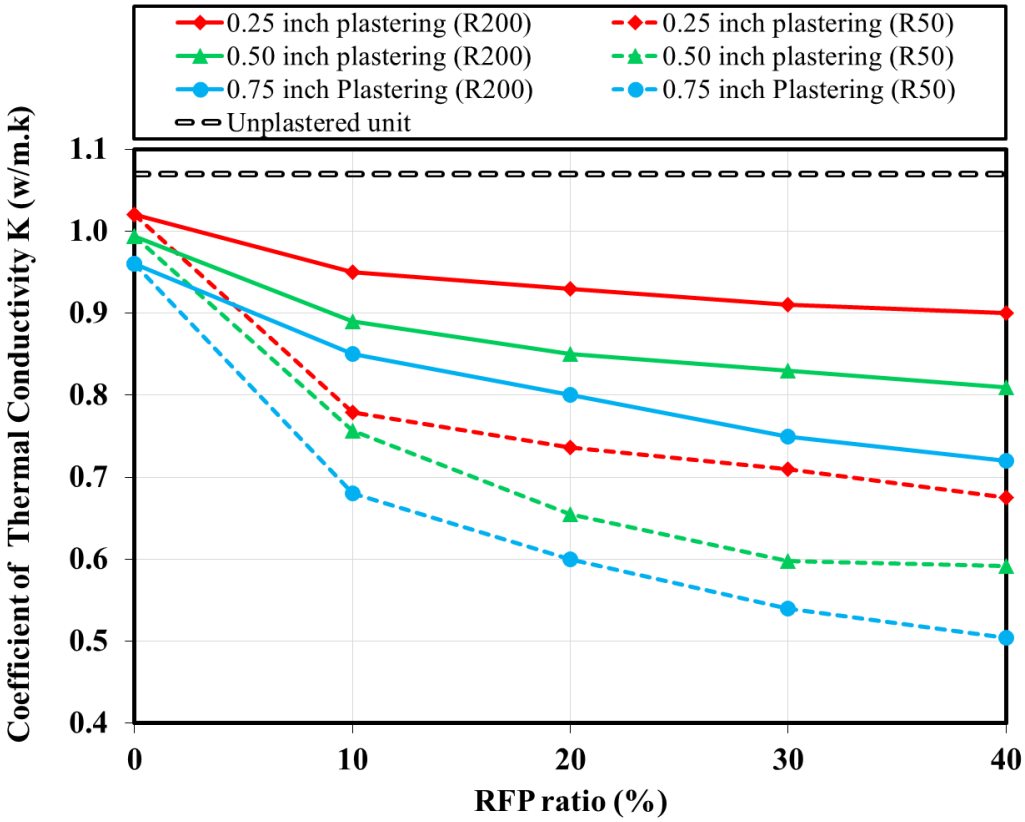

Figure 5.33: Thermal conductivity coefficients of masonry units with three plastering thicknesses and varied RFP sizes and content.

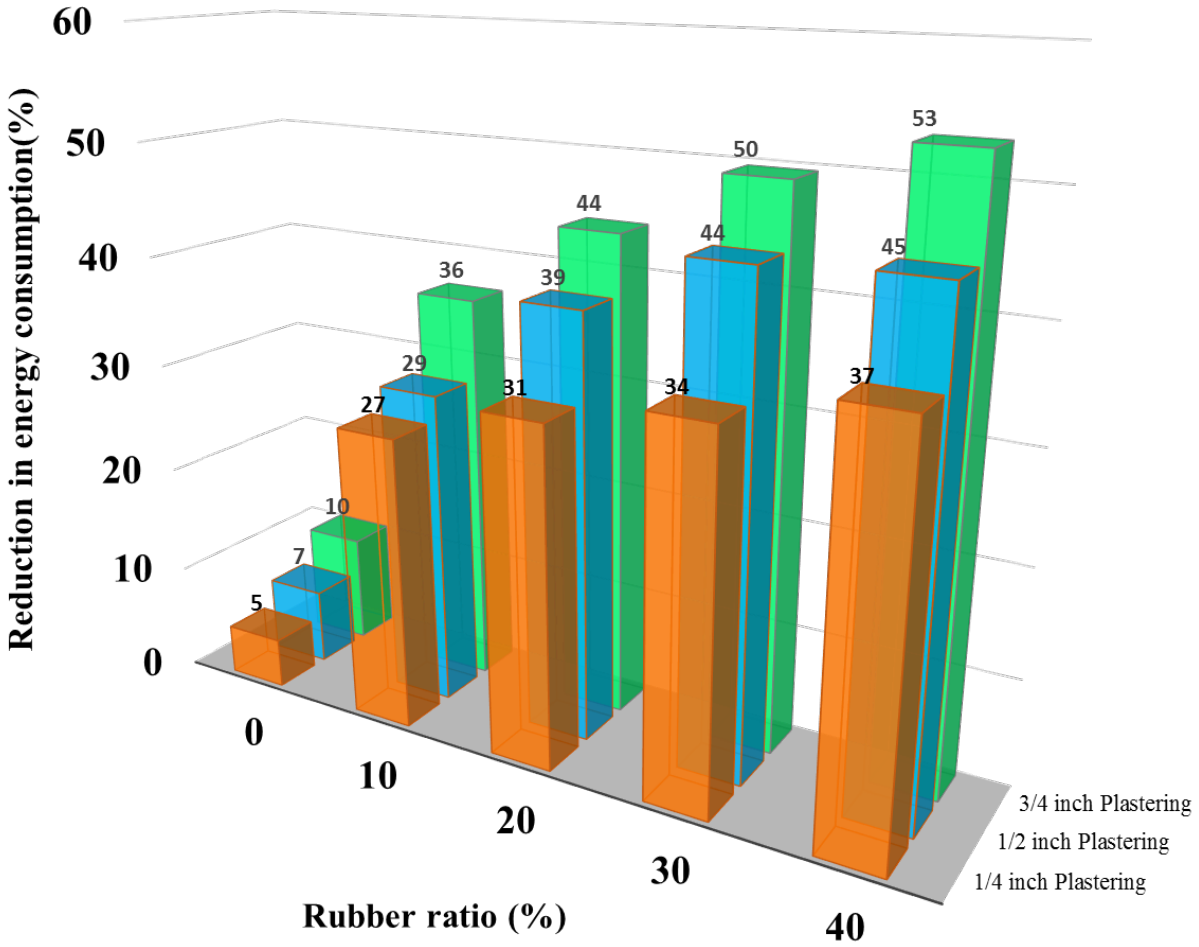

Figure 5.34: Effect of using RFP as a sand replacement on the reduction in energy consumption of masonry units with three plastering thicknesses.

5.2.3.3.Sound absorption

Figure 5.35 shows the sound absorption coefficients of unplastered and plastered masonry units with varied RFP content under frequency ranges from 50-5650 Hz. As shown in Figure 5.35, applying rubberized plastering mortar improved the sound absorption, especially with frequencies up to 3000 Hz. The results were also compared with unplastered masonry units where all plastered units behaved acoustically better than the unplastered unit.

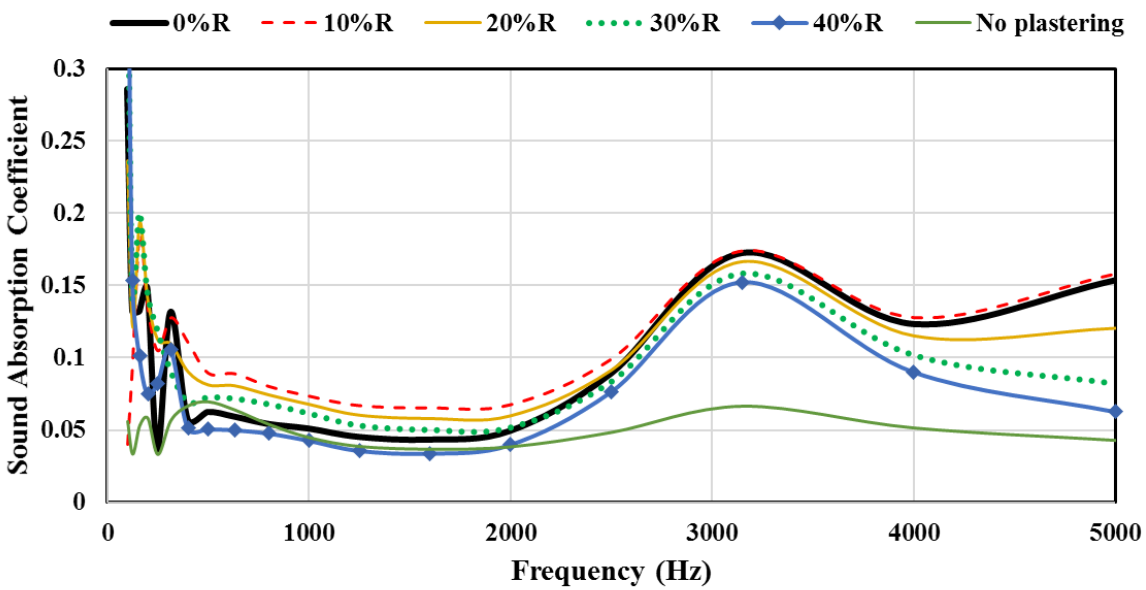

Figure 5.35: Sound absorption coefficient of plastered masonry units with varied RFP ratios.

Figure 5.36 presents the noise reduction factor of unplastered and plastered masonry units with varied RFP content. The noise reduction factor was increased by applying the plastering layer with varied RFP content. However, the plastering layer with a 10% RFP showed the best noise reduction of 0.34% compared with 0.2 for a layer of mortar plastering with 0% RFP and 0.19 for the unplastered masonry unit. This behavior was related to other factors that affect the noise reduction coefficient, such as the packing density and the surface texture of the plastering layers.

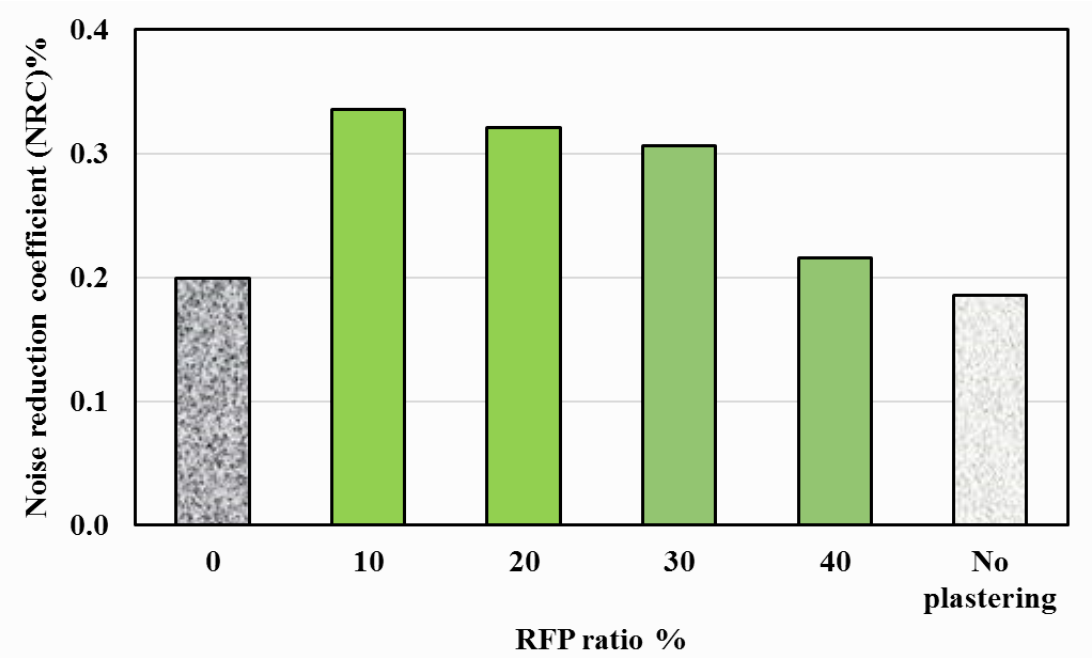

Figure 5.36: Noise reduction coefficient of plastered masonry units with varied RFP ratios.

5.2.4. Conclusions

Regarding to the thermal performance of rubberized concrete units, crumb rubber was used as a replacement of mineral fine aggregates to manufacture rubberized concrete masonry units (RCMUs). The thermal characteristics of RCMUs having rubber replacement ratios of 0%, 5%, 10%, and 15% were examined at the material and masonry block levels using four methods, namely the thermal needle probe procedure, guarded hot plate assembly method, guarded hot box method, and two controlled sides guarded hot box. The thermal performance of lightweight CMUs was also investigated as a reference specimen. The thermal characteristics are highly affected by the measuring method and the sample geometry (masonry unit vs. masonry plate). However, the general trends of the data were similar. Based on the experimental investigation, the following conclusions can be drawn:

- The specific heat increased linearly when increasing the rubber content. Increasing the rubber content from 0% to 15% increased the specific heat by an average of 8%

depending on the experiment temperature. For example, at 30° C, the specific heat increased from 920 J/kg.K to 1000 J/kg.K when increasing the rubber content in cement paste from 0% to 15%. A similar trend was measured at 45° C and 60° C.

- The thermal conductivity measured at the material level for rubberized masonry linearly decreased when increasing the rubber content. While the absolute values of the measured thermal conductivity varied depending on the measuring method used, both the thermal needle probe and guarded hot plate showed a reduction of 18.6% and 12.5% in the thermal conductivity, respectively, when the rubber content increased from 0% to 15%.
- The thermal conductivity measured at the masonry unit level showed a nonlinear decrease when increasing the rubber content. Adding rubber content of 5% to reduce the thermal diffusivity of the block resulted in a significant drop of 18% in the thermal conductivity. Beyond that, adding more rubber decreased the thermal conductivity at a smaller rate. Increasing the rubber content from 5% to 15% decreased the thermal conductivity by 13%.
- A reduction in energy consumption was measured when RCMU was used in lieu of CMU. Replacing the fine aggregate with 5%, 10%, and 15% crumb rubber reduced the energy consumption that is needed to keep the temperature constant inside the hot box by 18%, 26%, and 29% respectively.
- At the steady state, RCMUs had higher differences between the inner and outer temperatures compared to that of the CMUs. While the differences in inner and outer temperatures were 14.0° C for CMU, it increased to 17.3° C for RCMU having 15% rubber content. Furthermore, the time to reach steady-state heat flow was higher in

the case of RCMUs compared to that of CMU. Increasing the rubber content from 0% to 15% increased the time required to reach steady state by 18%.

Regarding to improving both thermal and acoustic insulation of conventional CMUs through using a a rubberized plastering mortar, rubber-fiber powder (RFP), a byproduct of the scrap tire recycling process, was used as a partial replacement of cement or sand in plastering mortar mixtures. Despite the reduction in some of the mechanical properties due to the inclusion of rubber powder in lieu of a portion of the cement or sand, this study found that the rubber powder obtained as a solid waste of scrap tires recycling could be used in the plastering mortar as an eco-friendly additive to provide better crack resistance and thermal and acoustic insulation based on the thickness of plastering layer from one side, and the size and content of RFP within the plastering layer. Based on the experimental investigation, the following points can be concluded:

- Plastering mortar mixtures with up to 40% of the cement or sand replaced by RFP did not show any difficulties to mix and apply with the required plastering thickness compared to the reference mortar mixture.
- Adding RFP with a size smaller than 75 μm up to 20% of cement, decreased the apparent and bulk densities. However, using RFP with a size between 150 and 300 μm as a sand replacement was more influential on both densities and continued up to 40% replacement of sand.
- Although there was a reduction in the compressive, tensile, and flexure strength, the modulus of toughness showed an increase of 19 and 16% when sand was replaced by 30 and 40% respectively, while the modulus of resilience showed a relatively slight reduction with all RFP replacement ratios. These results show that increasing the RFP

ratio will increase the strain energy that the rubberized mortar can absorb just before it fractures, which address the main cause of using plaster mortar.

- At a temperature of 25˚ C, replacing 10, 20, 30, and 40% of cement with RFP reduced the thermal conductivity factor of rubberized plastering mortar by 29, 41, 47, and 52% respectively. A higher reduction in thermal conductivity was noticed when sand was partially replaced with RFP.
- The coefficient of thermal conductivity showed a systematic reduction at low temperatures. At a temperature of -10˚ C, mixtures with an RFP ratio of 20% showed a reduction in the coefficient of thermal conductivity of 57 and 62% when cement and sand were replaced, respectively, compared to 41 and 53% at 25˚ C.
- Compared to conventional masonry units without any plastering, a reduction varying from 11 to 53% was achieved in the thermal conductivity of the masonry unit based on the size and amount of RFP as well as the thickness of the plastering layer.
- Applying rubberized plastering mortar improved the sound absorption, especially with frequencies up to 3000 Hz. Simultaneously, the noise reduction factor increased by applying the plastering layer with varied waste rubber powder content. The plastering layer with 10% waste rubber powder showed the best noise reduction of 0.34%, compared with 0.2 for a layer of mortar plastering with 0% waste rubber powder and 0.19 for unplastered masonry unit.

6. Conclusions and Future Work

With more than 1.1 billion vehicles on the road today and the expectation to double this number by 2040, the world is facing a serious threat dealing with 1.0 billion scrap tires every year, with continued growth. Furthermore, there is a tremendous increase in the use of natural materials in construction, which puts a huge burden on the environment and the whole ecosystem. With that being said, there is an opportunity for reducing the impact of the construction industry on the environment by replacing a portion of the mineral aggregate with a recycled one, where scrap tires are proposed to be a sustainable alternative.

Based on the above motives, this project investigates utilizing recycled crumb rubber as a partial replacement of natural mineral aggregate in the production of concrete masonry units (CMUs). The project started with optimizing the production presses, the size of rubber particles, and the rubber replacement ratios. Based on these parameters, rubberized concrete masonry units (RCMU) were produced both in the laboratory and in a plant setting. The mechanical properties of the new RCMUs were examined as well. In the second part, the impact of incorporating crumb rubber in CMUs on different durability aspects of the new units and structure were examined. The third part examined the thermal and acoustic behavior of the new proposed RCMUs using different measurements for thermal and sound conductivity and details the impact of using RCMUs on energy consumption for heating. The last part presented the seismic and cyclic behavior of rubberized masonry prisms and full-scale structural elements and the benefits of incorporating crumb rubber within the masonry structure in terms of responding to seismic and cyclic loads.

All the lessons learned during this project were integrated and evolved to optimize the RCMU mixes that had superior performance compared to previously available trials in the

literature. The proposed mixes were also cost-effictive and practical in terms of using them in the daily production process at mass production facilities.

6.1. Findings and conclusions

Based on the main findings of this study, the following conclusions can be drawn:

In terms of the production process and parameters, this project discloses that:

- Recycled crumb rubber with particle sizes between 2.83 and 0.841 mm can be utilized with fine aggregate replacement ratios up to 15% to produce rubberized concrete masonry units that meet the ASTM requirements for loadbearing units.

- The compaction pressure of 30 psi results in the highest dry density, recommending its use in mass production of RCMUs.

- Rubberized concrete masonry units with a crumb rubber replacement ratio up to 15% can be produced in masonry production facilities using the same conventional process without any obstacles or modifications.

- A crumb rubber replacement ratio of 5% resulted in the highest dry density and compressive strength as well as the lowest water absorption. However, RCMUs with crumb rubber ratios up to 15% can be produced to meet the ASTM C90−12 requirements in terms of compressive strength, absorption, and density.

In terms of durability and despite the reduction in some of the mechanical properties due to the inclusion of rubber powder in lieu of a portion of the cement, this project discloses that the rubber powder obtained as a solid waste of scrap tire recycling could be used in the mortar as an additive to provide more corrosion resistance and less heat of hydration. In particular, the following points can be concluded:

- Adding rubber fiber powder (RFP) to mortar mixtures decreased mortar workability. For w/c of 0.51 and 0.56, mortar mixtures with up to 20% RFP addition displayed good workability, reaching flowability of 40%, and 70%, respectively.

- Decreases in the compressive and flexural strengths were noticed with the increase in the RFP ratio. For example, for mixtures with w/c of 0.51 at the age of 28 days, the compressive and flexural strength of rubberized cement mortar with 10% RFP decreased by 35%, and 27%, respectively. However, the compressive and flexural strength of cement mortar with 10% sand addition instead of cement decreased by 76%, and 76%, respectively, which shows the advantage of adding RFP instead of cutting the cement content.

- The impact of adding the RFP on the bulk density relates to w/c ratio, workability, and the volume of the permeable voids. Adding 15% RFP reduced the bulk density after immersion and boiling from 2.20, 2.16, and 2.12 to 2.11, 2.02, and 2.06 for mixtures with w/c ratios of 0.42, 0.51, and 0.56 respectively.

- Adding the RFP lowered and delayed the peak temperature for the heat of hydration compared to reducing the cement content. The magnitude and the time of the peak heat flow of mixtures with 20% RFP ratios decreased by 25.5% and 31.5%, respectively.

- Mortar mixtures with up to 20% RFP showed improved bulk and surface electrical resistivity values which, are significant indications for better reinforcement corrosion resistance. For example, mixtures with w/c of 0.51 showed a linear increase in bulk and surface resistivity from 17.2 and 3.48 to 29.7 and 7.73, respectively, with 20% RFP. Beyond 20% RFP, the bulk and surface resistivity decreased due to the increase in the volume of the permeable voids.

- The carbon dioxide penetration depth dropped by 38% by adding 10% of RFP to the mortar mixture with w/c ratio of 0.56. However, adding 5% or higher RFP for mixtures having w/c of 0.51 led to a linear increase in the carbonation depth reaching 200% at 25% addition. Furthermore, for both w/c ratios, adding RFP was much better than adding sand. When adding 5% or higher sand, carbon dioxide had a full penetration through the specimens for mixtures with a w/c ratio of 0.51 and 0.56 due to the change in air void content, particle arrangement, and accompanying air voids.

- The results presented in this report showed that using RFP of 10% to 15% in combination with w/c of 0.51 to 0.56 can yield a workable rubberized mortar with a significant potential for high corrosion resistance.

Regarding the predicted seismic performance of structural elements with rubberized concrete masonry units and based on the experimental investigation, the following conclusions can be drawn:

- The use of rubber in masonry block units has a significant impact on increasing the peak strain.

- The use of rubber in masonry block units influences the initial stiffness and ductility of fully grouted masonry prisms.

- There is no significant loss in compressive strength when rubberized masonry units are used in fully grouted prisms.

- The full scale rubberized masonry wall showed a superior performance where a ductile and gradual failure was reported compared to sudden and brittle failure in the case of the exact same wall but with conventional CMUs.

- The rubberized shear wall has higher energy dissipation at each displacement level compared to the reference wall. For higher displacement levels, the rubber wall showed a 20% increase in energy dissipation. The total energy dissipated by the rubber wall is 64% higher than that of the reference wall.

- The rubberized wall had a very high damping ratio post yielding. At an ultimate displacement of the reference wall, the rubber wall shows almost more than twice the damping ratio compared to the reference wall.

Regarding the thermal characteristics' of RCMUs at the material and masonry block levels, and based on the experimental investigation, the following conclusions can be drawn:

- The specific heat increased linearly with an increase in the rubber content. Increasing the rubber content from 0% to 15% increased the specific heat by an average of 8% depending on the experiment temperature. For example, at 30° C, the specific heat increased from 920 J/kg.K to 1000 J/kg.K when increasing rubber content in cement paste from 0% to 15%. A similar trend was measured at 45° C and 60° C.

- The thermal conductivity measured at the material level for rubberized masonry linearly decreased with an increase in the rubber content. While the absolute values of the measured thermal conductivity varied depending on the measuring method used, both the thermal needle probe and guarded hot plate showed a reduction of 18.6% and 12.5% in the thermal conductivity, respectively, when the rubber content increased from 0% to 15%.

- The thermal conductivity measured at the masonry unit level showed a nonlinear decrease with an increase in the rubber content. Adding rubber content of 5% reduced the thermal diffusivity of the block, resulting in a significant drop of 18% in the thermal conductivity. Beyond that, adding more rubber decreased the thermal conductivity at a slower rate. Increasing the rubber content from 5% to 15% decreased the thermal conductivity by 13%.

- A reduction in energy consumption was measured when RCMU was used in lieu of CMU. Replacing the fine aggregate with 5%, 10%, and 15% crumb rubber reduced the energy consumption that is needed to keep the temperature constant inside the hot box by 18%, 26%, and 29% respectively.

- At the steady state, RCMUs had higher differences between the inner and outer temperatures compared to those of the CMUs. While the differences in inner and outer temperatures were 14.0° C for CMU it increased to 17.3° C for RCMU having 15% rubber content. Furthermore, the time to reach steady-state heat flow was higher in the case of RCMUs compared to that of CMU. Increasing the rubber content from 0% to 15% increased the time required to reach steady state by 18%.

- Compared to the reference mortar mixture, plastering mortar mixtures with up to 40% of the cement or sand replaced by RFP did not show any difficulties in mixing and application with the required thickness.

- Adding upto 20% RFP with a size smaller than 75 µm decreased the apparent and bulk densities. However, using RFP with a size between 150 and 300 µm as a sand replacement was more influential on both densities, and it continued up to 40% replacement of sand.

- Although there was a reduction in the compressive, tensile, and flexure strength, the modulus of toughness showed an increase of 19% and 16% when 30% and 40% of sand was replaced by RFP, respectively, while the modulus of resilience showed a relatively slight reduction with all RFP replacement ratios. These results show that increasing the RFP ratio will increase the strain energy that the rubberized mortar can absorb just before it fractures, which address the main cause of using plaster mortar.

- At a temperature of 25˚ C, replacing 10%, 20%, 30% and 40% of cement with RFP reduced the thermal conductivity factor of rubberized plastering mortar by 29%, 41%, 47%, and 52%, respectively. A higher reduction in thermal conductivity was noticed when sand was partially replaced with RFP.

- The coefficient of thermal conductivity showed a systematic reduction at low temperatures. At a temperature of -10˚ C, mixtures with a RFP ratio of 20% showed a reduction in coefficient of thermal conductivity of 57 and 62%, respectively, when cement and sand were replaced compared to 41 and 53% at 25˚ C.

- Compared to conventional CMUs without any plastering, a reduction varying from 11% to 53% was achieved in the thermal conductivity of the masonry unit based on the size and amount of RFP as well as the thickness of the plastering layer.

- Applying rubberized plastering mortar improved the sound absorption especially with frequencies up to 3000 Hz. Simultaneously, the noise reduction factor increased by applying the plastering layer with varied waste rubber powder content. The plastering layer with 10% waste rubber powder showed the best noise reduction of 0.34% compared with 0.20% for a layer of mortar plastering with 0% waste rubber powder and 0.19% for the unplastered masonry unit.

6.2. Future work

While this study introduced a guide to utilizing recycled scrap tires in the production of rubberized concrete masonry units (RCMUs) with high performance in terms of strength, ductility, durability, thermal, and acoustic behavior, further studies are still required to fine-tune the production and use of RCMU as well as their performance under different conditions. In addition, new aspects need to be investigated. This includes the following areas:

1. The effects of different rubber properties on the overall energy consumption of RCMU buildings.
2. The performance of rubberized concrete masonry units under elevated temperature and fire.
3. The effect of using RCMU on the structural integrity of buildings, including the development length of rebar, shear strength, bearing strength, etc.

7. References

AASHTO (2015). AASHTO T 358:2015Method Of Test For Surface Resistivity Indication Of Concrete'S Ability To Resist Chloride Ion Penetration.

Abu-Lebdeh, T., E. Fini and A. Fadiel (2014). "Thermal conductivity of rubberized gypsum board." Am. J. Eng. Applied Sci **7**: 12-22.

Amirkhanian, S. N. (2001). "Utilization of crumb rubber in asphaltic concrete mixtures–South Carolina's Experience." See ref **3**: 163-174.

Ang, G. and V. Marchal (2013). "Mobilising private investment in sustainable transport: The case of land-based passenger transport infrastructure." OECD Environment Working Papers(56): 0_1.

Azarsa, P. and R. Gupta (2017). "Electrical resistivity of concrete for durability evaluation: a review." Advances in Materials Science and Engineering **2017**.

Batayneh, M. K., I. Marie and I. Asi (2008). "Promoting the use of crumb rubber concrete in developing countries." Waste Management **28**(11): 2171-2176.

Benazzouk, A. and M. Queneudec (2002). Durability of cement-rubber composites under freeze thaw cycles. Proceeding of International congress of Sustainable Concrete Construction, Dundee-Scotland.

Berrueco, C., E. Esperanza, F. Mastral, J. Ceamanos and P. García-Bacaicoa (2005). "Pyrolysis of waste tyres in an atmospheric static-bed batch reactor: Analysis of the gases obtained." Journal of Analytical and Applied Pyrolysis **74**(1): 245-253.

Chini, A. R., L. C. Muszynski and J. K. Hicks (2003). Determination of acceptance permeability characteristics for performance-related specifications for Portland cement concrete.

Eldin, N. N. and A. B. Senouci (1993). "Rubber-tire particles as concrete aggregate." Journal of materials in civil engineering **5**(4): 478-496.

Epps, J. and L. Mason (1994). Uses of recycled rubber tires in highways: A synthesis of highway practice. Final report, National Cooperative Highway Research Program, Washington, DC (United States).

Fadiel, A., F. Al Rifaie, T. Abu-Lebdeh and E. Fini (2014). "Use of crumb rubber to improve thermal efficiency of cement-based materials." American Journal of Engineering and Applied Sciences **7**(1): 1-11.

Fattuhi, N. and L. Clark (1996). "Cement-based materials containing shredded scrap truck tyre rubber." Construction and building materials **10**(4): 229-236.

Fedroff, D., S. Ahmad and B. Savas (1996). "Mechanical properties of concrete with ground waste tire rubber." Transportation Research Record: Journal of the Transportation Research Board(1532): 66-72.

Forrest, M. (2014). Recycling and re-use of waste rubber, Smithers Rapra.

Ganjian, E., M. Khorami and A. A. Maghsoudi (2009). "Scrap-tyre-rubber replacement for aggregate and filler in concrete." Construction and Building Materials **23**(5): 1828-1836.

Gesoğlu, M. and E. Güneyisi (2011). "Permeability properties of self-compacting rubberized concretes." Construction and building materials **25**(8): 3319-3326.

Gesoğlu, M., E. Güneyisi, G. Khoshnaw and S. İpek (2014). "Investigating properties of pervious concretes containing waste tire rubbers." Construction and Building Materials **63**: 206-213.

Gheni, A., M. A. ElGawady and J. J. Myers (2017). "Thermal Characterization of Cleaner and Eco-Efficient Masonry Units Using Sustainable Aggregates." Journal of Cleaner Production.

Gheni, A. A., O. I. Abdelkarim, M. M. Abdulazeez and M. A. ElGawady (2017). "Texture and design of green chip seal using recycled crumb rubber aggregate." Journal of Cleaner Production **166**: 1084-1101.

Gheni, A. A., M. A. ElGawady and J. J. Myers (2017). "Mechanical Characterization of Concrete Masonry Units Manufactured with Crumb Rubber Aggregate." ACI Materials Journal **114**(01).

Gheni, A. A., S. M. Lusher and M. A. ElGawady (2018). "Retention behavior of crumb rubber as an aggregate in innovative chip seal surfacing." Journal of Cleaner Production **197**: 1124-1136.

Gou, M. and X. Liu (2014). "Effect of rubber particle modification on properties of rubberized concrete." Journal of Wuhan University of Technology-Mater. Sci. Ed. **29**(4): 763-768.

Gransberg, D. D. and D. M. James (2005). Chip seal best practices, Transportation Research Board.

Gupta, T., S. Chaudhary and R. K. Sharma (2014). "Assessment of mechanical and durability properties of concrete containing waste rubber tire as fine aggregate." Construction and Building Materials **73**: 562-574.

Hall, M. R., K. B. Najim and C. J. Hopfe (2012). "Transient thermal behaviour of crumb rubber-modified concrete and implications for thermal response and energy efficiency in buildings." Applied thermal engineering **33**: 77-85.

Hammond, G. P. and C. I. Jones (2008). "Embodied energy and carbon in construction materials." Proceedings of the Institution of Civil Engineers-Energy **161**(2): 87-98.

Hanson, D., J. Epps and R. Hicks (1996). "Construction Guidelines for Crumb Rubber Modified Hot Mix Asphalt." Federal Highway Administration Report DTFH61-94-C-00035.

Hernandez-Olivares, F., G. Barluenga, M. Bollati and B. Witoszek (2002). "Static and dynamic behaviour of recycled tyre rubber-filled concrete." Cement and concrete research **32**(10): 1587-1596.

Ho, A. C., A. Turatsinze, R. Hameed and D. C. Vu (2012). "Effects of rubber aggregates from grinded used tyres on the concrete resistance to cracking." Journal of Cleaner Production **23**(1): 209-215.

Hornbostel, K., C. K. Larsen and M. R. Geiker (2013). "Relationship between concrete resistivity and corrosion rate–a literature review." Cement and Concrete Composites **39**: 60-72.

Horvath, A. (2004). "Construction materials and the environment." Annu. Rev. Environ. Resour. **29**: 181-204.

Huang, Y., J.-l. Niu and T.-m. Chung (2013). "Study on performance of energy-efficient retrofitting measures on commercial building external walls in cooling-dominant cities." Applied energy **103**: 97-108.

Isler, J. W. (2012). Assessment of concrete masonry units containing aggregate replacements of waste glass and rubber tire particles, University of Colorado at Denver.

Kaewunruen, S. and R. Meesit (2016). "Sensitivity of crumb rubber particle sizes on electrical resistance of rubberised concrete." Cogent Engineering **3**(1): 1126937.

Karasahin, M., B. Aktas, A. Gungor, F. Orhan and C. Gurer (2014). "Laboratory and In Situ Investigation of Chip Seal Surface Condition Improvement." Journal of Performance of Constructed Facilities **29**(2): 04014047.

Kashani, A., T. D. Ngo, P. Mendis, J. R. Black and A. Hajimohammadi (2017). "A sustainable application of recycled tyre crumbs as insulator in lightweight cellular concrete." Journal of Cleaner Production **149**: 925-935.

Kessler, R. J., R. G. Powers and M. P. Mario Paredes (2005). "Resistivity measurements of water saturated concrete as an indicator of permeability." CORROSION 2005.

Khatib, Z. K. and F. M. Bayomy (1999). "Rubberized Portland cement concrete." Journal of materials in civil engineering **11**(3): 206-213.

Kolaitis, D. I., E. Malliotakis, D. A. Kontogeorgos, I. Mandilaras, D. I. Katsourinis and M. A. Founti (2013). "Comparative assessment of internal and external thermal insulation systems for energy efficient retrofitting of residential buildings." Energy and Buildings **64**: 123-131.

Kulakowski, M. P., F. M. Pereira and D. C. Dal Molin (2009). "Carbonation-induced reinforcement corrosion in silica fume concrete." Construction and Building Materials **23**(3): 1189-1195.

Lee, S.-J., C. K. Akisetty and S. N. Amirkhanian (2008). "The effect of crumb rubber modifier (CRM) on the performance properties of rubberized binders in HMA pavements." Construction and Building Materials **22**(7): 1368-1376.

Liu, H., X. Wang, Y. Jiao and T. Sha (2016). "Experimental investigation of the mechanical and durability properties of crumb rubber concrete." Materials **9**(3): 172.

Maupin Jr, G. (1996). "Hot mix asphalt rubber applications in Virginia." Transportation Research Record: Journal of the Transportation Research Board(1530): 18-24.

Milne, G. and C. Reardon (2005). "Embodied energy." Your Home Technical Manual: Australia's guide to environmentally sustainable homes. Commonwealth of Australia.

Mohammed, B. S., K. M. A. Hossain, J. T. E. Swee, G. Wong and M. Abdullahi (2012). "Properties of crumb rubber hollow concrete block." Journal of Cleaner Production **23**(1): 57-67.

Moustafa, A. and M. A. ElGawady (2017). "Dynamic properties of high strength rubberized concrete." ACI Spec. Publ **314**: 1-22.

Moustafa, A. and M. A. ElGawady (2015). "Mechanical properties of high strength concrete with scrap tire rubber." Construction and Building Materials **93**: 249-256.

Moustafa, A. and M. A. ElGawady (2016). "Strain rate effect on properties of rubberized concrete confined with glass fiber–reinforced polymers." Journal of Composites for Construction **20**(5): 04016014.

Moustafa, A., A. Gheni and M. A. ElGawady (2017). "Shaking-Table Testing of High Energy–Dissipating Rubberized Concrete Columns." Journal of Bridge Engineering **22**(8): 04017042.

Najim, K. and M. Hall (2010). "A review of the fresh/hardened properties and applications for plain-(PRC) and self-compacting rubberised concrete (SCRC)." Construction and building materials **24**(11): 2043-2051.

Najim, K. B. and M. R. Hall (2012). "Workability and mechanical properties of crumb-rubber concrete." Proceedings of the Institution of Civil Engineers-Construction Materials **166**(1): 7-17.

Olorunniwo, A. (1994). Effects of recycled scrap tires and asphalt pavement on the engineering properties of portland cement concrete, University of Texas at Austin.

Onuaguluchi, O. and D. K. Panesar (2014). "Hardened properties of concrete mixtures containing pre-coated crumb rubber and silica fume." Journal of cleaner production **82**: 125-131.

Pacheco-Torgal, F., P. B. Lourenço, J. Labrincha and S. Kumar (2014). Eco-efficient masonry bricks and blocks: design, properties and durability, Woodhead Publishing.

Pacheco-Torgal, F., P. B. Lourenço, J. Labrincha and S. Kumar (2015). Eco-efficient masonry bricks and blocks: design, properties and durability, Woodhead Publishing.

Page, G. C. (1992). "Florida's initial experience utilizing ground tire rubber in asphalt concrete mixes." Journal of the Association of Asphalt Paving Technologists **61**.

Paine, K. A. and R. K. Dhir (2010). "Research on new applications for granulated rubber in concrete." Proceedings of the institution of civil engineers: construction materials **163**(1): 7-17.

Papagiannakis, A. and T. Lougheed (1995). A REVIEW OF CRUMB-RUBBER MODIFIED ASPHALT CONCRETE TECHNOLOGY. RESEARCH REPORT.

Presti, D. L. (2013). "Recycled tyre rubber modified bitumens for road asphalt mixtures: a literature review." Construction and Building Materials **49**: 863-881.

Rada, E. C., M. Ragazzi, R. Dal Maschio, M. Ischia and V. N. Panaitescu (2012). "Energy recovery from tyres waste through thermal option." Scientific Bulletin, Politehnica University of Bucharest, Series D, Mechanical Engineering **74**: 201-210.

Rangaraju, P. and S. Gadkar (2012). "Durability evaluation of crumb rubber addition rate on Portland cement concrete." Department of Civil Engineering, Clemson University, Clemson: 1-126.

Richardson, A., K. Coventry, V. Edmondson and E. Dias (2016). "Crumb rubber used in concrete to provide freeze–thaw protection (optimal particle size)." Journal of Cleaner Production **112**: 599-606.

Richardson, A. E., K. A. Coventry and G. Ward (2012). "Freeze/thaw protection of concrete with optimum rubber crumb content." Journal of Cleaner Production **23**(1): 96-103.

RMA, R. M. A. (2018). 2017 U.S. Scrap Tire Management Summary. Wasington, DC.

Sadek, D. M. and M. M. El-Attar (2015). "Structural behavior of rubberized masonry walls." Journal of Cleaner Production **89**: 174-186.

Sajwani, A. and Y. Nielsen (2017). "THE APPLICATION OF THE ENVIRONMENTAL MANAGEMENT SYSTEM AT THE ALUMINUM INDUSTRY IN UAE." International Journal **12**(30): 1-10.

Savas, B., S. Ahmad and D. Fedroff (1997). "Freeze-thaw durability of concrete with ground waste tire rubber." Transportation Research Record: Journal of the Transportation Research Board(1574): 80-88.

Sengul, O. (2014). "Use of electrical resistivity as an indicator for durability." Construction and Building Materials **73**: 434-441.

Shuler, S. (2011). Use of Waste Tires, Crumb Rubber, on Colorado Highways, Colorado Department of Transportation, DTD Applied Research and Innovation Branch.

Si, R., J. Wang, S. Guo, Q. Dai and S. Han (2018). "Evaluation of laboratory performance of self-consolidating concrete with recycled tire rubber." Journal of Cleaner Production **180**: 823-831.

Siddique, R. and T. R. Naik (2004). "Properties of concrete containing scrap-tire rubber–an overview." Waste management **24**(6): 563-569.

Song, H.-W. and V. Saraswathy (2007). "Corrosion monitoring of reinforced concrete structures-A." Int. J. Electrochem. Sci **2**: 1-28.

Sperling, D. and D. Gordon (2009). Two billion cars: driving toward sustainability, Oxford University Press.

Sperling, D. and D. Gordon (2008). "Two billion cars: transforming a culture." TR news(259).

Sukontasukkul, P. (2009). "Use of crumb rubber to improve thermal and sound properties of pre-cast concrete panel." Construction and Building Materials **23**(2): 1084-1092.

Sukontasukkul, P. and C. Chaikaew (2006). "Properties of concrete pedestrian block mixed with crumb rubber." Construction and Building Materials **20**(7): 450-457.

Thomas, B. S. and R. C. Gupta (2016). "A comprehensive review on the applications of waste tire rubber in cement concrete." Renewable and Sustainable Energy Reviews **54**: 1323-1333.

Thomas, B. S. and R. C. Gupta (2015). "Long term behaviour of cement concrete containing discarded tire rubber." Journal of Cleaner Production **102**: 78-87.

Thomas, B. S. and R. C. Gupta (2013). "Mechanical properties and durability characteristics of concrete containing solid waste materials." Journal of Cleaner Production.

Thomas, B. S., R. C. Gupta and V. J. Panicker (2016). "Recycling of waste tire rubber as aggregate in concrete: durability-related performance." Journal of Cleaner Production **112**: 504-513.

Thumann, A. and R. K. Miller (1986). "Fundamentals of noise control engineering."

Triantafillou, T. C., K. Karlos, K. Kefalou and E. Argyropoulou (2017). "An innovative structural and energy retrofitting system for URM walls using textile reinforced mortars combined with thermal insulation: Mechanical and fire behavior." Construction and Building Materials **133**: 1-13.

Troy, K., P. Sebaaly and J. Epps (1996). "Evaluation systems for crumb rubber modified binders and mixtures." Transportation Research Record: Journal of the Transportation Research Board(1530): 3-10.

Turgut, P. and B. Yesilata (2008). "Physico-mechanical and thermal performances of newly developed rubber-added bricks." Energy and Buildings **40**(5): 679-688.

Xue, J. and M. Shinozuka (2013). "Rubberized concrete: A green structural material with enhanced energy-dissipation capability." Construction and Building Materials **42**: 196-204.

Yesilata, B., H. Bulut and P. Turgut (2011). "Experimental study on thermal behavior of a building structure using rubberized exterior-walls." Energy and Buildings **43**(2): 393-399.

Youssf, O., M. A. ElGawady and J. E. Mills (2015). Experimental investigation of crumb rubber concrete columns under seismic loading. Structures, Elsevier.

Youssf, O., M. A. ElGawady and J. E. Mills (2016). "Static cyclic behaviour of FRP-confined crumb rubber concrete columns." Engineering Structures **113**: 371-387.

Youssf, O., M. A. ElGawady, J. E. Mills and X. Ma (2017). "Analytical modeling of the main characteristics of crumb rubber concrete." Special Publication **314**: 1-18.

Yung, W. H., L. C. Yung and L. H. Hua (2013). "A study of the durability properties of waste tire rubber applied to self-compacting concrete." Construction and Building Materials **41**: 665-672.

Zhang, B. and C. S. Poon (2018). "Sound insulation properties of rubberized lightweight aggregate concrete." Journal of Cleaner Production **172**: 3176-3185.

Zheng, L., X. S. Huo and Y. Yuan (2008). "Experimental investigation on dynamic properties of rubberized concrete." Construction and building materials **22**(5): 939-947.

Zhu, X., C. Miao, J. Liu and J. Hong (2012). "Influence of crumb rubber on frost resistance of concrete and effect mechanism." Procedia Engineering **27**: 206-213.